

https://dspace.org/

# Ammonia Synthesis over Transition Metal Catalysts Reaction Mechanisms RateDetermining Steps and Challenges

**Pradeep Varadwaj; Helder Marques; Ireneusz Grabowski**

MDPI AG
https://hdl.handle.net/10539/46452
WOS

Downloaded from a DSpace repository. https://dspace.org/

International Journal of
*Molecular Sciences*

MDPI

*Review*

# Ammonia Synthesis over Transition Metal Catalysts: Reaction Mechanisms, Rate-Determining Steps, and Challenges

**Pradeep R. Varadwaj [1,2,*], Helder M. Marques [1] and Ireneusz Grabowski [2]**

[1] Molecular Sciences Institute, School of Chemistry, University of the Witwatersrand, Johannesburg 2050, South Africa
[2] Institute of Physics, Faculty of Physics, Astronomy, and Informatics, Nicolaus Copernicus University in Toruń, 87-100 Toruń, Poland
* Correspondence: pradeep@t.okayama-u.ac.jp

**Abstract:** Ammonia synthesis remains a cornerstone of global chemical manufacturing, essential for fertilizer production, energy storage, and emerging carbon capture technologies. This overview examines recent developments in the understanding of elementary reaction mechanisms in heterogeneous catalysis, with emphasis on transition metal thermocatalysts operating under the Haber–Bosch process. Traditionally, the dissociative adsorption of nitrogen ($N_2$) has been considered the rate-determining step. However, recent studies challenge this view, revealing possible shifts in rate-determining steps and suggesting that alternative mechanistic pathways may be operative. The discussion critiques studies that adhere strictly to the classic dissociative mechanism—often inferred from the reaction order of $N_2$—while overlooking alternative pathways that could offer more efficient catalytic routes and deeper mechanistic insight into ammonia synthesis. These insights offer a pathway toward more rational catalyst design and improved process efficiency in ammonia synthesis.

**Keywords:** ammonia synthesis; Haber–Bosch process; concepts and applications; elementary reaction mechanisms; reaction order; rate-determining step

check for updates

Academic Editor: Haiyang Gao

Received: 24 March 2025
Revised: 5 May 2025
Accepted: 6 May 2025
Published: 13 May 2025

**Citation:** Varadwaj, P.R.; Marques, H.M.; Grabowski, I. Ammonia Synthesis over Transition Metal Catalysts: Reaction Mechanisms, Rate-Determining Steps, and Challenges. *Int. J. Mol. Sci.* **2025**, *26*, 4670. https://doi.org/10.3390/ijms26104670

**Copyright:** © 2025 by the authors. Licensee MDPI, Basel, Switzerland. This article is an open access article distributed under the terms and conditions of the Creative Commons Attribution (CC BY) license (https://creativecommons.org/licenses/by/4.0/).

## 1. Introduction

The energy-intensive Haber–Bosch process [1], an unparalleled breakthrough developed by the brilliant minds of Fritz Haber and Carl Bosch [2–4]—both of whom were honored with Nobel Prizes in Chemistry (1918 and 1931, respectively)—has stood as the bedrock of industrial ammonia synthesis for over a century [5], revolutionizing the large-scale production of ammonia, which is indispensable to the global agricultural system [1,6–8].

The intellectual contributions of countless pioneers have enriched the legacy of this monumental achievement [9], including Emmett et al. [10,11] for their work on adsorption and catalyst design, particularly with iron-based catalysts; Mittasch et al. [8,12] for their exploration of osmium-, uranium-, and fused Fe-based catalysts; and Ertl et al. [13,14] for their groundbreaking contributions to understanding surface reactions at the atomic level.

Aika and Ozaki et al. [15,16] expanded the horizons of ruthenium and other transition metal catalysts, opening up the possibility of more efficient processes under milder conditions than iron-based catalysts. Somorjai et al. [17,18] added to our fundamental understanding of the role of promoters in iron-and ruthenium-based catalysts. Nørskov et al. [19–21] made significant conceptual contributions to heterogeneous catalysis, particularly concerning the volcano plot and the Brønsted–Evans–Polanyi relation

that links kinetics (activation barriers) with thermodynamics (reaction enthalpies) [22,23]. Hosono et al. [24–27] have continued to inspire the field through their exploration of transition metal nitride-, hydride-, and electride-based catalysts, aiming to improve the energy efficiency of the process and reduce the harsh conditions required in traditional methods for ammonia synthesis. Taylor's theory of catalytic surfaces [28], Boudart's work on the paradox of heterogeneous kinetics [29–31], Temkin and Pyzhev's [31] adsorption isotherm theory—subsequently applied to the performance of a Haber–Bosch reactor across a wide range of operating conditions by Krewer et al. [32]—which emphasizes nitrogen adsorption on the catalyst surface, and its correction for diffusion by Dyson and Simon [33] and Stoltze et al. [34,35], have all significantly advanced the field. Spencer's work on chemical kinetics and mixed alloy catalysts [36–38], Bowker's development of rate equations assuming dissociative hydrogen adsorption in two steps, along with several hydrogenation steps [39], and Brill's concept of poisoning in ammonia synthesis [40] have further shaped our understanding of the ammonia synthesis activity process.

The reaction between nitrogen and hydrogen gases in a 1:3 ratio is exothermic [41,42].

$$N_2\,(g) + 3H_2\,(g) \rightleftharpoons 2NH_3\,(g),\ \Delta H = -92\ kJ/mol \quad (1)$$

The Haber–Bosch process for ammonia synthesis operates under extreme conditions, with temperatures of 375–500 °C and pressures of 200–300 atm [43]. These conditions are necessary to overcome the high activation energy barrier of $N_2$ bond dissociation (941.4 kJ $mol^{-1}$ [44]), but they also demand substantial energy input (~485 kJ $mol^{-1}$). Despite its significance, the process remains challenged by energy efficiency and catalytic performance limitations. Consequently, ongoing innovation aims to enhance sustainability and efficiency for future generations [41]. At the heart of these advancements is the pursuit of novel catalysts capable of operating at significantly lower temperatures and pressures, reducing the need for energy-intensive compression and ushering in a new era of energy-efficient ammonia synthesis.

For decades, it was unclear whether adsorbed hydrogen atoms interacted with nitrogen in its atomic or molecular form on the catalyst surface. An Auger spectroscopy study [45,46] resolved this uncertainty by revealing that the density of adsorbed atomic nitrogen sharply decreases at elevated hydrogen pressures. This insight enhances our understanding of the adsorption process: at low pressure, hydrogen and nitrogen are weakly to moderately adsorbed onto the catalyst surface [9,11]. As both pressure and temperature increase, these molecules undergo dissociative adsorption, with hydrogen dissociating more rapidly than nitrogen. This differential behavior is pivotal for the subsequent reaction step.

Central to the Haber–Bosch process is the use of a metallic catalyst to drive reaction (1). Typically, the metal starts in a mixed-oxidation state—often as iron oxides like $Fe_3O_4$. In the initial step, gaseous $N_2$ and $H_2$ molecules adsorb onto the catalyst surface even if it is not fully reduced. The efficiency of N≡N bond cleavage, however, depends critically on the catalyst's reduction state.

Once the catalyst is fully reduced to its metallic form ($Fe^0$ [10,47] and $Ru^0$ [48]), it facilitates the thermodynamically favorable chemisorption of two N atoms onto two separate sites ($N_2 \rightarrow 2N$) [31]. These reactive sites are limited by the number of vacant adsorption sites available on the surface [28]. If the catalyst remains poorly reduced, the chemisorbed $N_2$ first reacts with adsorbed hydrogen to form a less stable N–NH (or HN–NH) intermediate, which then dissociates into adsorbed NH radical intermediates. This sequential reduction is essential for effective interactions between the adsorbed nitrogen and hydrogen atoms, ultimately leading to ammonia formation [8,49,50].

Moreover, the catalyst's microstructure—comprising metal particles interspersed with unreduced oxides or nitrides—promotes the formation of metal–nitrogen intermediates [51], thereby enhancing catalytic efficiency.

A crucial aspect of the Haber–Bosch process is identifying the rate-determining step (RDS) [24,26,32,52,53]—the slowest step that governs the overall reaction rate on transition metal catalysts [49,50], such as Fe and $Fe_2O_4$ [54,55]. Traditionally, this step was attributed to the dissociative adsorption of $N_2$ [25,32,42,56,57], a concept first proposed by Emmett and Brunauer [11]. However, recent studies highlight that the RDS can vary depending on reaction conditions, catalyst composition, and the influence of structural [58] and electronic promoters [52,59–62]. Advances in catalyst microstructural analysis and promoter effects have refined our understanding of the high-temperature dissociative pathway [63], while also pioneering alternative reaction mechanisms. These insights enable more efficient ammonia synthesis under milder conditions [64] by leveraging associative, alternating, or distal enzymatic hydrogenation mechanisms, ultimately enhancing control over the hydrogenation process [65].

Transition metal catalysts—such as Fe, Co, Mo, and Ru [66–69]—alone are often insufficient for efficient ammonia synthesis. To enhance their performance, they are typically paired with either structural or electronic promoters. Electronic promoters, including alkali, alkaline earth, or lanthanide metals (or their oxides and hydrides), improve catalytic activity by modifying the electronic environment. For example, Fe-based catalysts combined with $Al_2O_3$ and $K_2O$ exhibit enhanced $N_2$ triple bond cleavage and reduced bond dissociation energy [12,61,70,71]. $Al_2O_3$, a structural promoter, prevents sintering by spacing small iron platelets and may also stabilize Fe(111) facets, optimizing catalytic performance. By contrast, $K_2O$ functions as an electronic promoter by facilitating charge transfer to the transition metal surface, altering reaction orders for ammonia and hydrogen [72], and lowering the activation energy for $N_2$ dissociation—ultimately increasing ammonia synthesis rates [58,73]. Strongly basic supports such as $CeO_2$, $La_{0.5}Pr_{0.5}O_{1.75}$, $Ba/Ce_{0.5}La_{0.5}O_{1.75}$, $CeO_2$-$PrO_x$, and $Ce_{0.5}La_{0.5-x}Ti_xO_{1.75+0.5x}$, contribute to the promotion of $N_2$ dissociation. They enhance the transfer of electron density from Ru to the antibonding orbital of $N_2$, facilitating the dissociation process [74].

Barium, as an electronic promoter, is believed to modify surface morphology by forming highly active B5-type sites on Ru catalysts, thereby enhancing catalytic efficiency [75]. In the case of a $Ru/Sr_2Ta_2O_7$ catalyst, ammonia synthesis activity correlates with the electron donation capacity of alkali and alkaline-earth promoters, Cs > Rb > K > Ba [76]. Some studies further identify Cs as the strongest electron donor, while BaO primarily functions as a hydrogen scavenger [77]. The promoting mechanism and activity can vary depending on metal-oxide combinations, with hydroxide promoters exhibiting effectiveness in the order $Cs_2O > K_2O > Na_2O > BaO > CaO$ [78]. Under specific conditions, these promoters can shift the rate-limiting step from $N_2$ dissociation to hydrogenation processes, such as the hydrogenation of nitrogen intermediates or ammonia desorption. In the case of the promoters K, Cs, Ba, and Li, the reactivity order for promoted $Ru/La_2Ce_2O_2$-suppoted catalysts has been reported as K > Cs > Ba > Li (at 400 °C and 1 MPa), which contradicts the order based on the electronegativity of the promoters (Li > Ba > K > Cs) [48]. Furthermore, it has been shown that anchoring Ba and/or Ce onto Ru atomic cluster catalysts (ACCs) significantly enhances the catalytic $N_2$-to-$NH_3$ conversion, boosting the rate of $NH_3$ synthesis to 56.2 mmol $NH_3$ $g_{at}{}^{-1}$ $h^{-1}$ at 400 °C and 1 MPa—7.5 times higher than that of Ru ACC alone [79].

This overview summarizes studies investigating how the rate-determining step changes across various catalysts—including Fe, Co, Ru, and transition metal alloys—and how these variations influence activation energy [59]. We begin by analyzing the activation

sites on selected crystal phases of these metals, focusing on both molecular and dissociative adsorption states, as well as activation profiles and energies, typically characterized using experimental techniques and/or theoretical approaches such as density functional theory (DFT) [80,81]. The discussion highlights key catalyst systems where specific elementary reaction mechanisms contribute to a deeper understanding of $N_2$ decomposition in ammonia synthesis. Additionally, we explore the effects of promoter incorporation on catalytic performance, wherever applicable, and assess recent progress in establishing a qualitative relationship between reaction order and the RDS. This overview provides a concise perspective on the research required to advance catalytic design, improve efficiency, and enhance the sustainability of ammonia synthesis.

## 2. Catalytic Surface Reactivity Through the Lens of Geometry: Adsorption Site Topologies and Their Role in Heterogeneous Catalysis

In the microscopic realm of catalysis, it's not pristine perfection but structural irregularity that gives rise to exceptional reactivity, as discussed by Taylor [28], whose view ultimately proved more accurate than Langmuir's earlier perspective [82]. Catalysts operate most effectively when their surfaces are not flat and featureless but instead exhibit irregular contours—ridges, ledges, and atomic-scale discontinuities (defects). These imperfections serve as active zones that can transiently capture and orient reactant molecules, enhancing their likelihood of undergoing transformation. On such surfaces, molecules are not evenly spread or randomly placed—they gravitate toward specific topological features where the (adsorption) binding energy is most favorable.

Ruthenium commonly exhibits two principal surface structures: flat terraces [83,84] and step edges [85–87]—features that may also be characteristic of cobalt surfaces. Typical adsorption sites on the flat surface include on-top (t), bridge (b), face-centered cubic (fcc/FCC), hexagonal close-packed (hcp/HCP), as illustrated in Figure 1a,b. Wulff constructions of hcp metals such as Ru and Co nanoparticles typically feature dominant facets including the basal plane (0001), the prismatic plane $(10\bar{1}0)$ and the vicinal stepped surface $(10\bar{1}1)$. The latter corresponds to a vicinal plane inclined from the basal plane and features regular monatomic-height steps. These facets are energetically favorable and are commonly observed in both experimental and theoretical studies of hcp metal nanoparticles and single crystals [88].

The B5 adsorption site [89,90] is of particular catalytic significance. Found predominantly on Ru(0001) and Co(0001) step edges, the B5 site comprises five metal atoms: two at the step edge and three on the adjoining terrace, arranged in a distinctive configuration. This geometry provides an energetically favorable environment for adsorption, enabling the site to stabilize reactant species just long enough to facilitate key chemical transformations—thereby making it highly active in catalytic processes. Figure 1b,c illustrate a stepped surface of hcp Ru featuring the B5 site that consists of five Ru atoms arranged to expose both a three-fold hollow (hcp) site and a nearby bridge site in close proximity, analogous to that reported elsewhere [91].

The fcc(211) and bcc(310) surfaces are prototypical stepped terminations that inherently expose B5-active sites due to their distinct atomic arrangements. By contrast, flat surfaces such as hcp(0001) or fcc(111) lack the necessary step or kink features to host B5 sites. However, fcc(111), while atomically smooth, may be used to construct vicinal surfaces like fcc(211) through directional cleaving, thereby introducing step edges where B5 geometries can emerge. Similarly, if an Ru(0001) slab is constructed from a cubic lattice or any non-hexagonal surface, B5 sites potentially can still form, provided that step edges are introduced and the local atomic arrangement supports the specific fivefold geometry required for a B5 site (Figure 1b). The hexagonal Co$(10\bar{1}5)$ and Ru$(10\bar{1}5)$ facets have

been reported to display step structures [92], a member of the (10$\bar{1}$*l*) (l=1-9) family. These surfaces are vicinal to the (0001) plane, with terraces aligned along the [12$\bar{1}$0] direction and increasing step height as *l* increases. The Ru(11$\bar{2}$*l*) (*l* = 1-3) surfaces may have slightly different terrace orientations and compared to Ru(10$\bar{1}$5), with higher densities of steps or kinks, and could display more complex step-edge geometries due to the increasing step height and terrace misalignment.

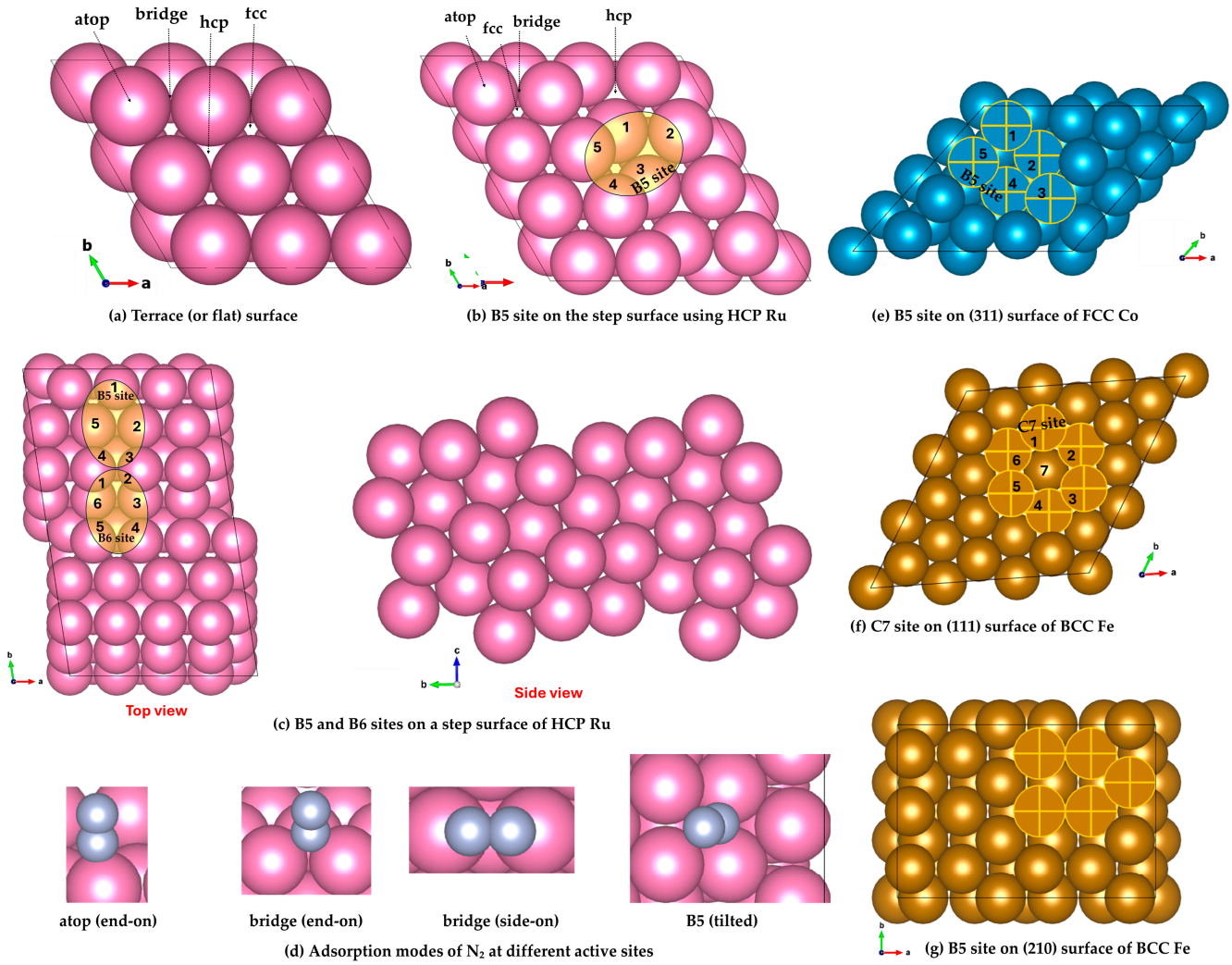



**Figure 1.** (**a**,**b**) Illustration (top view) of common adsorption sites on the flat/step HCP(0001) surface of Ru (space group: *P*$6_3$/*mmc*), including on-top (directly above a surface atom), bridge (between two adjacent atoms), face-centered cubic (fcc) hollow, and hexagonal close-packed (hcp) hollow sites. The fcc site is a threefold hollow site where the adsorbate sits above a triangle of atoms stacked in an fcc-like sequence, typically found on (111) surfaces of fcc metals. The hcp site is also a threefold hollow, but lies above atoms following an hcp stacking, characteristic of hcp metals like Ru. (**b**) Manual construction of a monoatomic step surface on Ru(0001) by selectively removing two rows of atoms from the top layer; this approach does not involve the use of a Wulff construction. (**b**,**c**) The B5 site is a step-edge site on a stepped Ru surface, composed of five metal atoms—two from the step and three from the terrace—within an hcp lattice. This site is well-known for its catalytic role in ammonia synthesis. (**c**) Marking of the B5 and B6 sites on a step surface of HCP Ru; the slab is shown from two different perspectives. (**d**) Schematic illustrations of different adsorption modes of molecular $N_2$ on various surface sites of Ru. Illustrations of the B5, C7, and B6 adsorption sites on the (311), (111), and (210) surfaces of FCC Co and BCC Fe are shown in panels (**e**), (**f**), and (**g**), respectively. Atom colors: Ru—pink; Co—deep cyan; Fe—deep orange; N—light blue.

The B6 adsorption site—consisting of a six-atom cluster made up of two step-edge atoms and four terrace atoms—has been identified on Ru catalysts but remains relatively underexplored as a potentially active adsorption site [90]. Structurally, it can be viewed as a distorted octahedral cavity, as may be inferred from Figure 1c. B-active sites, which are not always readily observed on small nanoparticles (NPs), become more apparent on large-sized, highly reactive NPs and can be tracked using Wulff construction in combination with first-principles calculations [90].

Zeinalipour-Yazdi's study investigated the diversity of local active site geometries on metal NPs and the surfaces of FCC and HCP metals [93]. As many as 18 local site geometries were characterized in HCP and FCC structures. These adsorption sites can be described by combinations of equilateral triangles and squares, with atoms adopting either bridge or atop bonding conformations. The geometries are further distinguished by their alignment above tetrahedral or octahedral hollows. Notably, the study proposed that the well-known B5 site (equilateral-triangle-square with a common side)—previously identified as catalytically active in ammonia synthesis and decomposition—may exist in five structural variants, depending on the angle between the triangular and square motifs. While this classification had not been explicitly formalized before, certain configurations, such as the 3f(T)-b-4f-234.7° site, had already been labeled as B5-sites [94] and shown to play a crucial role in ammonia synthesis [91] and decomposition [85] on Ru step surfaces. Four additional variants have been identified and labeled as 4f-b-3f(O)-200.7°, 3f(O)-b-4f-125.3°, 3f(T)-b-4f-164.2°, and 3f(T)-b-4f-125.3°, where "O" and "T" denote local octahedral and tetrahedral voids in ABAB (HCP) and ABCA (FCC) lattices, respectively. The angle appended to each label represents the geometric relationship between the equilateral triangle and square motifs that define the local adsorption site. For instance, the 3f(T)-b-4f site consists of a tetrahedral motif and a square pyramidal structure, connected through shared triangular facets. This configuration forms a distinct angle of 234.7°, giving rise to the specific designation 3f(T)-b-4f-234.7°. Such a site is located above a tetrahedral hole and can be found on both HCP and FCC NPs.

The C7 site is a catalytically active seven-atom cluster located at step edges or kinked regions of Fe surfaces, such as Fe(111) or Fe(211), which commonly arise in nanostructured or roughened iron catalysts. Here, "C" may stand for "cluster" or "coordination", and "7" refers to the number of surface atoms involved in forming the site—specifically, seven iron atoms, depending on context. As such, the site consists of three atoms from the upper terrace, three from the lower terrace, and a single atom at the step edge, forming a unique geometry that offers undercoordinated iron atoms. This arrangement creates an ideal environment for nitrogen activation, making the C7 site a key player in the rate-limiting $N_2$ dissociation step during ammonia synthesis [95,96]. To capture the diversity of iron surface structures, Zhang et al. [97] have explored low-index facets with Miller indices satisfying $h + k + l \leq 5$ and $h \leq 3$. In addition to the widely examined (111) and (211) facets, the (221), (311), (310), and (210) surfaces expose catalytically relevant C7 and/or B5 sites. Notably, the (111), (221), (311), and (211) surfaces all host C7 sites, with Wulff construction indicating that (211) contributes the largest surface area among them. Illustrations of the B5 and C7adsorption sites on the (311), (111), and (210) surfaces of FCC Co and BCC Fe (see Figure 1e–g).

Figure 1d illustrates the various adsorption configurations of molecular $N_2$ often examined on transition metal surfaces [98]. These configurations—such as atop end-on (vertical), bridged end-on, bridged side-on (horizontal), and tilted—reflect the diversity of local coordination environments. The specific mode of $N_2$ binding depends on the electronic structure and topology of the adsorption site, both of which vary across catalyst

materials and surface terminations. These differences influence the binding strength and activation of $N_2$, playing a critical role in catalytic performance.

## 3. The Activation Energy, $E_a$

The activation energy ($E_a$), a key kinetic parameter in ammonia synthesis, is widely examined in both experimental and theoretical studies [24,26,52,53,99–104]. It governs the rate constant $k$ through the Arrhenius equation $k = A\, e^{-Ea/RT}$, where A is the pre-exponential factor, which represents the frequency of molecular collisions, while the other symbols have their usual meaning. $E_a$ is often discussed in relation to rate-determining or rate-limiting steps and corresponds to the energy required to transition from reactants to the high-energy transition state (TS). Overcoming this energy barrier is crucial for breaking the strong N≡N triple bond in molecular nitrogen and activating nitrogen atoms for subsequent reactions. It also applies to overcoming barriers in forming intermediates via hydrogenation and facilitating desorption, ultimately leading to ammonia production [105].

Despite nearly a century of advances in experiments, theory, and catalyst development, a complete mechanistic understanding of activation profiles and their relationship to the RDS in ammonia synthesis remains elusive—posing both a challenge and an opportunity for the rational design of next-generation catalysts. [106].

In heterogeneous catalysis, activation energy is influenced by the catalyst's properties, including its electronic structure, surface morphology, and interactions with reactants. These factors facilitate adsorption, dissociation, and subsequent reaction of molecular species. Lower activation energy leads to a faster reaction rate, enhancing $NH_3$ production and overall catalyst efficiency. For instance, the Ru SAs/S-1 catalyst [107] exhibits an apparent activation energy of 0.57 eV (55 kJ $mol^{-1}$) for the reaction $N_2 + H_2 \rightarrow N\text{-}NH_2$ [77], as determined from an Arrhenius plot. Similarly, the $E_a$ for $N_2 \rightarrow 2N$ on $Ca_3CrN_3H$ is 0.777 eV (75 kJ $mol^{-1}$) [108], comparable to other hydride-based catalysts such as $BaTiO_{3-x}H_x$ (80 kJ $mol^{-1}$) [103], and $BaCeO_{3-x}N_yH_z$ (72 kJ $mol^{-1}$) [109], and significantly lower than conventional Ru-based catalysts (85–121 kJ $mol^{-1}$) [109]. $E_a$ values for various transition-metal-based catalysts are given in Table 1.

Using the most stable $N_2$ adsorption geometry as the initial state of an NEB simulation, Zhang et al. [97] theoretically examined $N_2$ dissociation on eight Fe surfaces. Facets exposing C7 sites—(111), (221), (311), and (211)—that demonstrated consistently high activity, with activation energies narrowly ranging from −0.35 to −0.45 eV, in the order: (111) > (221) = (311) > (211). By contrast, (210) and (310), which lack well-defined C7 sites, showed lower activity (activation energies between −0.16 and −0.14 eV), while (100) and (110) exhibited the highest barriers (0.10 and 0.26 eV). These findings clearly highlight the critical role of active site geometry in governing $N_2$ activation and, by extension, ammonia synthesis efficiency.

**Table 1.** Reported catalysts, rate-determining steps, reaction mechanism type, and apparent activation energies (wherever available), including the reaction mechanism, wherever feasible.

| Catalyst | Rate-Determining Step | Mechanism | Activation Energy/eV |
|---|---|---|---|
| Ru | $N_2 \rightarrow 2N$ | Dissociative | 0.881–1.254 [108,110] |
| $Ru/MgO$; $Ru/Al_2O_3$ | $N_2 \rightarrow 2N$ | Dissociative | 1.638 [62] |
| Fe (commercial) | $N_2 \rightarrow 2N$ | Dissociative | 0.725 [111,112] |
| $Ru/Sm_2O_3$ | $N_2 \rightarrow 2N$ | Dissociative | 1.30 [113] |
| $Co/Ba/La_2O_3$ | $N_2 \rightarrow 2N$ | | 0.474–0.758 [114] |
| $Co_3Mo_3N$ | $N + H_x \rightarrow NH_x$ (x = 1–3) | ER/MvK [115,116] | 0.58 [27] |
| $Ru/CeO_2$ | $N_2 + H \rightarrow N + NH$ | Associative | 0.85 [117] |
| $Ca_3CrN_3H$ | $N_2 + H \rightarrow N{=}NH$ | Associative alternating | 0.777 [108] |
| $BaTiO_{3-x}H_x$ | | | 0.829 [108] |
| $BaCeO_{3-x}N_yH_z$ | | | 0.746 [108] |
| Cs−Ru/MgO | | | 1.244 [117] |

**Table 1.** *Cont.*

| Catalyst | Rate-Determining Step | Mechanism | Activation Energy/eV |
|---|---|---|---|
| Ru/C12A7:$e^-$ | $N + H_x \rightarrow NH_x$ (x = 1–3) | | 0.508 [118] |
| Ru/$[Ca_{24}Al_{28}O_{64}]^{4+}(O_2^-)_2$ | $N + H_x \rightarrow NH_x$ (x = 1–3) | | 1.078 [75] |
| Ru/$[Ca_{24}Al_{28}O_{64}]^{4+}(O_2^-)_{2-x}$ $(e^-)_{2x}$ | $N_2 \rightarrow 2N$ | | 0.518–0.622 [75] |
| Ru−Cs/$[Ca_{24}Al_{28}O_{64}]^{4+}(O_2^-)_2$ | $N + H_x \rightarrow NH_x$ (x = 1–3) | | 1.171 [75] |
| Ba-Co/C | | | 0.954 [119] |
| Co@BaO/MgO; Co/Ba/MgO; Co/MgO | $N_2 \rightarrow 2N$ | | 0.538; 0.803; 0.833 [120] |
| Ru/CaFH | $N_2 \rightarrow 2N$ | | 0.207 [101] |
| Ru/Ba–$Ca(NH_2)_2$ | $N + H_x \rightarrow NH_x$ | | 0.425 [121] |
| LaCoSi | $N + H_x \rightarrow NH_x$ (x = 1–3) | | 0.435 [106] |
| Ru/$Ca_2N$:$e^-$ | | | 0.622 [24] |
| Ru–Cs/MgO | | | 1.244 [24] |
| Ru/CaNH | | | 1.14 [24] |
| Ru/$CaH_2$ | | | 1.244 [24] |
| $BaH_2$-BaO/Fe/$CaH_2$ | | | 0.415 [122] |
| Ru/Ba−$Ca(NH_2)_2$ | | | 0.456 [121] |
| Ru/Ba–$Ca(NH_2)_2$ | | | 0.611 [102] |
| Ru/BaO–$BaH_2$ | $N + H_x \rightarrow NH_x$ (x = 1–3) | Anticipated from reaction order | 0.425 [121] |
| Ru/$La_{0.5}Ce_{0.5}O_{1.75}$_650red | $N_2 \rightarrow 2N$ | | 0.663 [123] |
| Ru/Ba–$LaCeO_x$_$Ru_3(CO)_{12}$ | $N_2 \rightarrow 2N$ | | 0.705 [124] |
| Ru/Ba–$LaCeO_x$_ALD | $N_2 \rightarrow 2N$ | | 0.622 [124] |
| Ru/Ba–$LaCeO_x$_$RuCl_3$ | $N_2 \rightarrow 2N$ | | 0.736 [124] |
| Ru-Ba/MgO | | | 0.435 [125] |
| Ni/LaN; Ni/CeN NPs | $N + H \rightarrow NH$ | | 0.596 [27]; 0.556 [27] |
| Ru/$CaH_{1.72}O_{0.14}$ | | | 0.715 [126] |
| Ru/$CaH_{1.5}0O_{0.25}$ | | | 0.611 [126] |
| Ru/$CaH_{1.12}O_{0.44}$ | | | 0.829 [126] |
| $CeNi_2$ | $N + H_x \rightarrow NH_x$ (x = 1–3) | Anticipated from reaction order | 0.573 [127] |
| $CeNi_5$ | $N_2 \rightarrow 2N$ | Anticipated from reaction order | 0.824 [127] |
| CeN NPs | | | 0.586 [27] |
| Ru/$BaAl_2O_{4-x}H_y$ | $N_2 \rightarrow 2N$ | | 0.681 [128] |
| Co/C | | | 1.544 [111] |
| $Ba_{0.8}Co_{1.0}$/C | | | 1.068 [111] |
| Co-Mo(5:5)/$CeO_2$ | | | 0.591–0.632 [129] |
| 10%Cs–FePc; FePc; CoPc | $N_2 \rightarrow 2N$ | Dissociative | 0.435; 0.434; 0.631 [112] |
| Co/$BaAl_2O_{4-x}H_y$ | $N_2 \rightarrow 2N$ | Dissociative | 0.514 [128] |
| Co/$BaAl_2O_4$ | $N_2 \rightarrow 2N$ | Dissociative | 1.042 [128] |
| Fe/$Ce_{1-z}Sm_zO_{2x}N_y$ | $N_2 \rightarrow 2N$ | Dissociative | 0.466 [130] |
| Fe/$CeO^{2-x}N_y$ | $N_2 \rightarrow 2N$ | Dissociative | 0.518–0.684 [130] |
| Cr–LiH | $N + H_x \rightarrow NH_x$ (x = 1–3) | | 0.659 [131] |
| Mn–LiH | $N + H_x \rightarrow NH_x$ (x = 1–3) | | 0.524 [131] |
| Fe–LiH | $N + H_x \rightarrow NH_x$ (x = 1–3) | | 0.482 [131] |
| Co–LiH | $N + H_x \rightarrow NH_x$ (x = 1–3) | | 0.540 [131] |

## 4. The Activation Energy Profile

In Figure 2a, the energy profile illustrates a typical case of $N_2$ decomposition ($N_2 \rightarrow 2N$ [132]) via the Langmuir–Hinshelwood (LH) mechanism [133], where the reaction enthalpy ($\Delta H$) is exothermic. Here, $\Delta H$ is defined as $\Delta H = E(\text{product}) - E(\text{reactant})$, with $E$ referring to the total electronic energy of each individual state. On the surface of Fe, however, this reaction is endothermic, despite the overall ammonia synthesis reaction ($N_2 + 3H_2 \rightarrow 2NH_3$) being exothermic [134].

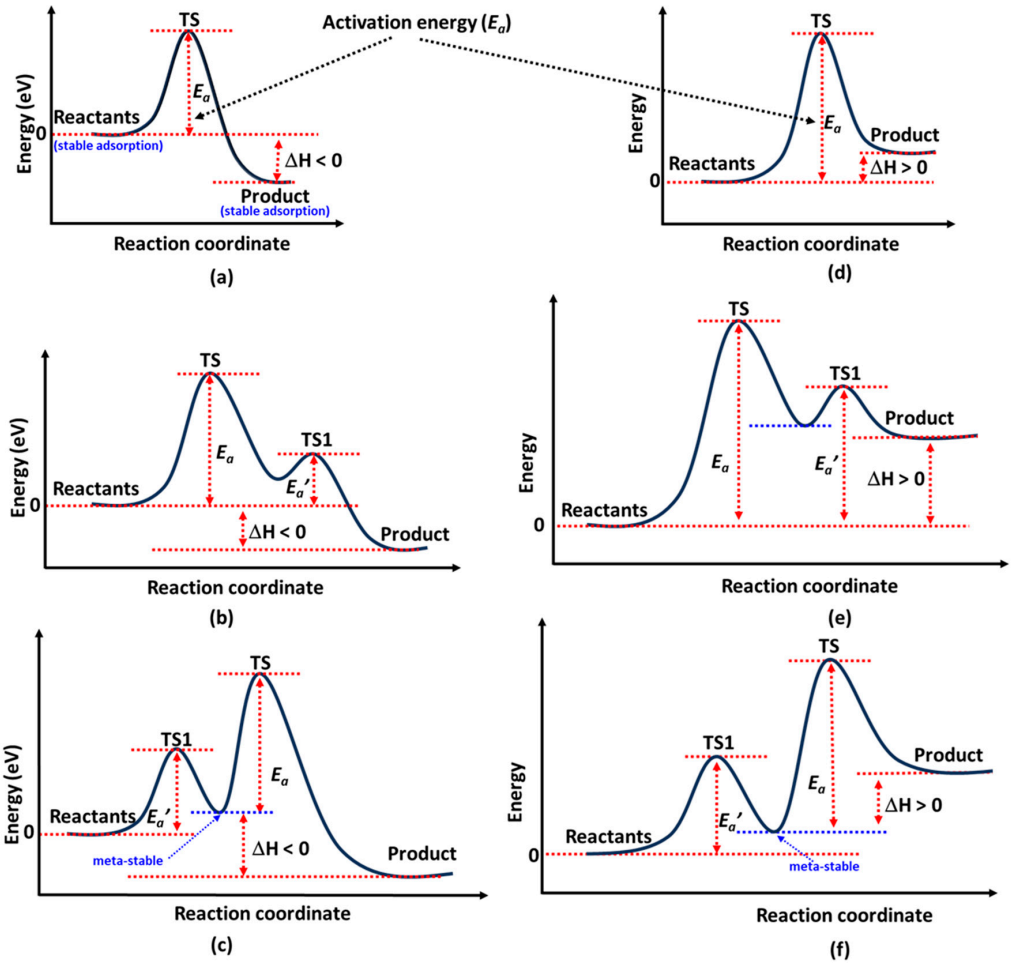



**Figure 2.** (**a**–**f**) Schematic representation of the energy of activation as a function of reaction coordinate. TS and TS1 are transition states, $\Delta H$ is the reaction enthalpy, and $E_a$ and $E_a'$ are the activation energies. The label at '0' energy corresponds to the reference point. The peaks representing $E_a$ correspond to the actual transition states.

In Figure 2b an energy profile is shown where a promoter on the catalyst obstructs reactants, hindering their ability to find an immediate optimal pathway to the product state. The transition state (TS), representing the highest energy point, corresponds to the activation energy ($E_a$).

Shown in Figure 2c is the profile that arises when a reactant, such as $N_2$, undergoes an orientational transformation (e.g., from end-on to side-on) on the catalyst surface before forming the product state (2N). Here, $E_a'$ represents the activation energy, and TS1 appears if the reactants pass through a quasi-stable intermediate state. This intermediate is likely to form when an active site near the reaction pathway influences the product before it reaches its most stable configuration at the most favorable active site on the catalyst surface.

For catalysts such as hexagonal Co or Ru, $N_2$ is exothermically adsorbed in an end-on configuration atop a Co [135] or Ru [136,137] atom. By contrast, the sideways (or side-on) configuration at an hcp site is a well-activated but metastable state [65] characterized by weaker adsorption. For example, at the PW91 level of theory, the reported adsorption energies of $N_2$ on Ru(0001) are −0.74 eV and −0.24 eV for top and hcp sites, respectively [138]. Zhang et al. [135] reported PBE-level adsorption energies for different sites, ranging from −0.46 to −0.67 eV for hcp Co and −0.42 to −0.61 eV for fcc Co. This behavior contrasts with the binding affinity of $N_2$ at the vacant site on a $Co_3Mo_3N(111)$ catalyst, where adsorption

is endothermic [139,140] ($E_{ad}$ = 0.415 eV [115], a trend similar to that observed for other metal nitrides, viz. $Mn_6N_{5+x}$ and η-$Mn_3N_2$ [99].

Assuming the side-on configuration corresponds to the reactant and the 2N configuration represents the product, the latter part of the reaction profile in Figure 2c would result, with $E_a$ denoting the activation barrier. Most studies classify this metastable initial state as the reactant [141], and the activation energy between it and the product state is commonly reported [136]. As a result, the reaction energy profile is often depicted with a single activation barrier, rather than showing two distinct transition states. This explains why side-on $N_2$ adsorption is frequently referenced in discussions of the LH mechanism [115]. $Co_3Mo_3N$ serves as a representative system where this behavior is clearly observed [115].

$N_2$ adsorbs in an end-on configuration before rotating into a side-on molecularly adsorbed state on CuNi(111) [142], following appropriate dissociatively adsorption states. Mortensen et al. [141] conducted a detailed DFT study on $N_2$ adsorption and dissociation on Fe(111), identifying four distinct molecular adsorption states. Three were end-on configurations (perpendicular or tilted) at different adsorption sites, while the fourth was a side-on orientation, where both nitrogen atoms interacted with the surface. The side-on state was found to be more stable than the end-on state, with dissociation proceeding through it as a precursor. However, this behavior differed for $N_2$ on a CuNi(111) catalyst, where end-on adsorption generally exhibited lower adsorption energy than the side-on mode [142].

The scenarios depicted in Figure 2d likely represent the hydrogenation process, where the reaction progresses through successive intermediate states. This interpretation is reasonable, as the formation of $NH_x$ ($x$ = 2, 3) intermediates may be kinetically hindered on the catalyst surface (e.g., Ru) at low temperatures [143], while the NH intermediate remains relatively stable [144]. In this context, the product state is thermodynamically less favorable ($\Delta H > 0$) than the reactant state, as observed for the Fe(111) catalyst in the reaction $NH_2 + H \rightarrow NH_3$ [145].

The reaction energy profile in Figure 2f suggests that a dissociatively adsorbed H atom, initially stabilized at a thermodynamically favorable site (e.g., an hcp site), migrates to a less favorable site (e.g., an fcc site, a bridge, or an on-top site [146]) along the hydrogenation pathway before recombining with the N adatom to form $NH_x$ species. Some of the scenarios illustrated in Figure 2 were demonstrated in ref. [142] for $N_2$ activation on a CuNi catalyst.

Abghouli et al. [147] reported that the adsorption of $N_2$ molecules and N atoms on clean transition metal nitride surfaces is typically endothermic, indicating high energy demands in the initial stages. Moreover, direct $N_2$ dissociation is hindered by substantial activation barriers exceeding 2 eV, posing a significant challenge for $N_2$ activation. By contrast, hydrogen-assisted $N_2$ activation via the associative Mars–van Krevelen (MVK) mechanism [148] (vide infra) is considerably more efficient, offering a viable alternative for facilitating $N_2$ dissociation.

To determine the activation energy profiles and locate the transition states for N≡N bond cleavage, $NH_x$ hydrogenation, and $NH_3$ desorption, the Nudged Elastic Band (NEB) method [149] is commonly used [115,150], with vibrational analysis confirming the identification of a saddle point. NEB constructs a series of intermediate "images" between the initial and final states of a reaction pathway, connected by virtual springs, and optimizes them to trace the minimum energy path (MEP). The method ensures that the images relax properly on the potential energy surface by applying forces perpendicular to the path, while maintaining appropriate spacing along the reaction coordinate.

To refine the transition state estimate, the Climbing Image NEB (CI-NEB [151]) method is often employed, as demonstrated in studies of catalysts such as $Fe_3Mo_3N$ [143], $FeN_4$ [152], $RuN_4$ [152], Co/MoC [153], and Ru-based TM@Ru(0001) (TM = Sc–Zn, Y–Cd)

single-atom alloys [154], among others [155]. In CI-NEB, the image with the highest energy is driven uphill along the reaction coordinate and relaxed in all perpendicular directions, allowing it to converge to the saddle point, corresponding to the true transition state, without requiring prior knowledge of its geometry. The activation profiles shown in Figure 2a–f may result from applying NEB and/or CI-NEB to the reactant and product states associated with $N_2$ dissociation and $NH_x$ formation.

The number of images used between reactant and product states typically ranges from three to ten [115,153,156]. For example, Zeinalipour-Yazdi et al. [115] first estimated the activation barriers associated with $N_2$ dissociation and $NH_x$ formation by employing both dissociative and associative mechanisms, using 10 images to capture the features of the potential energy surface. Once key intermediates were identified and fully optimized, a subsequent NEB calculation with three images was performed to locate the transition state more efficiently for the $Co_3Mo_3N$ catalyst [115].

## 5. Elementary Reaction Mechanisms and Reactant–Product Pairs for the Nitrogen Reduction Reaction (NRR)

Over time, various elementary reaction mechanisms for NRR have been proposed to elucidate the complex processes of adsorption, surface reactions, and desorption in catalysis [23]. These mechanisms include the conventional Haber–Bosch process [140,157,158], along with plasma-catalytic [159,160], photocatalytic [161], biocatalytic [162], and electrocatalytic approaches [163]. While these mechanisms can be dissociative, associative, or a combination of both [164], the last three primarily follow associative pathways for $N_2$ fixation, typically operating at ambient pressure (1 atm) and low temperatures [165,166] with distinct RDS and minimum-energy pathways [156].

The $H_2$ or $N_2$ molecule from its gaseous state can adsorb on the catalyst at vacant surface sites [167] in different orientations—end-on, side-on, on-top bridge, on-top hollow, hollow sideways, or tilted [135,141,146,168]. After $H_2$ dissociates on the catalyst, the chemisorption of atomic hydrogen onto the surface could occur with $\Delta H < 0$, whereas absorption into the catalyst's bulk is a process with $\Delta H > 0$ [169]. Hydrogen species (either $H_2$ or atomic H) can interact with adsorbed $N_2$ or N species through direct contact from the gas phase or via surface activation.

A variety of N≡N bond dissociation steps have been suggested to explain nitrogen reduction reaction associated with the RDS [145,170,171], shown in Figure 3a–h.

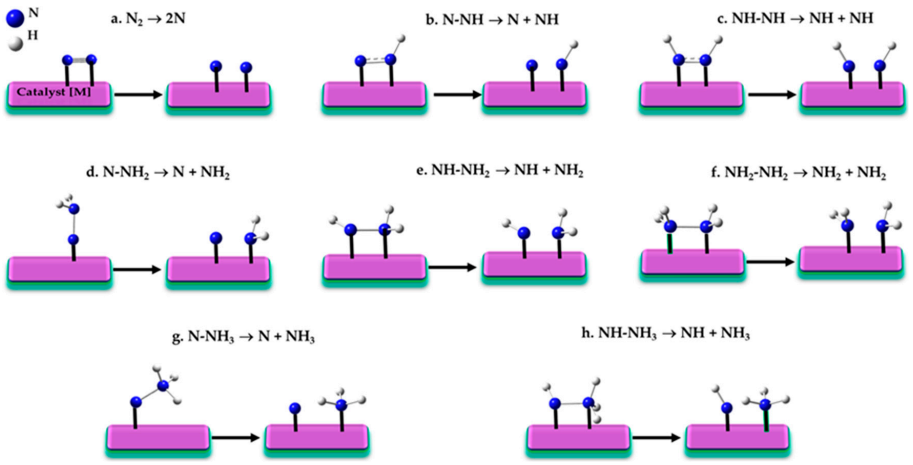



**Figure 3.** A schematic illustration of the possible dissociative pairs likely involved in the entire nitrogen reduction reaction (NRR) pathway on heterogeneous transition metal catalysts. These intermediates are central to NRR for Haber–Bosch catalysts and are likely to be relevant for photocatalytic and electrocatalytic processes [171].

If the initial stage of the reaction involves the dissociation of the N≡N triple bond ($N_2 \rightarrow 2N$; Figure 3a) under harsh conditions, a dissociative LH mechanism (vide infra) is typically considered operative [172,173]. This mechanism, first proposed by Langmuir in 1916 [174,175] and further developed by Hinshelwood in the late 1920s [176–179], depends on the catalyst's nature, as the energy barrier for $N_2$ dissociation can vary significantly. For instance, reported barriers range from 0.3 to 1.5 eV for different Miller index surfaces of Ru [180,181], 0.68 eV for Fe(111), 0.69 eV for K/Fe(111) [72,95], and between 0.55–1.37 eV for hcp Co and 0.64–1.39 eV for fcc Co [72,95].

If intermediate steps in N≡N dissociation involve partial hydrogenation, pathways like those in Figure 1b–f may arise. Back and Jung [171] demonstrated that reactant-product pairs such as $N_2 \rightarrow 2N$ (Figure 3a), N–NH → N + NH (Figure 3b), and HN–NH → 2NH (Figure 3c) exhibit significant activation barriers, often exceeding 1 eV, rendering these steps kinetically hindered. While the latter two steps belong to the associative $N_2$ fixation mechanism [165,166], Liu et al. [156] showed that the former step can occur after the first hydrogenation of $N_2$ on $Fe_3/\theta$-$Al_3O_3(010)$, leading to the dissociation of adsorbed N≡N into N and NH. This hydrogen-assisted $N_2$ dissociation route is an associative process, also observed in Ru NPs [113,182] and $Ru/CeO_2$ catalysts [117].

The structures of reactants, transition states, and products for N–N bond cleavage—illustrated in Figure 3a,b,e—were analyzed on the $Fe_2P(001)$ surface [183], revealing $N_2$ dissociation as the rate-limiting step. Various reaction mechanisms, including direct dissociative adsorption and stepwise associative pathways, were considered to capture the diversity of possible activation modes.

Back and Jung [171] further demonstrated that the dissociation steps $N–NH_2 \rightarrow N + NH_2$ (Figure 3d), $NH–NH_2 \rightarrow NH + NH_2$ (Figure 3e), and $NH_2–NH_2 \rightarrow NH_2 + NH_2$ (Figure 3f) have significantly lower activation barriers (<0.7 eV). These reduced barriers enhance the feasibility of these dissociation steps, making them more likely to occur under typical reaction conditions. This finding, along with results from other studies [115,150,184], may also extend to the reactant–product pairs in the reactions $N–NH_3 \rightarrow N + NH_3$ (Figure 3g) and $NH–NH_3 \rightarrow NH + NH_3$ (Figure 3h). In these cases, the favorable energetics of N–N dissociations [140] drive the overall reaction mechanism, promoting the reduction process at lower activation energies compared to the more challenging N≡N dissociation.

### *5.1. The Volcano Plot and Bronsted–Evans–Polanyi Relationship*

The volcano plot is a visual representation that captures the relationship between catalytic activity—such as turnover frequency—and the binding energy of a specific reaction intermediate. In the context of ammonia synthesis, this relationship typically balances nitrogen adsorption—neither too weak (hindering activation) nor too strong (impeding desorption)—and thus centers around the chemisorption energy of nitrogen species (N or $N_2$). A clear volcano-type trend, as illustrated in Figure 4a, has been established between nitrogen binding strength and catalytic activity [20], a relationship frequently referenced in catalyst screening studies [26]. This trend aligns with Sabatier's principle: optimal catalysts exhibit intermediate nitrogen adsorption, strong enough to activate $N_2$, but weak enough to permit subsequent hydrogenation and desorption. However, while useful for interpreting activity trends, this principle is often insufficient for guiding the rational design of optimal catalysts, as it overlooks the complexities of multistep reaction mechanisms and competing surface phenomena [185].

Metals on the left side of the volcano curve strongly adsorb nitrogen, leading to sluggish N–H bond formation and reduced ammonia synthesis rates. Conversely, metals on the right adsorb nitrogen too weakly, limiting $N_2$ activation and constraining overall efficiency. Near the volcano peak, metals like Fe, and Ru exhibit intermediate nitrogen binding, with

CoMo emerging as the most effective catalyst [186]. This optimal binding enhances nitrogen activation, facilitating efficient ammonia production. The superior performance of these metals is attributed to their favourable electronic properties, particularly the positioning of their d-band centres, which enable optimal interactions with nitrogen intermediates.

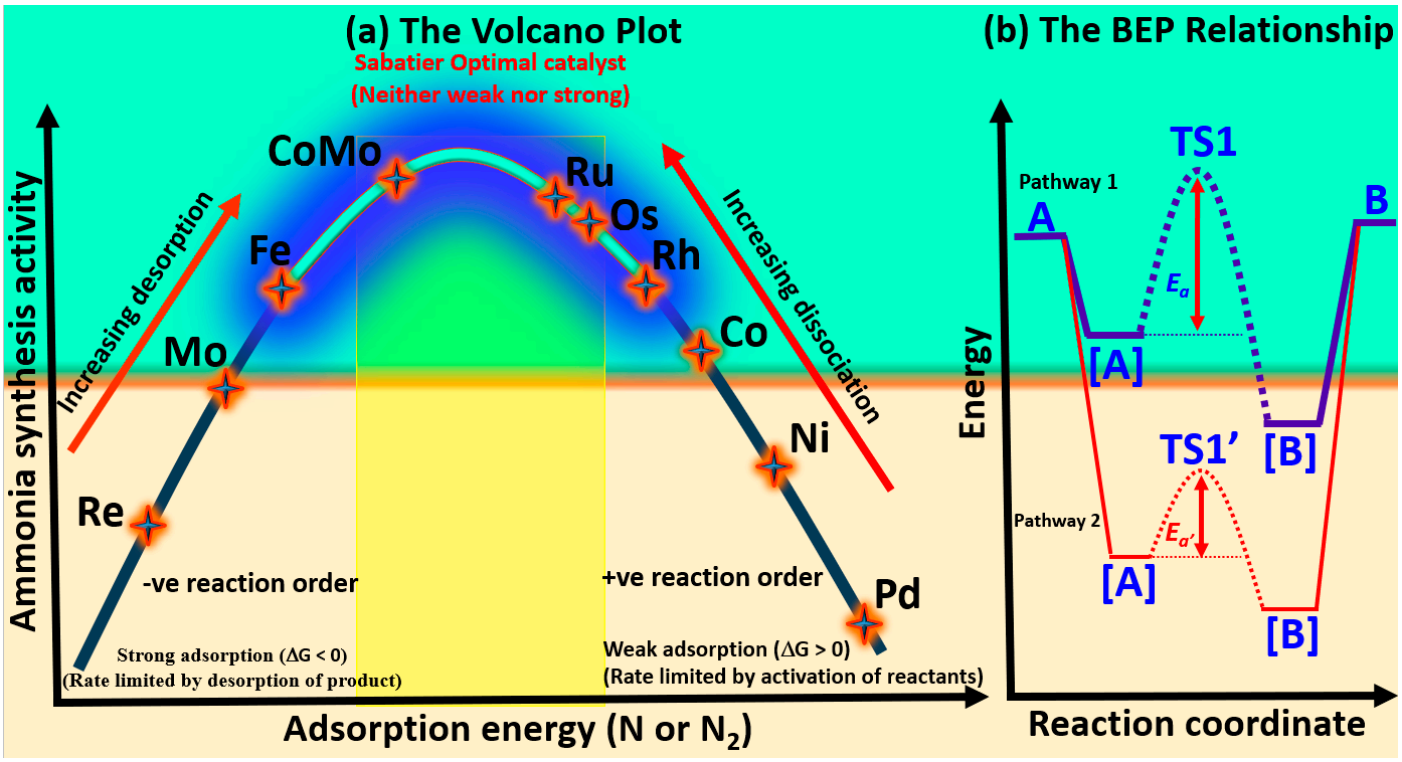



**Figure 4.** (**a**) Schematic representation of the widely used volcano plot illustrating the limitations of transition metal catalysts in ammonia synthesis. Δ*G* refers to the Gibbs free energy. Shown in (**b**) is the representation of the Brønsted–Evans–Polanyi (BEP) relationship (see text for description).

Nickel and cobalt generally exhibit lower catalytic activity compared to palladium-based systems. However, early transition metals such as Sc, V, Y, Ti, Zr, Nb, and Re demonstrate a stronger adsorption affinity for nitrogen relative to hydrogen, suggesting their potential suitability for nitrogen reduction reaction [171,187]. This preferential nitrogen binding behavior is probably advantageous in suppressing the competing hydrogen evolution reaction (HER), thereby enhancing selectivity toward ammonia production. Similar adsorption trends observed in thermocatalytic systems suggest that these metals could be promising candidates for both electrochemical and thermochemical ammonia synthesis.

On the other hand, the Brønsted–Evans–Polanyi (BEP) relationship [188] provides a widely used framework in heterogeneous catalysis, linking activation energies to reaction enthalpies through linear scaling. In many transition metal systems for ammonia synthesis, this implies that a single descriptor—often the nitrogen adsorption energy—can approximate the energetics of key steps, such as N≡N dissociation and N–H bond formation. Specifically, stronger adsorption of the N atom implies a lower $N_2$ dissociation barrier but higher $NH_x$ desorption energies, which is typically seen on metal surfaces like Re, Mo, and Fe. Conversely, weaker adsorption of the N atom results in a higher $N_2$ dissociation barrier and lower $NH_x$ desorption energies [156]. Thus, a good metal catalyst for ammonia synthesis must exhibit a moderate atomic N adsorption energy, located around the peak of the volcano plot. However, when $N_2$ hydrogenation becomes the dominant process, the N–N bond is significantly weakened, and the dissociation barrier no longer obeys the BEP relationship [189]. This alteration suggests that the BEP framework is more applicable in

the early stages of the reaction and may not fully capture its complexity in the later stages, where different factors influence the reaction. Furthermore, the BEP relation also imposes a trade-off: optimizing one step (e.g., $N_2$ activation) may adversely affect another (e.g., $NH_3$ desorption), as seen with metals like Ru and Ni. To overcome this constraint, recent efforts have focused on breaking such scaling relations through catalyst architecture innovations, including bifunctional sites, support effects, and single-atom alloys [190]. For example, Ru single atoms on Cu (Ru@Cu) have demonstrated the decoupling of $N_2$ activation and $NH_3$ release, offering a promising route to circumvent BEP limitations and achieve enhanced catalytic performance.

A reaction energy diagram comparing two surface-catalyzed pathways for the transformation of a gas-phase reactant (A) to a gas-phase product (B) via adsorbed intermediates ([A], TS1, [B]) is presented in Figure 4b. In Pathway 1, the energy ordering is A(gas) < [A] < [B], indicating that adsorption stabilizes the molecule progressively. Despite this thermodynamic favorability, the reaction proceeds through a high-energy transition state (TS1), resulting in a large activation energy barrier ($E_a$). In Pathway 2, both [A] and [B] are further stabilized (i.e., at lower energies than in Pathway 1), and the corresponding transition state (TS1′) lies at a lower energy, leading to a smaller activation barrier ($E_{a'}$). This trend agrees with the Brønsted–Evans–Polanyi (BEP) relationship, which correlates the stability of intermediates with reduced kinetic barriers. Thus, Pathway 2 is both thermodynamically and kinetically more favorable.

While both the volcano plot and the BEP relationship [188] are central in catalysis, they offer different perspectives on catalyst performance. The volcano plot emphasizes the balance between nitrogen adsorption strength and catalytic activity, visualizing how intermediate binding energies correlate with turnover frequency. On the other hand, the BEP relationship links activation energies to reaction enthalpies through linear scaling, where a single descriptor—typically nitrogen adsorption energy—can approximate the energetics of key catalytic steps like N≡N dissociation and N–H bond formation. Both frameworks are useful, yet each has its limitations. The volcano plot is often too simplistic for optimizing complex multistep processes, while the BEP relationship, though insightful, can result in trade-offs [191] between different multistep reaction steps, such as the competing needs for efficient $N_2$ activation and $NH_3$ desorption [23].

Breaking the inherent scaling limitations in transition metal (TM)-based catalysts has been a major challenge, particularly when catalysts exhibit a scaling relationship between the binding energies of reaction intermediates. Recent advances in catalyst design have shown that introducing a second active site can help overcome this constraint [131,192–194]. Specifically, pairing low-valent metal centers can exhibit cooperative behavior, enhancing reaction pathways in either stepwise or concerted manners. This cooperative effect often leads to more efficient reactant activation, mitigating the typical scaling limitations seen in single-metal catalysts.

Liu et al. [195] have shown that the $N_2$ dissociation barriers on Fe(111), Fe(211), Fe(110), and Fe(100) surfaces deviate from the conventional BEP trend. Specifically, Fe(111) exhibits both the weakest $N_2$ adsorption and the lowest dissociation energy barrier. This unexpected behavior is linked to electron transfer from the iron surface to the $\pi^*$ antibonding orbital of adsorbed $N_2$. Increased charge transfer into this orbital weakens the N≡N bond, thereby reducing the energy required to dissociate the N atoms. By contrast, the subsequent hydrogenation of N atoms and the desorption of $NH_3$ on these surfaces still conform to the BEP principle. Consequently, Fe(111) emerges as the most catalytically active surface for ammonia synthesis—a trend that also extends to similar surfaces of nickel and molybdenum.

A promising example of this approach is the use of bimetallic single-cluster catalysts (SCCs), denoted as $M_1M'_n$ (e.g., $Pt_1Co_n$), which have gained attention for their ability to activate reactants more effectively. For instance, Ma et al. [192] studied NRR over $Rh_1Co_3$ clusters supported on CoO(011), finding that the reaction mechanism in this system follows an associative pathway, similar to the highly efficient enzymatic nitrogen fixation found in nature. This biomimetic mechanism illustrates the potential of SCCs to enhance thermal $N_2$-to-$NH_3$ conversion and highlights new strategies for overcoming the limitations of traditional single-metal catalysts.

$Fe_3$ clusters supported on θ-$Al_2O_3$(010) activate $N_2$ via an associative *NNH intermediate rather than the traditional dissociative pathway, reducing the energy barrier beyond BEP expectations [196]. Phosphorus-modified $Fe_2P$(001) surfaces exhibit multiple N–N activation routes and altered $NH_x$ binding energies, defying the typical scaling behavior [183]. In Co/$BaCeO_3$ catalysts modified with yttrium, the enhanced performance could not be explained solely by $N_2$ adsorption energies, indicating additional electronic or structural factors are at play [197], which are not fully explained by traditional BEP scaling. Collectively, these studies demonstrate that while BEP offers valuable predictive insight, it often breaks down in the presence of defects, support effects, alternative mechanisms, or under non-equilibrium reaction conditions. This emphasizes the need for a more flexible framework in catalyst design.

### *5.2. The Dissociative Langmuir–Hinshelwood (LH) Mechanism*

Langmuir envisioned the reaction as unfolding through a series of dynamic, striking collisions [175,198], conceptualized in the following stages [199]:

(i) Reaction between adsorbed species and the surface: adsorbed species interact with the underlying surface through processes such as migration or diffusion [200]. These interactions modify surface structure and reactivity, influencing both reaction kinetics and catalytic performance.

(ii) Collision between gas molecules and adsorbed species: gas-phase molecules (e.g., $H_2$) collide with adsorbed species (e.g., N or $N_2$), transferring energy to surface-bound atoms and triggering catalytic transformations.

(iii) Interaction between adsorbed molecules/atoms: this occurs when adsorbed species on the surface interact with each other in adjacent spaces on the catalyst, forming intermediates that are crucial for the reaction.

Many studies [200–202] illustrate stage (iii), particularly in hydrogenation steps [62,203] such as $N + H \rightleftharpoons NH$, $NH + H \rightleftharpoons NH_2$, and $NH_2 + H \rightleftharpoons NH_3$. The process culminates in $NH_3$ desorption from the catalyst surface [204,205]. This associative sequence also defines the MvK mechanism [148]. By contrast, the LH mechanism follows a dissociative pathway [7,206,207] where reactants undergo dissociative chemisorption before interacting on neighboring sites, ultimately leading to $NH_3$ desorption [62].

Studies by Honkala et al. [110] and Strongin et al. [208] highlight the role of Ru's B5 sites [110] and Fe's C7 sites [208] as key active centers for $N_2$ adsorption and dissociation. Under ambient conditions, both $N_2$ and $H_2$ adsorb molecularly onto the catalyst surface [140,146,206,209,210], reaching equilibrium with the catalyst [199]. $N_2$ adopts a side-on orientation to enhance triple bond activation, while $H_2$ follows a similar pattern. Under harsh conditions, dissociative adsorption occurs, facilitated by electron density transfer from the catalyst substrate [211].

The Horiuti–Polanyi (HP) mechanism is a dissociative mechanism [212], primarily involving the homolytic (or heterolytic) dissociation of $H_2$ on the catalyst surface [213], such as Ag(211) and Ni(111) [214,215], with the dissociation step being the rate-determining step [216]. In the case of homolytic cleavage, the $H_2$ molecule splits evenly; each H adsorbs

onto the catalyst before participating in hydrogenation. In the case of heterolytic cleavage, $H_2$ splits unevenly, with one hydrogen atom adsorbing onto the metal surface, while the other adsorbs onto a heteroatom (such as nitrogen) on the catalyst [216].

The ammonia synthesis reaction, $N_2 + 3H_2 \rightleftharpoons 2NH_2$, proceeds via a series of elementary steps, a-o, on the catalyst surface, characteristic of the LH mechanism and illustrated in Figure 5a–n.

| | | |
|---|---|---|
| (a) | $[] + N_2(g) + 3H_2(g)$ | Reference state: clean catalyst, unreacted $N_2(g)$ and $H_2(g)$ |
| (b) | $[] + N_2(g) \rightleftharpoons [N_2]$ | Adsorption of molecular $N_2$ from gas phase |
| (c) | $[N_2] \rightleftharpoons [N + N]$ | Dissociative adsorption of $N_2$ |
| (d) | $[N + N] + H_2(g) \rightleftharpoons [N + N + H + H]$ | Dissociative adsorption of first $H_2(g)$ |
| (e) | $[N + N + H + H] \rightleftharpoons [N + NH + H]$ | Formation of first -NH intermediate |
| (f) | $[N + NH + H] \rightleftharpoons [N + NH_2]$ | Formation of first -$NH_2$ intermediate |
| (g) | $[N + NH_2] + H_2(g) \rightleftharpoons [N + NH_2 + H + H]$ | Dissociative adsorption of second $H_2(g)$ |
| (h) | $[N + NH_2 + H + H] \rightleftharpoons [N + NH_3 + H]$ | Formation of first $NH_3$ intermediate |
| (i) | $[N + NH_3 + H] \rightleftharpoons [N + H] + NH_3(g)$ | Desorption of first $NH_3$ |
| (j) | $[N + H] \rightleftharpoons [NH]$ | Formation of second -NH intermediate |
| (k) | $[NH] + H_2(g) \rightleftharpoons [NH + H + H]$ | Dissociative adsorption of third $H_2(g)$ |
| (l) | $[NH + H + H] \rightleftharpoons [NH_2 + H]$ | Formation of second -$NH_2$ intermediate |
| (m) | $[NH_2 + H] \rightleftharpoons [NH_3]$ | Adsorption of second $NH_3$ intermediate |
| (n) | $[NH_3] \rightleftharpoons [] + NH_3(g)$ | Desorption of second $NH_3$ |
| (o) | $[] + 2NH_3(g) \rightarrow []$ | Desorption of both $NH_3$ and leaving clean catalyst |

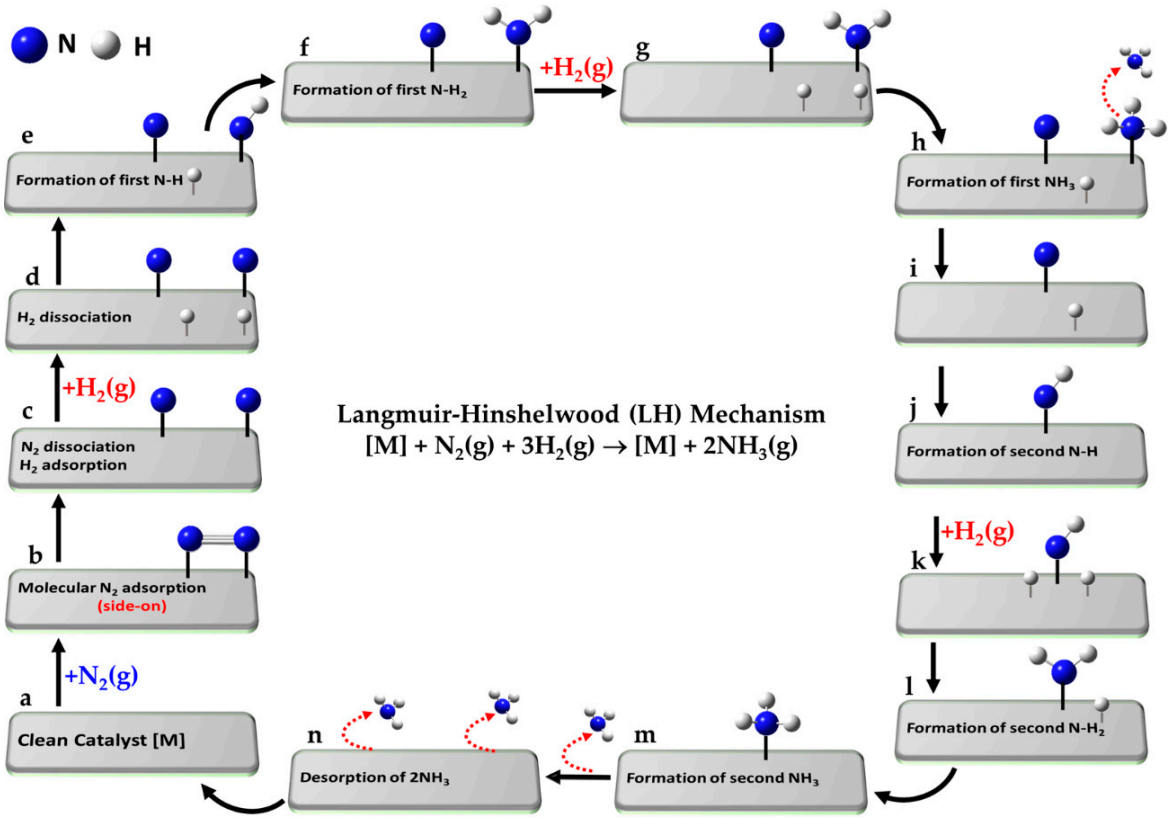



**Figure 5.** (**a**–**n**) Schematic representation of the Langmuir–Hinshelwood (LH) (dissociative) mechanism for ammonia synthesis. The elementary reaction is $[M] + N_2(g) + 3H_2(g) \rightarrow [M] + 2NH_3(g)$, where M in [M] represents the active site on the clean catalyst [] and (g) denotes the gas phase species.

The reference state (a) corresponds to the clean catalyst surface, [M], with active sites M, along with one mole of $N_2$ and three moles of $H_2$ in the gas phase, i.e., [M] + $N_2$(g) + 3$H_2$(g). In step (b), $N_2$ adsorbs from the gas phase onto the surface. Step (c) involves the dissociative adsorption of $N_2$, where the N≡N bond is cleaved to form two surface-bound nitrogen atoms. In step (d), the first $H_2$ molecule undergoes dissociative adsorption, forming two surface-bound H atoms. Subsequent hydrogenation steps lead to the formation of a metal–imide intermediate (M–NH; step e), then a metal–aminyl (M–$NH_2$; step f). Step (g) involves adsorption and dissociation of a second $H_2$ molecule, enabling further hydrogenation to a metal–ammonia species (M–$NH_3$; step h). In passing from step (h) to step (i), the first $NH_3$ molecule desorbs into the gas phase. The second N atom undergoes an analogous sequence: formation of M–NH (step j), followed by dissociative adsorption of a third $H_2$ molecule (step k), leading to M–$NH_2$ (step l) and M–$NH_3$ (step m). The second $NH_3$ molecule desorbs in step (n), and step (o) represents the final state, where both ammonia molecules have desorbed, regenerating the clean catalyst surface [M]. Clearly, each N atom follows a similar sequence of hydrogenation steps, but the exact path may slightly vary depending on the specific intermediate and surface site involved.

Often, the symbol "*" is used to denote an active site on a catalyst surface (in contrast to our use of "[]" to represent the clean catalyst that has the active site M), with reactions written as *2 + $N_2$(g) ⇌ *2N (rather than that of step b, for example) or *2 + $H_2$(g) ⇌ *2H [217]. These expressions imply that the adsorbed molecule dissociates into two atoms, each binding to a separate active site—an assumption valid when the molecule adopts a side-on (horizontal) orientation, allowing simultaneous interaction with two adjacent sites. However, this representation is less accurate for end-on adsorption, where the molecule initially binds through one atom to a single (atop) site on the catalyst (see atop adsorption of $N_2$ in Figure 1d). Nevertheless, after cleavage, the resulting atoms may still occupy two distinct active sites through dissociative adsorption.

Transition metal nitrides, such as $Ta_3N_5$(100) [140,150] and η-$Mn_3N_3$(100) [218], serve as catalysts for elucidating the LH mechanism in ammonia synthesis. The adsorption of $N_2$ at nitrogen vacancies is moderately endothermic, with an energy of 0.199 eV. Strong ammonia adsorption ($E_{ad}$ = 2.332–2.934 eV), comparable to its desorption energy, has been identified as the RDS, indicating that high temperatures are required for effective ammonia synthesis.

Catalysts such as $Co_3Mo_3N$(111) [115] and Mo-terminated δ-MoN(0001) [211] may facilitate ammonia synthesis at elevated temperatures via the LH mechanism. However, for $Co_3Mo_3N$, this pathway is less kinetically favorable due to higher energy barriers in the hydrogenation steps [150].

Ru catalysts supported by electrides, such as as $[Ca_{24}Al_{28}O_{64}]^{4+}(e^-)_4$ and $Ca_2N$:$e^-$, exemplify systems where LH-based rate equations aid in determining reaction kinetics [25].

The associative and dissociative concerted mechanism proposed by Ye et al. [99] for Co/CeN catalysts aligns with the LH model for $N_2$ dissociation, while also highlighting the role of nitrogen vacancies in facilitating the associative process [116]. Similarly, Co or Fe atoms enhance $N_2$ dissociation on the electron-rich surface of molybdenum carbide ($Mo_2C$), forming $N_{ad}$ atoms in accordance with the LH mechanism [57]. It has been suggested that the RDS shifts from nitrogen dissociation to the hydrogenation of surface-bound $NH_x$ species. However, whether the rate-limiting step and the rate-determining step are identical remains unclear, as the former is the slowest step in the sequence, while the latter controls the overall reaction rate. Furthermore, the specific hydrogenation intermediate corresponding to the RDS after this shift was not explicitly identified.

Mo-terminated γ-$Mo_2N$(111) and δ-MoN(0001) catalysts are nearly identical, both exhibiting exothermic adsorption of $N_2$, with adsorption energies ranging from −1.07 to −2.54 eV for δ-MoN(0001) at the PBE functional level of theory [211]. Notably,

the side-on adsorption at the bridge site is favored over other adsorption sites, such as on top or tilted molecule orientation. The authors proposed that the rhombic configuration of the nearest-neighbor Mo sites exists on Mo-terminated γ-$Mo_2N$(111), while near-identical surface site configurations are observed on Mo-terminated δ-MoN(0001). Moreover, the well-established method for controllable growth of single-crystalline, hexagonal MoN thin films provides a foundation for developing effective strategies to sustain Haber–Bosch catalysis by the LH mechanism with these materials.

$N_2$ dissociation on pristine δ-MoN(0001) is associated with an $E_a$ of 0.52 eV, but the reaction is rate-limited by the subsequent hydrogenation step, with an $E_a$ of 2.00 eV for NH + H → $NH_2$. By contrast, the activation energies for the reactions N + H → NH ($E_a$ = 1.42 eV) and $NH_2$ + H → $NH_3$ ($E_a$ = 2.00 eV) are lower. These values are different to those estimated for the corresponding reactions on γ-$Mo_2N$(111), where $E_a$ values are 0.58, 1.18, 1.47, and 1.28 eV, respectively [186,211]. However, in this case, the RDS is associated with the formation of an $NH_2$ intermediate and the desorption of $NH_3$. This contrasts with N-terminated γ-$Mo_2N$, where the RDS is $N_2$ → 2N, and the hydrogenation steps have activation barriers in the range 1.2–1.6 eV, with $NH_3$ desorption having an activation energy of 0.87 eV. It was further shown that a significantly larger activation barrier can be observed for the hydrogenation step on the γ-phase model ($E_a$ = 2.56 eV) for $NH_2$ + H → $NH_2$, particularly when the system's initial state is arbitrary.

Sato et al. [120] proposed that $N_2$ adsorption on Co nanoparticles supported on MgO weakens the N≡N triple bond to the strength of a double bond. This weakening was attributed to electron donation from $Ba^{2+}$ in BaO, mediated through neighboring Co atoms, which facilitates $N_2$ bond cleavage. They proposed the dissociation step ($N_2$ → 2N) as the RDS in ammonia synthesis. However, this conclusion was based on assumptions rather than a thorough examination of reaction mechanisms and adsorption characteristics, analogously as conducted in studies on lanthanoid-oxide-supported Ru [219] and Fe/Ba/MgO [47] catalysts. More recently, Miyazaki et al. [52] challenged this perspective, demonstrating that $N_2$ dissociation—as in Ru-based catalysts [62]—is not the RDS in most catalytic systems, including Fe/$BaTiO_{3-x}N_y$. Instead, the breakdown of scaling relations suggests that catalytic activity is governed by the adsorption of intermediates and transition-state energies on the transition metal surface.

### *5.3. The Associative Langmuir–Rideal and Eley–Rideal Mechanisms*

The Langmuir–Rideal (LR) mechanism [175], an adsorption-abstraction process in heterogeneous atom recombination [220], involves a gas-phase reactant (atom or molecule) directly colliding with an adsorbed species on the catalyst surface, as per condition (ii) (Section 5.2). Under ambient conditions (1 atm), such collisions are rare. However, an atomic gas-phase reactant may form via the hot-atom mechanism if its precursor molecule undergoes multiple rebounds on the surface [221,222]. The key distinction between the LR and LH mechanisms lies in the thermal equilibrium: the gaseous reactant in the LR mechanism is not in thermal equilibrium with an adsorbed species on the catalyst surface [199].

The Eley–Rideal (ER) mechanism [223,224], often referenced in plasma catalysis [159,160], operates in a low-entropy regime for the gas-phase reactant. Unlike the LR mechanism, the ER mechanism entails the gas-phase reactant being weakly adsorbed onto the catalyst surface through van der Waals interactions [225]—essentially a form of physisorption [223]. This weak adsorption mitigates the disorder of the gas-phase species, as compared to the LR mechanism, reducing the entropic factor [188]. The rest of the ER mechanism is driven by collisional interactions between the physisorbed species and the chemisorbed surface species, facilitating the hydrogenation steps. A detailed comparison of the LR and ER mechanisms can be found elsewhere [198,220].

The $N_2$ molecule undergoes chemisorption on the catalyst surface, while the reactant $H_2$ may be physisorbed, particularly when the surface exhibits limited reactivity (inertness) toward its adsorption. In such cases, the surface is ineffective in cleaving the H–H bond [213], or $H_2$ remains in the gas phase when the surface fails to provide the necessary site-specific environment for physisorption. The former occurrence is not uncommon on transition metal surfaces such as Cu, Ag, and Au [215].

The collision between the interacting species dictates whether the LR or ER mechanism governs the formation of $NH_3$ [200,216]. The reaction follows an associative mechanism, where recombination between reactants occurs. Some studies suggest that both the LH and ER mechanisms can contribute collectively to the overall reaction rate [226]. Notably, Elis et al. [227] demonstrated that the ER mechanism dominates at very high temperatures (around 1250 K) for specific catalysts, in contrast to the LH mechanism.

The elementary steps (a–l) representing the Eley–Rideal mechanism for the reaction $N_2(g) + 3H_2(g) \rightleftharpoons 2NH_3(g)$ on the catalyst surface are outlined below.

| | |
|---|---|
| a. $[] + N_2(g) + 3H_2(g)$ | Reference state: clean catalyst; unreacted $N_2(g)$ and $H_2(g)$ |
| b. $[] + N_2(g) \rightleftharpoons [N_2]$ | Chemically adsorbed $N_2$ molecule |
| c. $[N_2] + H_2(g) \rightleftharpoons [N\text{-}N + H_2]$ | Physically adsorbed first $H_2$ molecule |
| d. $[N\text{-}N + H_2] \rightleftharpoons [N\text{-}NH_2]$ | Formation of $N\text{-}NH_2$ intermediate |
| e. $[N\text{-}NH_2] + H_2(g) \rightleftharpoons [N\text{-}NH_2 + H_2]$ | Physically adsorbed second $H_2$ molecule |
| f. $[N\text{-}NH_2 + H_2] \rightleftharpoons [NH\text{-}NH_3]$ | Formation of $NH\text{-}NH_3$ |
| g. $[NH\text{-}NH_3] \rightleftharpoons [NH] + NH_3(g)$ | Desorption of first $NH_3(g)$ |
| h. $[NH] + H_2(g) \rightleftharpoons [NH + H_2]$ | Physisorption of third $H_2$ molecule |
| i. $[NH + H_2] \rightleftharpoons [NH\cdots H_2]$ | Formation of $NH\cdots H_2$ weakly bonded intermediate |
| j. $[NH\cdots H_2] \rightleftharpoons [NH_3]$ | Formation of second $NH_3$ |
| k. $[NH_3] \rightleftharpoons [] + NH_3(g)$ | Desorption of second $NH_3$ |
| l. $[] + 2NH_3(g) \rightleftharpoons []$ | Desorption of two $NH_3$; clean catalyst regenerated |

The elementary steps (a′-l′) of the LR mechanism for the reaction $N_2(g) + 3H_2\ (g) \rightleftharpoons 2NH_3(g)$ on the catalyst surface [] are as follows:

(a′) $[] + N_2(g) + 3H_2(g)$
(b′) $[] + N_2(g) \rightleftharpoons [N_2]$
(c′) $[N_2] + H_2(g) \rightleftharpoons [N\text{-}N\cdots H_2]$
(d′) $[N\text{-}N\cdots H_2] \rightleftharpoons [N\text{-}NH_2]$
(e′) $[N\text{-}NH_2] + H_2(g) \rightleftharpoons [N\text{-}NH_2\cdots H_2]$
(f′) $[N\text{-}NH_2\cdots H_2] \rightleftharpoons [NH\text{-}NH_3]/[NH_2\text{-}NH_2]$ (/ refers another possibility)
(g′) $[NH\text{-}NH_3]/[NH_2\text{-}NH_2] + H_2(g) \rightleftharpoons [NH\text{-}NH_3\cdots H_2]/[NH_2\text{-}NH_2\cdots H_2]$
(h′) $[NH\text{-}NH_3\cdots H_2]/[NH_2\text{-}NH_2\cdots H_2] \rightleftharpoons [NH_3\cdots NH_3]$
(i′) $[NH_3\cdots NH_3] \rightleftharpoons [NH_3] + [NH_3]$
(j′) $[NH_3] + [NH_3] \rightleftharpoons [NH_3] + NH_3(g)$
(k′) $[NH_3] + NH_3(g) \rightleftharpoons [] + NH_3(g)$
(l′) $[] + 2NH_3(g) \rightarrow []$

The key aspects of the minimum-energy pathway following the LR and ER mechanisms are illustrated in Figure 6. Both mechanisms can operate when $N_2$ adopts an end-on (or indeed side-on) orientation [150]. While not explicitly shown for both, the end-on mode (left, a–k) is depicted for the ER mechanism, and the side-on (right, a′–k′) for the LR mechanism.

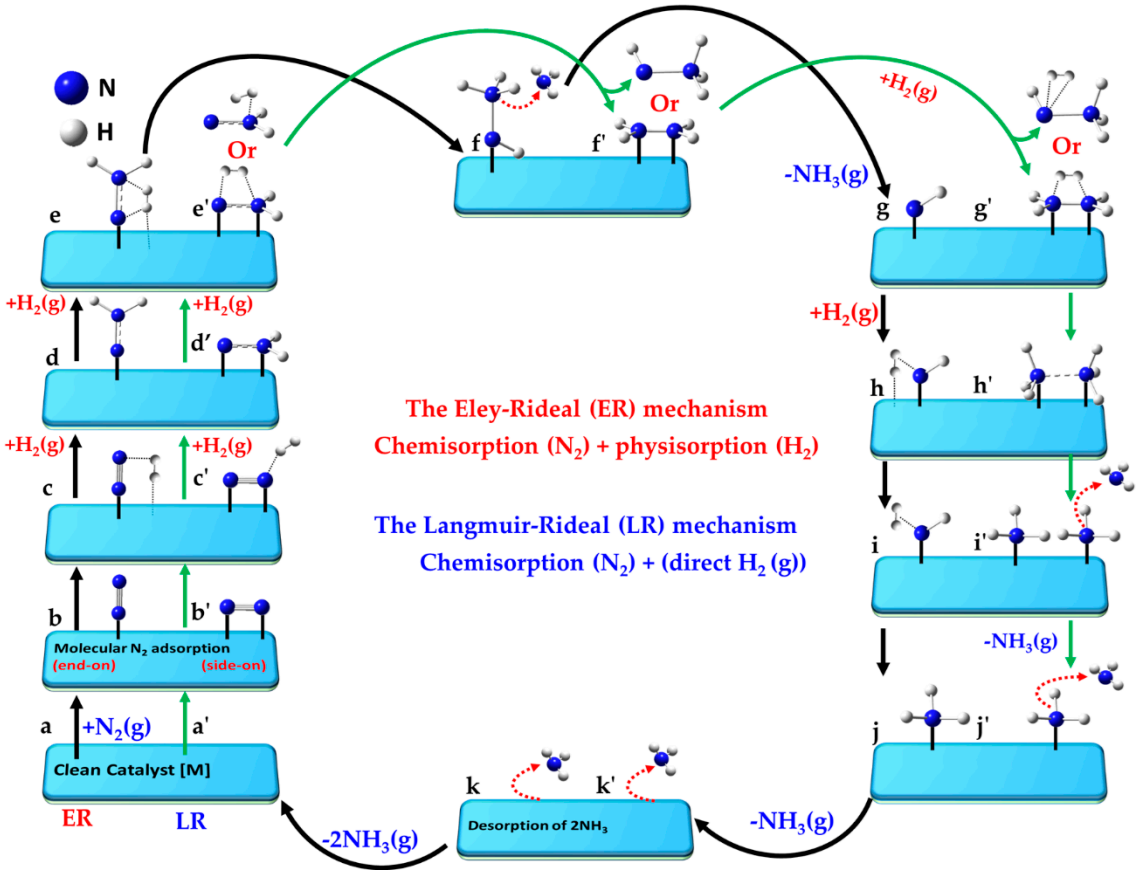



**Figure 6.** Schematic representation of the (**a**–**k**) (associative) Eley–Rideal (ER) (**left**) and (**a′**–**k′**) Langmuir–Rideal (LR) (**right**) mechanisms for ammonia synthesis. The elementary reaction, [M] + $N_2$(g) + 3$H_2$(g) → [M] + 2$NH_3$(g), is shown, where M in [M] represents the active site on the clean catalyst []. Two possible adsorption modes of molecular $N_2$ on the catalyst are depicted, facilitating direct chemical reactions between chemisorbed $N_2$ and physisorbed (or gas-phase) $H_2$ molecules via a non-dissociative mechanism, leading to the formation of intermediate and product species along the ER and LR pathways, respectively. In both cases, the $N_2$ molecule may be adsorbed in either an end-on or side-on orientation. Interaction modes between the reactants are illustrated in (**f′**,**g′**), each showing the varied nature of plausible intermediate species.

For the ER mechanism, the process begins with a clean catalyst [M] (a), which facilitates the chemisorption of $N_2$ in step (b). The first $H_2$ molecule is physisorbed onto the same catalyst and non-covalently interacts with the distal N atom of chemisorbed $N_2$ in step (c), forming a hydrazine intermediate (N-$NH_2$) in step (d). A second $H_2$ molecule is adsorbed in a similar manner in step (e), and reacts to form the NH–$NH_3$ species (see step f). The first $NH_3$ molecule desorbs when passing from (f) to (g), leaving the NH intermediate in step (g). A third $H_2$ molecule is physisorbed in step (h), forming a $H_2$···NH intermediate (i). The second $NH_3$ molecule desorbs in step (k), and step (l) represents the final state in which both ammonia molecules have desorbed, fully regenerating the clean catalyst surface [M] as shown in (a).

For the LR mechanism, when the $N_2$ molecule is adsorbed in its side-on orientation (b′), the first $H_2$ molecule interacts directly with one of the N atoms via non-covalent interactions (c′). Alternatively, if $N_2$ adopts an end-on adsorption geometry (as in step b), the distal nitrogen atom is the primary site of interaction with the incoming $H_2$ molecule. A hydrazine (N=$NH_2$) intermediate (d′) is formed regardless of the adsorption mode. A second $H_2$ molecule adsorbs (e′), progressing to an intermediate (f′). Two possible interaction modes are shown in steps e′–g′, leading to $NH_2$-$NH_2$ or NH-$NH_3$ intermediates

(f′). The N-N bond may break at this stage, or if it remains intact, a third $H_2$ molecule interacts with the intermediate, advancing from (f′) to (g′). This leads to stage (h′), where two $NH_3$ species are non-bonded to each other. Stage (i′) follows, where the $NH_3$ species are physically separated, either via chemisorption or physisorption. The first $NH_3$ molecule desorbs from stage (i′) to (j′), and the second $NH_3$ molecule desorbs from (j′) to (k′). Step (l′) represents the final stage, where both $NH_3$ molecules have desorbed, regenerating [M]. While the pathway is hypothetical, the actual state of the intermediate species may vary depending on the nature of the catalyst surface.

Lan et al. [145] investigated the LH and ER mechanisms on an Fe(111) surface, identifying $NH_2 + H \rightarrow NH_3$ as the rate-determining step. Their DFT calculations revealed that the top shallow site on Fe(111) is the most energetically favorable position for $NH_2$. For the ER mechanism, they simulated the migration of a surface-activated H atom, placing it in a vacuum approximately 4.6 Å above the Fe surface. As the H atom approached the surface, it descended and reacted with the adsorbed $NH_2$, thereby forming $NH_3$.

While the authors attributed surface-adsorbed H migration to the LH mechanism and vacuum-phase H migration to the ER mechanism, the latter process, in our view, aligns more closely with the LR mechanism. However, the study does not explicitly confirm whether the H atom first adsorbs onto the Fe surface before reacting with $NH_2$. Temporary interaction or weak adsorption before reaction is common in the ER mechanism. Despite this ambiguity, the study concluded that the ER and LH mechanisms share close similarities, with the key distinction being the vertical position of the H atom: in the ER mechanism (more accurately, the LR mechanism), the H atom descends toward $NH_2$, whereas in the LH mechanism, it remains elevated as $NH_3$ forms.

It was argued that the θ-$Mn_6N_5$-(111) catalyst facilitates an ER mechanism, but its kinetics are unfavorable due to the high barrier for surface nitrogen hydrogenation [150]. The nitrogen vacancies on the catalyst surface play a crucial role in driving the reaction, favoring an associative pathway [218]. Rouwenhorst et al. [228] proposed a similar ER mechanism involving comparable intermediate steps. However, in their model, association occurs through direct interaction between dissociatively adsorbed hydrogen atoms and N radicals from the plasma on MgO-supported Ru, Co, Pt, Pd, Cu, and Ag catalysts. In this process, the reaction $N + H \rightarrow NH$ on the catalyst surface was identified as the rate-limiting step. Since the N radicals originate from the plasma and are not physically adsorbed, this mechanism, in our view, aligns more closely with the LR mechanism rather than the ER mechanism.

$N_2$ adsorbs more strongly than $H_2$ on $Mn_6N_{5+x}$ ($x$ = 1)-(111) catalysts [229]. When adsorbed in an end-on configuration, $N_2$ exhibits minimal activation. Hydrogenation via the ER mechanism faces high energy barriers (>1.866 eV or 182 kJ $mol^{-1}$), making ammonia synthesis impractical on this catalyst unless elevated temperatures are applied. A similar conclusion was drawn for the η-$Mn_3N_2$-(100) catalyst, where $N_2$ adopts a side-on configuration in both the ER and LH mechanisms [215].

Zhang et al. [230] demonstrated that Ru clusters on MgO exhibit significantly stronger $N_2$ adsorption ($E_{ad}$ = −1.95 eV) compared to Ru/$SiO_2$ ($E_{ad}$ = −0.75 eV) and Ru/$Al_2O_3$ ($E_{ad}$ = −1.33 eV). $N_2$ dissociation on Ru/MgO has a low barrier (1.07 eV) and is exothermic by 0.33 eV. However, the high activation energy for hydrogenating surface-adsorbed N and $NH_x$ species hinders $NH_3$ formation via the LH mechanism, particularly in the $NH_2 + H \rightarrow NH_3$ step, leading to a lower production rate. Instead, $NH_3$ production via the ER mechanism was suggested in a plasma environment, involving reactions such as $H_2$(g) + NH or H(g) + $NH_2$, with the hot-atom mechanism assumed to aid $N_2$ dissociation. However, the process corroborates more accurately with the LR mechanism rather than the ER mechanism.

### *5.4. The Associative Mars–Van Krevelen (MvK) Mechanism*

The Mars–van Krevelen mechanism [148] involves a redox process in which the catalyst surface undergoes oxidation and reduction cycles during ammonia synthesis. In this process, the first $NH_3$ molecule is desorbed via hydrogenation of metal-coordinated N sites as in the backbone of the catalyst and a nitrogen vacancy is created through the reduction of mono-, bi- or tertiary- metal nitrides MN (e.g., TiN, CeN, $Mo_2N$ and $Co_3Mo_3N$) [104]. Introducing surface nitrogen vacancies, which are replenished by the direct capture of externally supplied gaseous $N_2$, facilitates its subsequent activation. The associative distal-type pathway (vide infra) becomes the primary mechanism, where the distal N atom in $N_2$ undergoes hydrogenation before the dissociation of the N≡N triple bond [42]. This leads to the formation and desorption of the second $NH_3$ molecule, leaving behind the clean metal nitride catalyst [231], as observed for A–Mn–N (A = Li, K, Fe or Co) materials [232].

The elementary reaction pathway corresponding to the MvK mechanism, progresses through the following steps (a–n), where "•" refers to the vacancy site that represents the active absorption site on the clean catalyst [].

| | |
|---|---|
| a. $[\bullet] + N_2(g) + 3H_2(g)$ | Reference: clean catalyst with vacancy, unreacted $N_2$ (g) and $H_2$(g) |
| b. $[\bullet] + N_2(g) \rightleftharpoons [N_2]$ | Molecular adsorption of $N_2$(g) at the vacancy |
| c. $[N_2] + H_2(g) \rightleftharpoons [N_2 + H_2]$ | Molecular adsorption of $H_2$ |
| d. $[N_2 + H\cdots H] \rightleftharpoons [N\text{-}NH + H]$ | Dissociation of $H_2$, formation of N−NH intermediate |
| e. $[N\text{-}NH + H] \rightleftharpoons [N\text{-}NH_2]$ | Formation of N-$NH_2$ intermediate |
| f. $[N\text{-}NH_2] + H_2(g) \rightleftharpoons [N\text{-}NH_2 + H_2]$ | Molecular adsorption of second $H_2$ |
| g. $[N\text{-}NH_2 + H\cdots H] \rightleftharpoons [N\text{-}NH_3 + H]$ | Dissociation of $H_2$ and formation of first $NH_3$ |
| h. $[N\text{-}NH_3 + H] \rightleftharpoons [N\ H] + NH_3(g)$ | Desorption of first $NH_3$(g) |
| i. $[N\ H] \rightleftharpoons [NH]$ | Formation of second NH intermediate |
| j. $[NH] + H_2(g) \rightleftharpoons [NH + H_2]$ | Molecular adsorption of third $H_2$ |
| k. $[NH + H\cdots H] \rightleftharpoons [NH_2 + H]$ | Dissociation of $H_2$ and formation of $NH_2$ |
| l. $[NH_2 + H] \rightleftharpoons [NH_3]$ | Formation of second $NH_3$ |
| m. $[NH_3] \rightleftharpoons [\bullet] + NH_3$ (g) | Desorption of second $NH_3$(g) |
| n. $[\bullet] + 2NH_3(g) \rightleftharpoons [\bullet]$ | Desorption of two $NH_3$, leaving clean catalyst |

A schematic view of the entire reaction pathway for the MvK mechanism is shown in Figure 7a–m, following a consecutive pathway for protonation [162]; the term "consecutive" refers to the step-by-step hydrogenation of the same nitrogen atom in $N_2$. The reference state (a) consists of the clean catalyst surface with an oxygen vacancy, unreacted $N_2$(g), and three $H_2$(g) molecules. The reaction pathway proceeds via a surface with a vacancy or defect (b), where $N_2$ initially adsorbs—typically in an end-on, tilted, or side-on configuration (the first two depicted in b)—at the active site [206,233]. This is followed by $H_2$ adsorption (c), in line with the mechanistic description reported by Jesudass et al. [231].

The dissociation of $H_2$ begins to occur at this stage, with one hydrogen atom transferring to the distal nitrogen atom in $N_2$, leading to the formation of the N-NH intermediate (d). At this point, $N_2$ may remain in its original end-on titled configuration (as on the left) or shift to a side-on orientation (as on the right). Continued hydrogenation results in the formation of the N-$NH_2$ intermediate (e).

The addition of a second $H_2$ molecule leads to the configurations depicted in step (f). The reaction pathway continues with the formation of a diazane intermediate in step (g), which facilitates the desorption of the first $NH_3$ molecule as the system transitions from step (g) to (h). The subsequent steps (h–l) proceed in a manner analogous to the associative part of the LH mechanism [233,234] (see Figure 5i–m), involving the sequential formation

of NH, $NH_2$, and $NH_3$ intermediates. This culminates in the desorption of the second $NH_3$ molecule in step (m) of Figure 7, restoring the clean catalyst with the vacancy to complete the catalytic cycle (step n.).

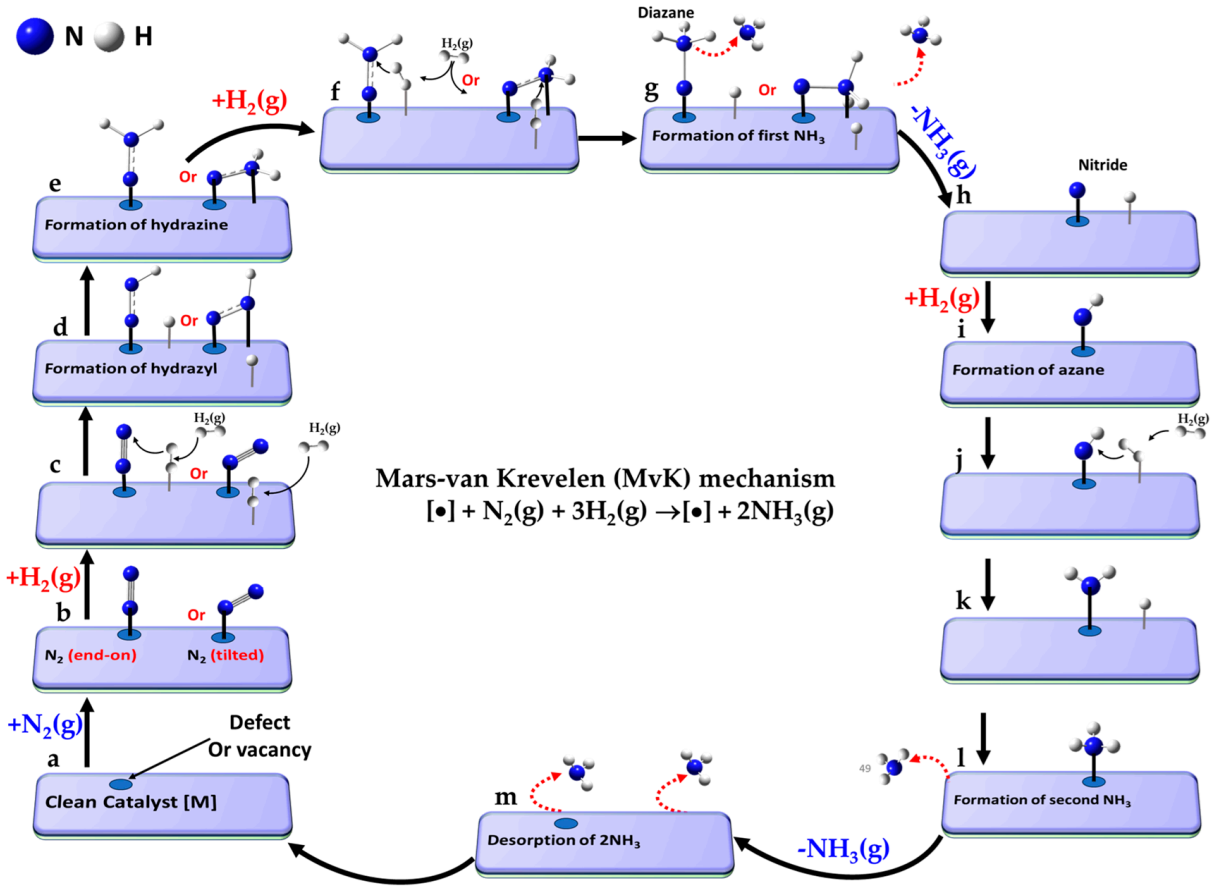



**Figure 7.** (**a**–**m**) Schematic representation of the associative Mars–van Krevelen (MvK) mechanism for ammonia synthesis, following a (distal-type) consecutive pathway for hydrogenation. The elementary reaction is as follows: [•] + $N_2$(g) + 3$H_2$(g) → [•] + 2$NH_3$(g), where [•] represents the vacancy site on the clean catalyst. Two possible modes of adsorption of $N_2$ are shown: (**left**) end-on; (**right**) (side-on tilted).

It should be noted that the dissociation of the N≡N bond can occur at any point between steps (d) and (g), depending on the reactivity of the transition metal catalyst, although this is not explicitly depicted in the schematic. While this study primarily focuses on the use of molecular $N_2$ and $H_2$, other studies (e.g., (viz. ref. [147]) explore the stepwise hydrogenation of a single H atom to the distal nitrogen site in $N_2$ on specific metal mononitride catalysts (such as rocksalt(100)) for $N_2$ electroreduction and ammonia pair formation.

An ER-MvK hybrid mechanism has been proposed for ammonia synthesis on catalysts like molybdenum nitride ($Co_3Mo_3N$) [159], iron-molybdenum nitride ($Fe_3Mo_3N$) [143,150], and other transition metal nitride catalysts [196], combining elementary steps from both the ER and MvK mechanisms. In this model, $N_2$ adsorbs onto the catalyst in a side-on [143] or end-on orientation [101,115,229], where the distal N site first interacts with gaseous $H_2$ directly [235], forming an -N-$NH_2$ intermediate on the $Fe_3Mo_3N$ catalyst (similar to that shown in Figure 7d (right)). In another study [115], the same authors demonstrated that the first $H_2$ molecule directly interacts with the distal N atom of end-on adsorbed $N_2$, forming a trans-hydrazine intermediate on the $Co_3Mo_3N$(111) catalyst, and the subsequent steps follow the MvK pathway, as shown in Figure 7f–m. Even though it's called the ER-MvK

mechanism for $Fe_3Mo_3N$ [143] and $Co_3Mo_3N$ [115] catalysts, it results from a combination of the LR and MvK mechanism, and could be referred to as an LR-MvK mechanism instead.

The elementary pathway associated with the LR-MvK mechanism may proceed through steps (a–m, below). Most steps follow the typical ER-MvK mechanism, except for step c ($[N_2] + H_2(g) \rightleftharpoons [N\text{-}NH_2]$) that involves direct interaction between adsorbed $N_2$ and gaseous $H_2$. The remaining two $H_2$ molecules are initially physisorbed on the surface, rather than immediately reacting with the chemisorbed $N_2$.

| | |
|---|---|
| a. $[\bullet] + N_2(g) + 3H_2(g)$ | Reference state: clean catalyst with a vacancy, unreacted $N_2(g)$ and $H_2(g)$ |
| b. $[\bullet] + N_2(g) \rightleftharpoons [N_2]$ | Molecular adsorption of $N_2(g)$ at the vacancy |
| c. $[N_2] + H_2(g) \rightleftharpoons [N\text{-}NH_2]$ | LR step: first $H_2$ interacts directly with distal N in $N_2$, forming $N\text{-}NH_2$ |
| d. $[N\text{-}NH_2] + H_2(g) \rightleftharpoons [N\text{-}NH_2 + H_2]$ | Adsorption of second $H_2$ molecule |
| e. $[N\text{-}NH_2 + H_2] \rightleftharpoons [N\text{-}NH_3 + H]$ | Formation of $N\text{-}NH_3$ intermediate |
| f. $[N_2H_3 + H] \rightleftharpoons [N + NH_3 + H]$ | Formation of first $NH_3$ |
| g. $[N + NH_3 + H] \rightleftharpoons [N\ H] + NH_3\ (g)$ | Desorption of first $NH_3(g)$ |
| h. $[N + H] \rightleftharpoons [NH]$ | Formation of first NH intermediate |
| i. $[NH] + H_2(g) \rightleftharpoons [NH + H_2]$ | Adsorption of third $H_2$ molecule |
| j. $[NH + H_2] \rightleftharpoons [NH_2 + H]$ | Formation of $NH_2$ intermediate |
| k. $[NH_2 + H] \rightleftharpoons [NH_3]$ | Formation of second $NH_3$ |
| l. $[NH_3] \rightleftharpoons [\bullet] + NH_3\ (g)$ | Desorption of second $NH_3(g)$ |
| m. $[\bullet] + 2NH_3(g) \rightleftharpoons [\bullet]$ | Desorption of two $NH_3$ molecules, leaving behind the clean catalyst |

Roy and Kumar [57] suggested that both the LH and MvK mechanisms can coexist on $Mo_2C$, $Fe/Mo_2C$, and $Co/Mo_2C$ thermo-catalysts, each contributing to ammonia synthesis. However, the $Co/Mo_2C$ catalyst exhibited the higher performance, attributed to its strong electron-donating ability, which enhances nitrogen dissociation For instance, at 520 °C and 1 bar, the specific activities for $Mo_2C$, $Fe/Mo_2C$, and $Co/Mo_2C$ were reported to be 8.58, 9.78, and 11.73 μmol $h^{-1}$ $m^{-2}$, respectively.

Kitano et al. [109] found that $BaCeO_{3-x}N_yH_y$ acts as an efficient thermo-catalyst operating through the MvK mechanism, with lattice $N^{3-}$ and $H^-$ ions mediating the process. However, ammonia synthesis typically occurs over conventional catalysts via the LH mechanism, highlighting the combined role of the MvK-LH model. Zhang et al.'s review [236] provides a detailed account of this mechanism on catalysts, such as $Ru/LaN/ZrH_2$ [237].

Due to the high activation barrier for $N_2$ dissociation and the endothermic adsorption of $N_2$ on clean transition metal nitride surfaces, the MvK mechanism is a more favorable electrocatalytic NRR pathway [147,238]. Abghoui et al. [147,239] identified VN, CrN, ZrN, and NbN as the most promising catalysts, with the rocksalt (100) facet exhibiting the highest activity. These materials, due to their stable N vacancies and resistance to poisoning by −H or −O, demonstrated superior NRR activity compared to HER. Guan et al. [240] also highlighted the significance of the MvK mechanism in various vacancy-assisted catalysts.

Kobayashi et al. [103] demonstrated that at an elevated temperature of 400 °C, solid-state hydride-containing titanium compounds—specifically $TiH_2$ and $BaTiO_{2.5}H_{0.5}$—give rise to a nitride-hydride surface strikingly similar to that observed in titanium clusters. Under the influence of $H_2/N_2$ flow conditions, these compounds undergo a continuous transformation, producing $NH_3$ over an extended period of approximately 7 days, sustaining a catalytic cycle with an impressive activity of up to 2.8 mmol·$g^{-1}$·$h^{-1}$. Although the reaction mechanism was not explicitly detailed, it was speculated that the MvK mechanism might be involved, as the $N_2$ dissociation step occurred rapidly and was not the RDS.

Wang et al.'s [241] discovery identifies early 5f-element catalysts, particularly the surfaces of $ThO_2$ and $UO_2$ (111), as exceptional and highly efficient single-component catalysts for the conversion of $N_2$ to $NH_3$. Their pioneering study highlights atomic oxygen vacancies as the central and crucial active sites for $NH_3$ synthesis from $N_2$ and $H_2$ gases. Their analysis shows that the chemically adsorbed N≡N molecule is highly resistant to direct dissociation, with significant energy barriers of 3.64 eV and 2.91 eV on $ThO_2$ and $UO_2$ surfaces, respectively. This suggests that $NH_3$ synthesis is unlikely to proceed via the dissociative LH mechanism.

While $N_2$ binds to the vacancy site on these catalysts, $H_2$ dissociates directly at the same location, producing two $H^-$ ions. These $H^-$ ions then migrate across the surface, enabling the hydrogenation of the distal N site on adsorbed $N_2$, which ultimately leads to the formation of N=NH and N=$NH_2$ intermediates. The N-N bond cleavage occurs through the reaction N-$NH_2$ + H → NH + $NH_2$, although this reaction step does not precisely mirror the step from Figure 7g to Figure 7h in which the latter involves the formation of an N-$NH_3$ intermediate. The subsequent steps (depicted in Figure 7i–m) for the generation of the second $NH_3$ molecule, however, proceed identically. The most energetically favorable and computed reaction pathway is as follows: $N_2$(g) → [N≡N] → [N=NH] → [N-$NH_2$] → [HN···$NH_2$] → [HN···$NH_3$] → [NH] → [$NH_2$] → [$NH_3$] → 2$NH_3$(g). The process may follow an associative MvK mechanism.

The nickel-loaded lanthanum nitride (Ni/LaN) catalyst exemplifies the MvK mechanism [53]. The rate-limiting step is the fusion of hydrogen with the nitrogen lattice (N + H → NH), with an energy barrier of ~0.54 eV, closely matching the Arrhenius plot value (~0.622 eV). Further hydrogenation selectively targets the top nitrogen of adsorbed N≡N at the vacancy site, initiating a stepwise progression toward the formation of a second $NH_3$. This sequence, culminating in the release of $NH_3$, is governed by an overall energy barrier of 0.76 eV.

The account by Tian et al. [242] provides additional details on other catalysts, e.g., Ru/CaFH, $BaH_2$–BaO/Fe, Ba–Co@NC, (Co, Fe)/$BaCeO_{3-x}N_yH_z$ $ATiO_{3-x}H_x$ (A = Ba, Sr, Ca) and Ru-loaded $BaTiO_{2.5}H_{0.5}$ [243], where the MvK mechanism is at play.

### 5.5. Associative Alternating (Symmetric) Pathway (AAP)

The associative alternating (symmetric) pathway (AAP) [201] involves the adsorption of $H_2$ on the catalyst's surface, its dissociation, and the alternating hydrogenation of adsorbed $N_2$. $N_2$ binds end-on orientation to the catalyst, which weakens the N≡N bond. Dissociatively adsorbed hydrogen atoms are then progressively transferred to $N_2$ through an alternating hydrogenation process, ultimately producing $NH_3$.

The steps of the AAP mechanism are illustrated in Figure 8a–m. Starting from the reference state (a), the mechanism includes the clean catalyst (a), non-dissociatively adsorbed $N_2$ (b), and dissociatively adsorbed $H_2$ (c, f, and i). The surface reaction between H and the distal N atom in $N_2$ forms intermediate hydrogenated species N=NH (d). Sequential addition of H atoms to the N atoms alternately, in a symmetric fashion, leads to the formation of NH-NH (e), NH-$NH_2$ (g), $N_2H_2$ (h), and $NH_2NH_2$ (j). The cleavage of the N-N bond occurs during the hydrogenation stages (i → j), followed by the desorption of the first $NH_3$ at stage (j → k), leaving an amine group (-$NH_2$) at stage (k). Further hydrogenation leads to the formation of the second $NH_3$ (l), followed by its desorption from (l) to (m).

The elementary steps, a-n, of the AAP mechanism are depicted in Figure 8a–m. The process begins from the reference state (a), which includes the clean catalyst surface, a molecule of $N_2$, and three molecules of $H_2$, represented as [] + $N_2$(g) + 3$H_2$(g). In step (b), $N_2$ adsorbs non-dissociatively onto the surface, typically in an end-on configuration. This is followed by the dissociative adsorption of the first $H_2$ molecule in step (c), providing two

surface-bound hydrogen atoms. One hydrogen then reacts with the distal nitrogen of $N_2$ to form the N–NH intermediate (d). Subsequently, symmetric addition of hydrogen atoms leads to the formation of NH–NH (e), followed by the dissociative adsorption of the second $H_2$ molecule in step (f), enabling further hydrogenation to produce NH–$NH_2$ (g) and then $NH_2$–$NH_2$ (h). The third $H_2$ molecule dissociates in step (i), leading to the formation of the $NH_2$···$NH_3$ intermediate in step (j). The cleavage of the N–N bond and the desorption of the first $NH_3$ molecule occur during the transition from step (j) to (k), leaving behind an –$NH_2$ group. Continued hydrogenation results in the formation of the second $NH_3$ molecule in step (l), which desorbs in step (m). Final desorption of both $NH_3$ molecules is completed in step (n), thereby regenerating the clean catalyst surface and closing the catalytic cycle.

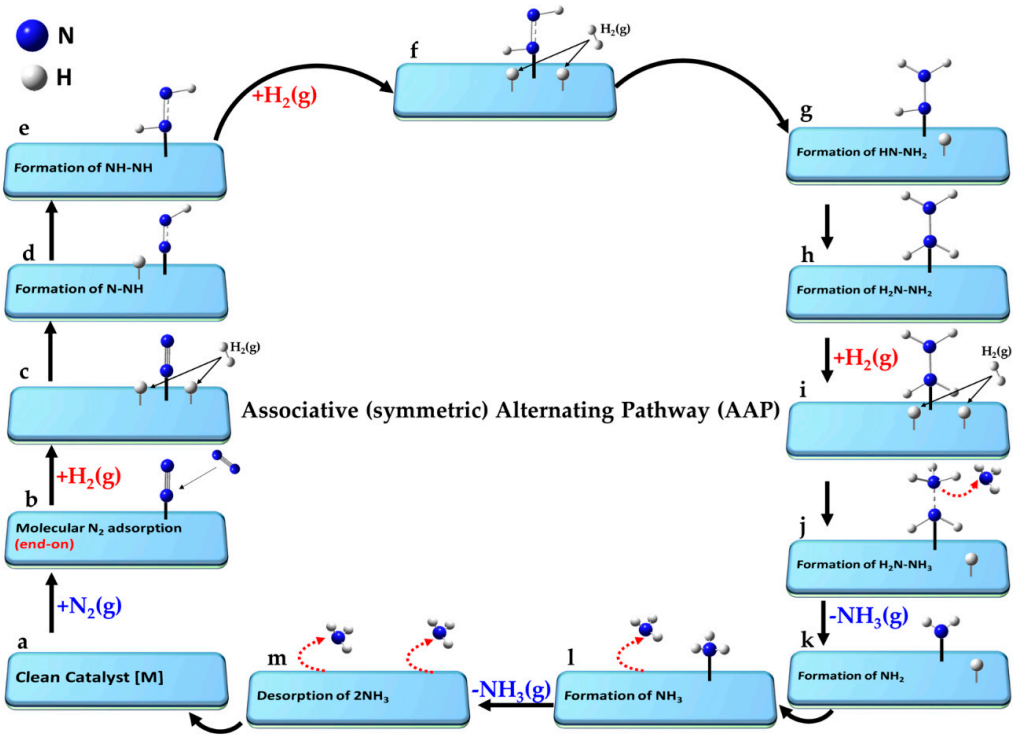



**Figure 8.** (**a**–**m**) Schematic representation of the associative alternating (symmetric) pathway for ammonia synthesis. The elementary reaction is as follows: [M] + $N_2$(g) + 3$H_2$(g) → [M] + 2$NH_3$(g), where M in [M] represents the active site on the clean catalyst [] (e.g., $Ca_3CrN_3H$ [108]).

In the vacancy-assisted AAP mechanism, schematically represented in the study by Yet al. [203], the first $H_2$ directly hydrogenates end-on adsorbed $N_2$ in an alternating fashion, forming NH=NH via the LR mechanism. The next $H_2$ dissociates on the catalyst surface, with one hydrogen atom adsorbing while the other hydrogenates NH=NH, yielding the NH-$NH_2$ intermediate. Further hydrogenation produces $NH_2$-$NH_2$, and the third $H_2$ follows a similar pattern, leading to the release of the first $NH_2$. Subsequent hydrogenation releases a second $NH_2$ molecule. This reaction mechanism closely resembles that shown in Figure 8, differing only in how $H_2$ participates in the hydrogenation process.

A recent study on the catalyst $Ca_3CrN_3H$(001) [108] examined the AAP mechanism, demonstrating that the free energy pathway for $N_2$ hydrogenation follows the alternating route. $N_2$ activation and hydrogenation primarily occur at Ca cations rather than Cr sites. The $N_2$ + H → N=NH step is the most energy-intensive, requiring 0.63 eV when hydrogen is supplied from lattice H. The process becomes even less favorable with gaseous $H_2$, raising the energy cost to 0.85 eV. Further hydrogenation proceeds either through direct gaseous $H_2$ attack on the N moiety or by filling a surface H vacancy, followed by lattice H

attack. Preferential hydrogenation occurs at the surface-bound N rather than the distal N, making the alternating associative pathway approximately 0.5 eV more favorable. Partial cleavage of NH=NH and NH-$NH_2$ bonds may occur during the process, while $NH_2$-$NH_2$ bond dissociation is believed to happen spontaneously. Upon further hydrogenation, $NH_2$ forms as an intermediate, and final hydrogenation leads to the exothermic release of $NH_2$ (−1.55 eV).

| | |
|---|---|
| a. [] + $N_2$(g) + 3$H_2$(g) | Reference state: clean catalyst and unreacted $N_2$ and $H_2$ |
| b. [] + $N_2$(g) ⇌ [$N_2$] | Molecular end-on adsorption of $N_2$(g) |
| c. [$N_2$] + $H_2$(g) ⇌ [N-N + H H] | Dissociative adsorption of first $H_2$ molecule |
| d. [N-N + H H] ⇌ [N-NH + H] | Formation of N-NH intermediate |
| e. [N-NH + H] ⇌ [NH-NH] | Formation of NH-NH intermediate |
| f. [NH-NH] + $H_2$(g) ⇌ [NH-NH + H H] | Dissociative adsorption of second $H_2$ molecule |
| g. [NH-NH + H H] ⇌ [NH-$NH_2$ + H] | Formation of NH-$NH_2$ intermediate |
| h. [NH-$NH_2$ + H] ⇌ [$NH_2$-$NH_2$] | Formation of $NH_2$-$NH_2$ intermediate |
| i. [$NH_2$-$NH_2$] + $H_2$(g) ⇌ [$NH_2$-$NH_2$ + H H] | Dissociative adsorption of third $H_2$ molecule |
| j. [$NH_2$-$NH_2$ + H H] ⇌ [$NH_2$-$NH_3$ + H] | Formation of $NH_2$···$NH_3$ intermediate |
| k. [$NH_2$-$NH_3$ + H] ⇌ [$NH_2$ + H] + $NH_3$(g) | Formation of $NH_2$ and desorption of first $NH_3$ |
| l. [$NH_2$ + H] + $NH_3$(g) ⇌ [$NH_3$] | Adsorption of second $NH_3$(g) |
| m. [$NH_3$] ⇌ [] + $NH_3$(g) | Desorption of second $NH_3$(g) |
| n. [] + 2$NH_3$ ⇌ [] | Desorption of two $NH_3$ molecules, leaving behind the clean catalyst |

Li et al. [244] reported an $FeN_3$-embedded graphene single-atom catalyst (SAC) using DFT modeling, demonstrating that the $FeN_3$ active site significantly facilitates N≡N bond cleavage, making both distal and alternating pathways of the associative mechanism highly favorable. Similarly, Liu et al. [156] proposed that $Fe_3$ clusters anchored on θ-$Al_2O_3$($Fe_3$/θ-$Al_2O_3$(010)) exhibit an extraordinary turnover frequency, outperforming Fe's $C_7$ sites by two orders of magnitude. This remarkable enhancement is attributed to the unparalleled ability of $Fe_3$ clusters to catalyze $N_2$ activation via the AAP mechanism, where adsorbed $N_2$ first hydrogenates to form an N=NH intermediate. This pathway is more efficient than the dissociative mechanism involving direct $N_2$ cleavage.

### *5.6. Associative (Asymmetric) Distal Pathway (ADP)*

The associative (asymmetric) distal pathway (ADP) [68,245,246] involves the hydrogenation of molecularly adsorbed $N_2$ on transition metal surfaces, where the terminal nitrogen atom plays the first involved in facilitating the reaction. In this process, hydrogen molecules first dissociate on the catalyst surface, releasing activated (surface-bound) hydrogen atoms that are transferred to $N_2$.

The catalytic reduction of nitrogen via the distal pathway proceeds through a sequential hydrogenation mechanism, as illustrated in Figure 9a–m. The process begins with the clean catalyst surface exposed to gaseous nitrogen and hydrogen (a). $N_2$ adsorbs molecularly in an end-on configuration onto the active site (b), followed by dissociative adsorption of the first $H_2$ molecule, leading to surface-bound hydrogen atoms (c). These hydrogen atoms facilitate the stepwise hydrogenation of the distal nitrogen atom, producing N–NH and then N–$NH_2$ intermediates (d–e). A second $H_2$ molecule adsorbs and dissociates (f), allowing further hydrogenation to form N–$NH_3$ (g). At this stage, the first $NH_3$ molecule is released, leaving behind the [N H] intermediate on the surface (h). This remaining nitrogen atom undergoes additional hydrogenation, leaving behind the N-H intermediate (i). The third $H_2$ molecule dissociates (j), and subsequent steps convert the N–H species to $NH_2$ and then to $NH_3$ (k–l). The second ammonia molecule is then desorbed from the surface (m),

regenerating the catalyst and completing the cycle with the release of both $NH_3$ molecules (see step n).

| | | |
|---|---|---|
| (a) | [] + $N_2$(g) + 3$H_2$(g) | Reference state: clean catalyst, unreacted $N_2$ and $H_2$ |
| (b) | [] + $N_2$(g) ⇌ [$N_2$] | Molecular end-on adsorption of $N_2$(g) |
| (c) | [$N_2$] + $H_2$(g) ⇌ [N-N + H H] | Dissociative adsorption of first $H_2$ molecule |
| (d) | [N-N + H H] ⇌ [N-NH + H] | Formation of N-NH intermediate |
| (e) | [N-NH + H] ⇌ [N-$NH_2$] | Formation of N-$NH_2$ intermediate |
| (f) | [N-$NH_2$] + $H_2$(g) ⇌ [N-$NH_2$ + H H] | Dissociative adsorption of second $H_2$ molecule |
| (g) | [N-$NH_2$ + H] ⇌ [N-$NH_3$ + H] | Formation of N-$NH_3$ intermediate |
| (h) | [N-$NH_3$ + H] ⇌ [N H] + $NH_3$(g) | Formation of $NH_2$-$NH_2$ and desorption of first $NH_3$ |
| (i) | [N-H] ⇌ [N-H] | Formation of NH intermediate |
| (j) | [N-H] + $H_2$(g) ⇌ [N-H + H H] | Dissociative adsorption of third $H_2$ molecule |
| (k) | [N-H + H H] ⇌ [$NH_2$ + H] | Formation of second $NH_2$ |
| (l) | [$NH_2$ + H] ⇌ [$NH_3$] | Adsorption of second $NH_3$(g) |
| (m) | [$NH_3$] ⇌ [] + $NH_3$(g) | Desorption of second $NH_3$(g) |
| (n) | [] + 2$NH_3$(g) ⇌ [] | Desorption of both $NH_3$ molecules |

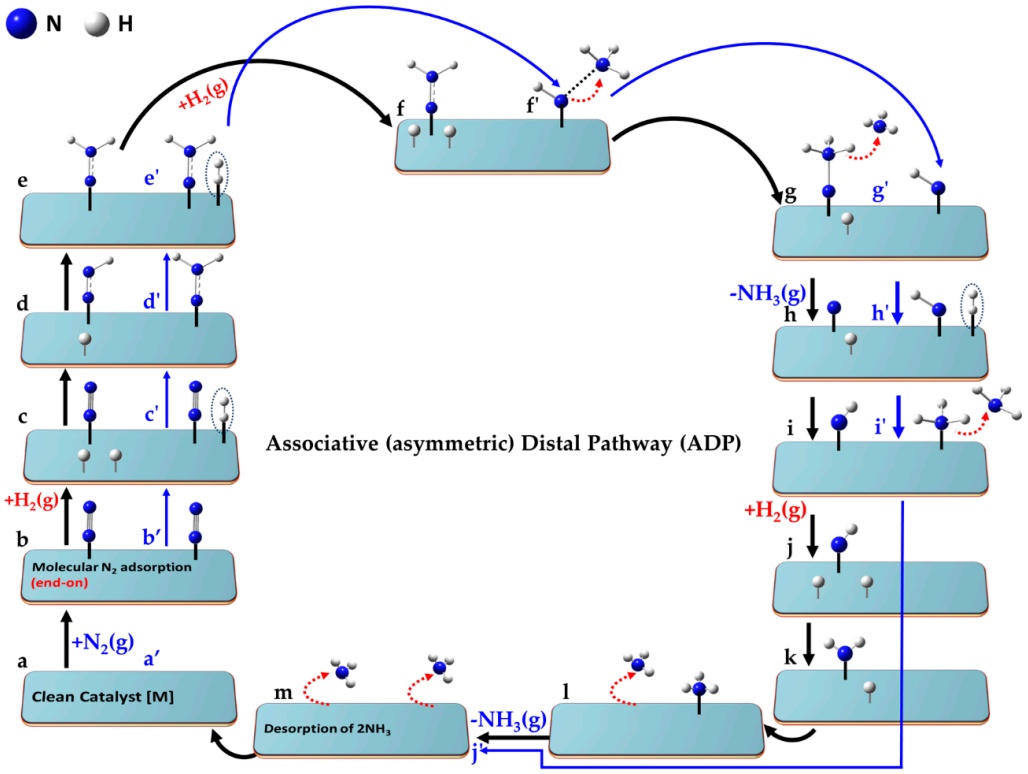



**Figure 9.** (**a**–**m**) Schematic representation of the associative (asymmetric) distal pathway (ADP) mechanism for ammonia synthesis. The elementary reaction is as follows: [M] + $N_2$(g) + 3$H_2$(g) → [M] + 2$NH_3$(g), where M in [M] represents the active site in the clean catalyst [] and (g) denotes the gas phase species. Shown in (**a′**–**j′**) is the distal pathway similar to that utilized in the study of

Qui et al. [107], including the following reactant, intermediate and product steps: (**a′**) [M] + $N_2$(g) + 3$H_2$(g); (**b′**) [M-$N_2$] + 3$H_2$(g); (**c′**) [M-$N_2$ $H_2$] + 2$H_2$(g); (**d′**) [M-N-$NH_2$] + 2$H_2$(g); (**e′**) [M-N-$NH_2$ $H_2$] + $H_2$(g); (**f′**) [M-NH···$NH_3$] + $H_2$(g); (**g′**) [M-NH] + $NH_3$(g) + $H_2$(g); (**h′**) [M-NH $H_2$] + $NH_3$(g); (**i′**) [M-$NH_3$] + $NH_3$(g); (**j′**) [M] + 2$NH_3$(g). In each step of the reaction, (**a′**–**j′**), the total number of hydrogen and nitrogen moieties is conserved, although this stoichiometric balance is not explicitly depicted in the schematic.

Catalysts like $Ca_3CrN_3H(001)$ [108] effectively promote the distal pathway by forming lattice hydrides and weakly adsorbing $H_2$, which helps prevent hydrogen poisoning. The catalyst's adsorption sites are approximately 3 Å apart—an ideal distance for hydrogenation. However, stable dissociative adsorption of $N_2$ requires a separation of about 7.20 Å, corresponding to the spacing between equivalent $Ca_3$ active sites. This configuration forces the bottom nitrogen atom deeper into the $Ca_3$ cavity toward Cr, resulting in high-energy adsorption states. Consequently, dissociative $N_2$ adsorption at these sites demands extensive surface diffusion, making this pathway both spatially and energetically unfavorable.

While less thermodynamically favorable than the alternating pathway, the ADP pathway may still occur on the catalyst, especially when $N_2$ is strongly adsorbed or when catalyst properties—such as steric and electronic factors—favor distal hydrogenation. After the release of the first $NH_3$ molecule, it was suggested that the remaining nitrogen at a Cr site in $Ca_3CrN_3H$ undergoes hydrogenation to form NH and $NH_2$, which weakens the $Cr^{-}N$ coordination and leads to the formation of $NH_3$. The ammonia desorption process is endothermic by approximately 1 eV.

The study of Liu et al. [68] identified an associative distal mechanism within a ferrierite catalyst with dual Mo(II) sites, [L-2$Mo^{(II)}$/FER], which promotes efficient ammonia synthesis under ambient conditions. With a significantly lower energy barrier for $N_2$ hydrogenation (0.73 eV) compared to direct N≡N bond breaking (1.38 eV), the catalyst outperforms Ru in turnover frequency over a wide temperature range, highlighting the potential of tailored porous catalysts with multiple active sites for the Haber–Bosch process.

The pure siliceous zeolite-supported Ru SAC (Ru SAs/S-1) catalyst is another exemplary system [107] that facilitates the ADP mechanism. DFT calculations indicate that $H_2$ weakly adsorbs on Ru sites or lattice oxygen sites within the zeolite framework. Notably, $H_2$ molecules remain largely intact within the zeolite channels, where they are physically adsorbed with a weak interaction energy of 0.21 eV. By contrast, $N_2$ preferentially adsorbs linearly on Ru with a stronger binding energy of 0.57 eV.

The reaction step $N_2 + H_2 \rightarrow N\text{-}NH_2$ (the first hydrogenation step), distinct from that shown in Figure 9d, was proposed as the rate-determining step, with an activation energy of 0.88 eV. This is reasonable because the subsequent reaction steps, $N\text{-}NH_2 + H_2 \rightarrow NH + NH_3\uparrow$, $NH + H_2 \rightarrow NH_3\uparrow$, have lower activation energies, facilitating their faster progression. Depicted in Figure 9a′–j′ is the distal pathway, similar to that used in the study by Qui et al. [107]. It includes the following reaction steps: (a′) [M]; (b′) [M-$N_2$] + 3$H_2$(g); (c′) [M-$N_2$ $H_2$] + 2$H_2$(g); (d′) [M-N-$NH_2$] + 2$H_2$(g); (e′) [M-N-$NH_2$ $H_2$] + $H_2$(g); (f′) [M-NH···$NH_3$] + $H_2$(g); (g′) [M-NH] + $NH_3$(g) + $H_2$(g); (h′) [M-NH $H_2$] + $NH_3$(g); (i′) [M-$NH_3$] + $NH_3$(g); (j′) [M] + 2$NH_3$(g). In each step of the reaction, Figure 9a′–j′, the total number of hydrogen and nitrogen moieties is conserved, although this stoichiometric balance is not explicitly depicted in the schematic. In this case, the physically adsorbed $H_2$ molecule directly reacts with the adsorbed nitrogen species to form $NH_3$, which then desorbs. The reaction pathway is more consistent with an ER-type ADP mechanism.

Wang et al. [247] have designed homogeneous single-atom Ru centers on an H-ZMS-5 (HZ) support, with Ru atoms individually anchored in the micropores of HZ. Their DFT calculations revealed that the direct dissociation of $N_2$ into two nitrogen atoms on a single Ru site of the Ru/HZ SAC catalyst requires a substantial energy barrier of 2.90 eV. However, the hydrogenation process via the ADP mechanism, leading to the formation of $N^{-}NH_2$, demands a significantly lower activation energy of just 1.12 eV. The hydrogenation of $N_2$ was crucial for the significant weakening of the N≡N bond, with the RDS proposed to be associated with forming the $N_2H_2$ intermediate.

Ghuman et al. [248] suggested that using an associative mechanism, $N_2H$ ($N_2 + H \rightarrow N_2H$) serves as the RDS for both Ru/MgO and RuFe/MgO catalysts. However, while this

pathway applies to the former catalyst, it could shift to $N_2H_2 + H \rightarrow N_2H_3$ in the latter case, as this transition involves higher energy. For the dissociative mechanism, a significant energy barrier was observed for the reaction $NH_2 + H \rightarrow NH_3$ on both catalysts, but the associative pathway was found favorable over the dissociative one.

Bai and colleagues [117] proposed that the rate-determining step in their associative pathway is $N_2 + H \rightarrow N + NH$ on the $Ru/CeO_2$ catalyst. They demonstrated $N_2H$ as the precursor of the N≡N bond cleavage. However, the lack of a detailed reaction pathway in their study makes it difficult to discern whether a distal path or an alternating one was followed prior to the dissociation of the kinetically relevant vertically adsorbed N=NH intermediate, in contrast to the widely known dissociative route [5,249,250]. According to the schematic model presented by the authors, the $N_2$ molecule initially aligns in an end-on orientation on the clean catalyst. Upon protonation of the distal nitrogen, the molecule shifts to a side-on orientation before the N=NH bond undergoes cleavage. The subsequent hydrogenation of the adsorbed NH and N species results in the formation of $NH_3$.

### *5.7. The Associative Enzymatic Reaction Pathway (AERP)*

In the associative enzymatic reaction pathway (AERP), employed by nitrogenase enzymes in biological systems, $N_2$ is converted to $NH_3$ through stepwise hydrogenation, and the catalytic site is subsequently regenerated. This mechanism, which avoids the high-energy nitrogen dissociation step, is increasingly used as a model for photocatalytic and electrocatalytic NRR [251].

A recent mechanism proposed by Hau et al. [252] resembles AERP in its alternating hydrogenation pattern and is similar to the associative alternating pathway (AAP, see Figure 8). This "bridge distal pathway" (BDA) involves side-on ($\mu$-$\eta^2$:$\eta^2$) adsorption of $N_2$, followed by sequential hydrogenation and eventual release of two $NH_3$ molecules. The "bridge" term refers to this specific binding mode, distinguishing BDA from AAP where $N_2$ is not necessarily bridge-bound. However, it remains uncertain whether the hydrogen atoms involved in reduction are sourced from the catalyst surface or the gas phase. In a consecutive-type pathway [162], three hydrogen atoms attack one nitrogen atom in pre-adsorbed $N_2$, leading to the stepwise release of $NH_3$, as proposed by Hou et al. [252].

Figure 10 illustrates the sequential steps of AERP, where two ammonia molecules are synthesized from a single $N_2$ molecule. Similar to BDA but unlike AAP, $N_2$ adopts a side-on orientation, enhancing hydrogenation efficiency. The orientation of $N_2$ influences its accessibility and reactivity, with the side-on configuration in AERP creating a more favorable environment for N≡N bond cleavage. Ultimately, the preferred reaction pathway depends on the catalyst's surface morphology and electron density, both of which govern $N_2$ activation and reactivity.

The sequential steps of AERP are outlined below (steps a–m). Since the intermediate steps of hydrogenation mirror those of the AAP with the end-on orientation of $N_2$ (Figure 8), a detailed reiteration of each step is unnecessary.

Peng et al. investigated Ru-Co dual single-atom catalysts (RuCo DSAC) for ammonia synthesis via AERP [253]. They identified that the first hydrogenation of $N_2$, forming $N_2H$ ($N_2 + H \rightarrow N_2H$) on the Ru site, had the highest kinetic barrier, making it the rate-limiting step. Their findings are noteworthy, showing that the $NH_3$ synthesis rate of RuCo DSAC was 8.2 times and 7.5 times higher than that of Co SAC and Ru SAC, respectively, at 400 °C. A combination of experimental data and DFT calculations revealed that the synergistic interaction between Ru and Co centers significantly enhanced $NH_3$ synthesis via the associative pathway.

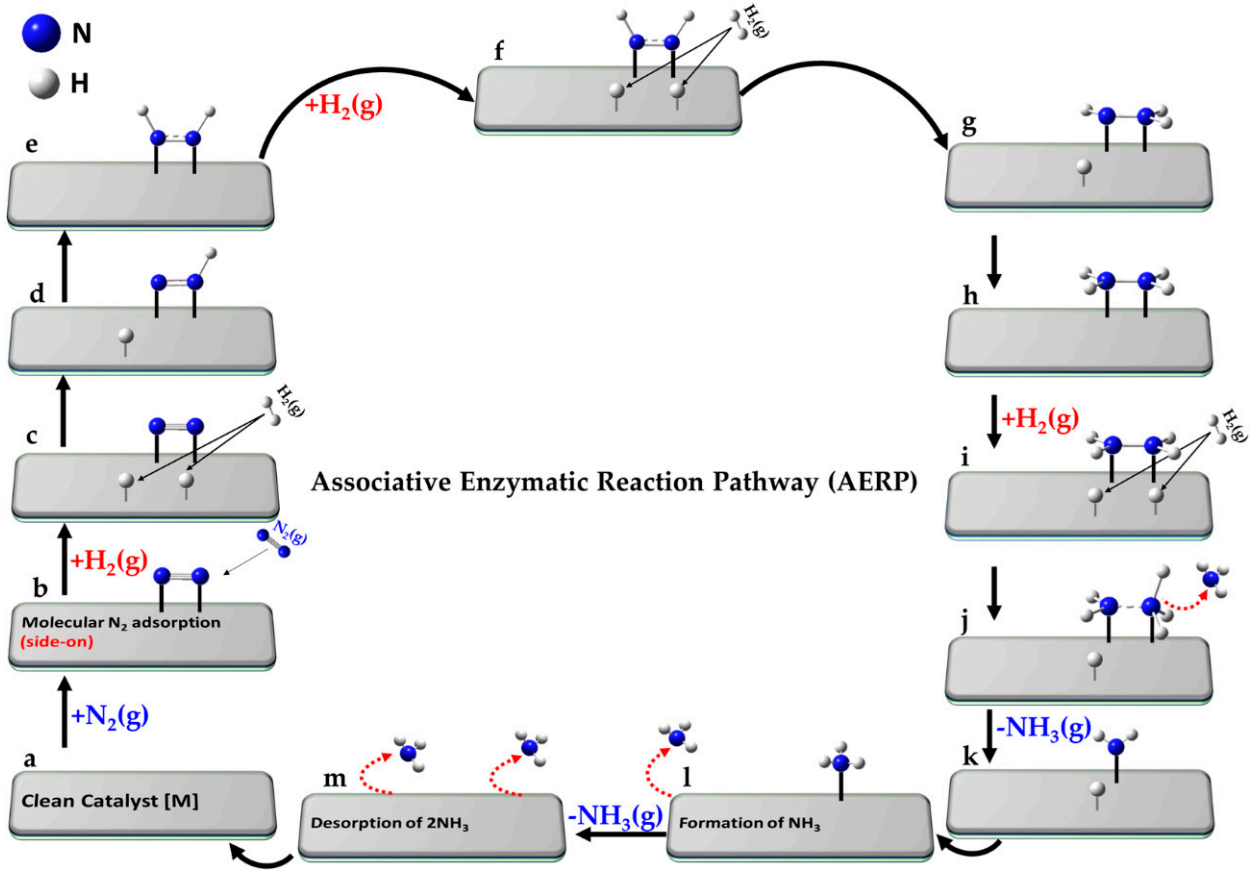



**Figure 10.** (**a**–**m**) Schematic representation of the enzymatic reaction pathway (AERP) for ammonia synthesis. The elementary reaction is as follows: [M] + $N_2$(g) + 3$H_2$(g) → [M] + 2$NH_3$(g), where [M] represents the clean catalyst and (g) denotes the gas phase species.

| | | |
|---|---|---|
| a. | [] + $N_2$(g) + 3$H_2$(g) | Reference state: clean catalyst unreacted $N_2$ and $H_2$ |
| b. | [] + $N_2$(g) ⇌ [$N_2$] | Molecular side-on adsorption of $N_2$(g) |
| c. | [$N_2$] + $H_2$(g) ⇌ [N-N + H H] | Dissociative adsorption of first $H_2$ molecule |
| d. | [N-N + H H] ⇌ [N-NH + H] | Formation of N-NH intermediate |
| e. | [N-NH + H] ⇌ [NH-NH] | Formation of NH-NH intermediate |
| f. | [NH-NH] + $H_2$(g) ⇌ [NH-NH + H H] | Dissociative adsorption of second $H_2$ molecule |
| g. | [NH-NH + H H] ⇌ [NH-$NH_2$ + H] | Formation of NH-$NH_2$ intermediate |
| h. | [NH-$NH_2$ + H] ⇌ [$NH_2$-$NH_2$] | Formation of $NH_2$-$NH_2$ intermediate |
| i. | [$NH_2$-$NH_2$] + $H_2$(g) ⇌ [$NH_2$-$NH_2$ + H H] | Dissociative adsorption of third $H_2$ molecule |
| j. | [$NH_2$-$NH_2$ + H H] ⇌ [$NH_2$-$NH_3$ + H] | Formation of $NH_2$···$NH_3$ intermediate |
| k. | [$NH_2$-$NH_3$ + H] ⇌ [$NH_2$ + H] + $NH_3$(g) | Formation of $NH_2$ and desorption of first $NH_3$ |
| l. | [$NH_2$ + H] + $NH_3$(g) ⇌ [$NH_3$] | Adsorption of second $NH_3$(g) |
| m. | [$NH_3$] ⇌ [] + $NH_3$(g) | Desorption of second $NH_3$(g) |
| n. | [] + 2$NH_3$ ⇌ [] | Desorption of two $NH_3$, leaving the clean catalyst |

Similarly, theoretical investigations of the singly dispersed bimetallic catalyst $Rh_1Co_3$/CoO(011) [192] demonstrated alternating hydrogenation of $N_2$, with $H_2$ activation occurring on both metal sites. Other studies have explored different catalytic systems, such as $Pt_2$@$C_3N_3$ and $Ru_3$@$C_3N_3$, focusing on the AERP mechanism, as discussed by others [254,255].

Zhang et al. [113] examined Ru clusters on $Sm_2O_3$ (Ru/$Sm_2O_3$) and found that both dissociative and associative pathways contribute to ammonia synthesis. They proposed

two models for side-on adsorbed $N_2$: Model I (hydrogen-lean) and Model II (hydrogen-rich surface). In both models, $N_2$ adsorption was endothermic ($E_{ad}$ = 0.29 eV for Model I, 0.25 eV for Model II), while dissociative adsorption was exothermic ($E_{ad}$ = −0.34 eV for Model I, −0.42 eV for Model II). Protonation proceeded via an associative pathway, but it did not follow enzymatic, distal, or alternating mechanisms, ultimately yielding two $NH_3$ molecules.

In Model I, the reaction followed this sequence:

$N_2 \rightarrow 2N \rightarrow 2N + 2H \rightarrow NH + N + H \rightarrow NH + NH \rightarrow NH + NH + 2H \rightarrow NH_2 + NH + H \rightarrow NH_2 + NH + 2H \rightarrow NH_3 + NH + H \rightarrow NH + H \rightarrow NH_2 + H \rightarrow NH_3(g)$. For the associative pathway, the process remained endothermic until the breakdown of the N=N-H intermediate: $N_2 \rightarrow N_2 + H_2 \rightarrow$ N=N-H + H → N + NH + H. They found that the dissociation of N=NH into N and NH ad-species was both kinetically and thermodynamically favorable under the reaction conditions. The subsequent steps followed a similar pattern to the associative portion of the pathway.

### *5.8. Mechanism of Nitrogenase-Catalyzed Ammonia Synthesis and Associative Analogues*

While this overview focuses primarily on the Haber–Bosch process, it should be appreciated that nitrogen fixation occurs through three main pathways: (i) natural phenomena such as lightning, (ii) biological conversion by nitrogenase enzymes found in specific microorganisms, and (iii) industrial synthesis via the Haber–Bosch process [256].

Below, we briefly outline the widely accepted mechanism by which nitrogenase catalyzes ammonia synthesis. In the AERP, hydrogen atoms typically originate from molecular hydrogen ($H_2$) present in the medium. By contrast, enzymatic systems may also supply protons ($H^+$) or hydride ions ($H^-$), interacting with water molecules through protonation or deprotonation steps, as commonly observed in acid–base catalysis. While AERP represents a biologically inspired mechanism, related pathways such as the distal and alternating mechanisms are also known to be relevant under various catalytic conditions [256,257].

Nitrogenase operates under ambient conditions by coupling electron transfer with ATP hydrolysis [256,258], where ATP refers adenosine triphosphate. The enzyme's active site binds $N_2$ in a suitable orientation for multi-step reduction while receiving electrons from a reductase partner. These enzymes enable plants to assimilate nitrogen, making it accessible throughout the food chain. Nitrogenases are primarily found in bacteria and archaea, such as *Rhizobium* in legumes and *Azotobacter* in soils.

Three types of nitrogenases are known: molybdenum-dependent (Mo-Nase), vanadium-dependent (V-Nase), and iron-only (Fe-Nase) [259]. Each enzyme contains a complex metallocluster: the [$Fe_8S_7$] P-cluster, which serves as an electron relay, and the active-site cofactor, [$MFe_7S_9C$] (where M = Mo, V, or Fe), where $N_2$ reduction takes place [260]. Electrons required for the reaction are donated by a reductase protein (NifH) containing a [$Fe_4S_4$] active site. This reductase is itself reduced by ferredoxin or flavodoxin.

The nitrogenase-catalyzed reaction is energetically demanding due to the high N≡N bond dissociation enthalpy of 941.4 kJ $mol^{-1}$ [44]. Breaking this bond electrochemically would require an overpotential of approximately −1.6 V—well beyond the limits of the nature's "electrochemical window", i.e., in an aqueous environment at pH 7 this is limited by the evolution of $O_2$ (+0.82 V) at one end and the evolution of $H_2$ (−0.41 V) at the other end. Nitrogenase overcomes this challenge by coupling electron transfer to ATP hydrolysis, allowing the reaction to proceed under mild conditions. The mechanism of nitrogenase is complex (see [261] and references therein); what is generally accepted has been summarized recently [262] but many questions remain [263], and involves multiple electron transfer steps.

The nitrogenase cycle requires eight electrons and protons, and its stoichiometry is given by Equation (2), where ADP and Pi refer adenosine diphosphate and inorganic phosphates, respectively.

$$N_2 + 8e^- + 10H^+ + 16ATP \rightarrow 2\,NH_4^+ + H_2 + 16ADP + 16P_i \quad (2)$$

This equation emphasizes several crucial features of the nitrogenase mechanism, such as the role of ATP hydrolysis in facilitating substrate reduction and the mandatory production of 1 mole of $H_2$ for every mole of $N_2$ reduced. This byproduct of hydrogen is essentially a waste of two reducing equivalents and four ATP molecules for each molecule of $N_2$ reduced.

Electrons are delivered by dinitrogenase reductase (NifH), which contains a [$Fe_4S_4$] cluster and is itself reduced by a ferredoxin or flavodoxin. Upon ATP binding, NifH forms a complex with the catalytic component, enabling electron transfer from the [$Fe_4S_4$] site to the P-cluster, and ultimately to the active FeMo cofactor. ATP hydrolysis plays a key role, providing the thermodynamic driving force for the reaction by lowering the redox potential needed for electron transfer, effectively bypassing nature's electrochemical constraints (see [260,264] and references therein). The complex dissociates after each electron transfer, with phosphate release constituting the rate-limiting step. The entire process proceeds through eight one-electron transfer steps, designated $E_0$ to $E_7$, as outlined in the Lowe–Thorneley model [265] (Figure 11). The first $NH_3$ molecule is released after the third hydrogenation, and the second after the fifth, with the release of $H_2$ occurring at various stages. The exact pathway can follow either a distal or alternating mechanism, depending on the sequence of hydrogenation steps and the intermediates formed.

Nitrogen binding to the cofactor typically occurs after the accumulation of three to four electrons, often accompanied by the release of $H_2$. $N_2$ is then progressively reduced via a diazene-type intermediate to form two $NH_3$ molecules. However, the mechanism is not fully resolved. Unproductive $H_2$ loss from $E_2$(2H), $E_3$(3H), or $E_4$(4H) states can reverse progress by two electrons per event, adding complexity to the overall cycle.

The electrons transferred to the FeMo cofactor may reduce the metal centers or form bridging hydrides [266–269]. If hydride species are present, they are expected to emerge after two-electron accumulation steps, while odd-numbered E-states may feature reduced metal centers. Upon $H_2$ release, the cofactor reaches a highly reduced state, enabling effective $N_2$ activation and subsequent conversion to ammonia.

While the initial steps of nitrogen fixation up to the formation of the Janus $E_4$ intermediate are relatively well established, the exact sequence of events in the latter half of the mechanism remains an open question [256,270,271]. Two primary pathways have been proposed: the distal and alternating mechanisms. In the distal pathway, hydrogenation is directed first toward the nitrogen atom furthest from the metal center, which is fully reduced and released as ammonia before the proximal nitrogen is hydrogenated. By contrast, the alternating pathway involves a sequential, back-and-forth addition of hydrogen atoms to both nitrogen atoms—alternating between the distal and proximal sites—until both are converted to ammonia.

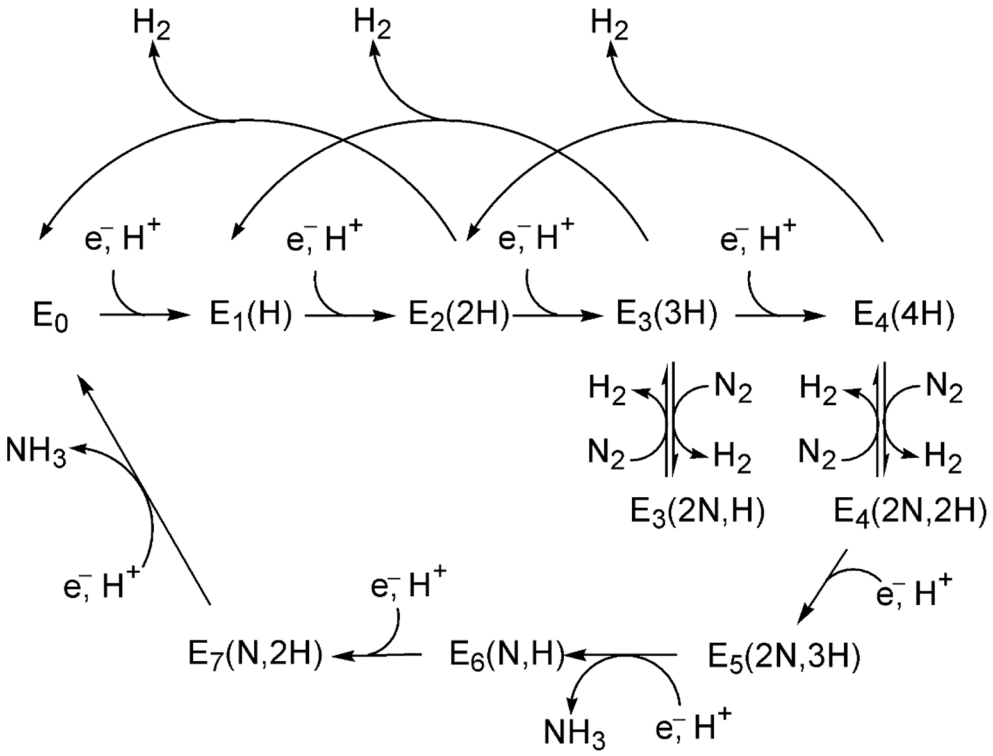



**Figure 11.** The Lowe–Thorneley mechanism of nitrogenase (adapted from [262,263,272]), emphasizing the coupled transfer of electrons and protons across eight steps. While the complete model indicates that $N_2$ binds at either the E3 or E4 stages, this representation focuses less on the pathway through E3. Additionally, the model includes protons that are associated with the FeMo cofactor.

## 6. Reaction Order and the Rate-Determining Step

The reaction order is a key and informative metric reflecting the RDS in a catalytic process [24,75,102,106]. It provides critical insight into the reaction mechanism [118]. The reaction orders for $N_2$, $H_2$, and $NH_3$ may be represented by $\alpha$, $\beta$, and $\gamma$ [114]. The ammonia synthesis rate under the Haber–Bosch process's commercial conditions, as Temkin and Pyzhev proposed in 1940 [32,273], is related to $\alpha$. Across all catalysts, the reaction exhibits nearly first-order kinetics with respect to $N_2$ and close to zero order in $H_2$ and $NH_3$ [116,274]. However, the reaction order with respect to $H_2$ varies depending on the chosen promoter [77], as evidenced by the changes in reaction order observed for $H_2$ passing over unpromoted, Cs-promoted, and Ba-Cs-promoted Ru catalysts. Others have shown that the introduction of Ba and La promoters effectively reduces the $H_2$-induced inhibition observed in Cs-promoted Ru/MgO catalysts [274].

The signs of $\alpha$, $\beta$, and $\gamma$, whether positive or negative, reveal the nature of the molecular interactions with the catalyst surface. A positive reaction order sometimes suggests weak adsorption, meaning the molecule's physical coverage on the catalyst surface is minimal, while a negative order indicates strong adsorption [70], which may obstruct the adsorption of other species. For instance, the negative $\beta$ values of $-0.14$, $-0.18$, and $-0.76$ were reported for $H_2$ on Ru/MgO, Ru/$CeO_2$_500red, and $Cs^+$/Ru/MgO_500red, respectively, implying strong adsorption of hydrogen on the Ru surface, which impedes the efficient activation of molecular $N_2$ [114]. This phenomenon, known as hydrogen poisoning, limits the preferential activity of Ru-based catalysts [76,275], such as Ru/MgO and Cs-Ru/MgO [27,116,274].

By contrast, the positive reaction orders of 0.50, 0.43, 0.32 1.5, 1.2, and 0.8 were reported for $H_2$ on RuFe/MgO [248], Co/Ba/$La_2O_3$_700red, Co/$La_2O_3$_700red [114], $BaH_2$-BaO/Fe/$CaH_2$ [122], Co-Ba/C, and $Co_3Mo_3N$ [118], respectively. The $\beta$ values range from

0.1 to 1.7 for catalysts like Fe/SrNH, Co/SrNH, Ni/SrNH, and Ni/CaNH [116], meaning that these catalysts are not subject to hydrogen poisoning and demonstrate an increased ammonia synthesis rate [116,276].

$\gamma$ is typically negative with respect to $NH_3$. A highly negative $\gamma$ may indicate that an increased concentration of ammonia on the catalyst slows down the reaction rate, in accordance with le Chatelier's principle. The catalyst Co/$La_2O_3$_700red showed a $\gamma$ of $-0.51$, pointing to the inhibitory effect of adsorbed NH, $NH_2$, and $NH_3$ species, which prevents the $NH_3$ yield from reaching equilibrium [114]. However, adding Ba to Co/$La_2O_3$_700red reduced this negative value to $-0.17$, indicating that Ba promotes the desorption of the adsorbate, accelerating the reaction even as it approaches equilibrium.

Fe-based catalysts (e.g., Fe/K(3)/MgO-500red and Fe/MgO-500red) exhibit significantly larger negative $\gamma$ values compared to Ru-based catalysts ($Cs^+$/Ru/MgO-500red and Ru/$CeO_2$-500red) [70]. This behavior is attributed to the strong adsorption of $NH_x$ species on the Fe surface, where the equilibrium between $NH_x$ and $NH_3$ inhibits $N_2$ adsorption and activation. Drummond et al. [77] observed that $\gamma$ for the doubly promoted Ru catalyst could shift from $-0.17$ to $-0.59$ with a 40 °C increase, indicating greater sensitivity of the reaction rate to ammonia concentration at higher temperatures. This shift suggests the possibility of back reactions, site blocking, or a change in catalyst behavior not observed in unpromoted or Cs-promoted Ru catalysts.

In conventional heterogeneous catalysis, the $\alpha$ value for $N_2$ typically hovers near unity (0.8–1.0) [118]. Specific examples include Co NPs ($\alpha$ = 1.08) [277], Ru/MgO ($\alpha$ = 1.4), RuFe/MgO ($\alpha$ = 0.97) [248], Fe/K(3)/MgO-500red ($\alpha$ = 1.0), Ru/$CeO_2$-500red ($\alpha$ = 0.85) [70], $Cs^+$/Ru/MgO-500red ($\alpha$ = 1.07), Ru/$CeO_2$-500red ($\alpha$ = 0.85), Co/Ba/$La_2O_3$-700red ($\alpha$ = 0.85), Co/$La_2O_3$-700red ($\alpha$ = 0.97) [114], commercial Fe ($\alpha$ = 0.90) [27], Ru-Cs/MgO ($\alpha$ = 0.99) [121], and Ru/$[Ca_{24}Al_{28}O_{64}]^{4+}(O_2^-)_2$ ($\alpha$ = 0.75–1.0) [75]. This near-unity order suggests that the RDS in the slow reaction process is the dissociation of molecular $N_2$ [56,70,277].

In electride-based catalysts, however, $N_2$ dissociation is no longer the RDS [24,75,102]. Electrically conductive electrides efficiently donate electrons to the metal surface (e.g., Ru nanoparticles), enhancing $N_2$ cleavage and accelerating the synthesis of $NH_3$. As a result, hydrogenation becomes the rate-limiting step, reducing $\alpha$ for $N_2$ from 0.5 to ~1.5 and lowering the apparent activation energy to 0.45–0.65 eV, thereby improving the efficiency of ammonia synthesis. Such reaction orders were reported for Ca-based systems such as Ru/$Ca(NH_2)_2$ ($\alpha$ = 0.53), Ru/$Ca_2N$:$e^-$ ($\alpha$ = 0.53), Ru/$C_{12}A_7$:$e^-$ ($\alpha$ = 0.46), Ru/BaO-$CaH_2$ ($\alpha$ = 0.47), Ru/$CaH_2$ ($\alpha$ = 0.57) [106] and Ru/$[Ca_{24}Al_{28}O_{64}]^{4+}(O_2^-)_{2-x}$ $(e^-)_{2x}$ ($\alpha$ = 0.57) [75].

For the $CeNi_2$ and $CeNi_5$ catalysts, $\alpha$ values of 0.663 and 0.884 were reported [127], respectively, suggesting that the RDS involves a hydrogenation step for $NH_x$ in the case of $CeNi_2$, while $N_2$ dissociation is the RDS for $CeNi_5$. This accords with the observation that $CeNi_2$ reinforces higher ammonia synthesis activity.

For Ni/ReN (Re = Ce, La) catalysts, $\alpha$ was estimated to be 1.2 [27]. In both cases, however, the RDS for ammonia synthesis is the hydrogenation of lattice nitrogen via the reaction N + H $\rightarrow$ NH, occurring on the surface of LaN and CeN, respectively. For Ni/YN, however, the overall activation barrier is primarily governed by the hydrogenation of $NH_2$ species. For CeN NPs, $Co_3Mo_3N$, and Ru/Ba-$Ca(NH_2)_2$, the value of $\alpha$ was 1.0 [27], despite the activation energy being relatively low (Table 1).

The reaction orders for the Ni/CeN catalyst were determined to be $\alpha$ ($N_2$) = 1.2 (1.2), $\beta$ ($H_2$) = 1.6 (1.2), and $\gamma$ ($NH_3$) = $-1.4$ ($-1.7$) [27]. For $CeNi_2$, the corresponding values were 0.663, 1.089, and $-0.725$, while for $CeNi_5$, they were 0.884, 0.633, and $-0.690$, respectively [127]. These $\beta$ values revealed the absence of hydrogen poisoning issues on these catalysts. The negative value of $\gamma$ for all three catalysts indicated notable adsorption of $NH_3$, leading to coverage on the catalyst surface. For the catalysts, including Ni/CeN, CeN, Ni/LaN, $Co_3Mo_3N$, LaRuSi,

Ru/Ba-Ca($NH_2$), and Cs-Ru/MgO, and $BaH_2$-BaO/Fe/$CaH_2$, Ru/$BaH_2$-BaO, Ru powder, and Ru-Cs/MgO, the reaction orders with respect to $NH_3$ were approximately −1.4, −1.6, −1.7, −1.3, −1.05, −0.9, −0.35 [27], −1.1 and −1.7 [122], −0.15 and −0.12 [118], respectively.

The reaction order of $N_2$ over the intermetallic catalyst LaCoSi was reported as 0.45 [106], suggesting that $N_2$ dissociation occurs rapidly enough to maintain a surface saturated with activated nitrogen. This behavior closely resembles that of high-performance ruthenium-loaded electride catalysts [118] and Co–LiH [131], where the RDS is no longer $N_2$ cleavage. Kinetic analysis, involving linear regression between calculated and experimental synthesis rates [106], assessed reaction rates over LaCoSi using rate equations derived from various reaction steps. The analysis was based on three key assumptions: (1) ammonia synthesis proceeds via eight elementary steps, (2) one step controls the overall reaction rate, and (3) adsorption follows the Langmuir model.

This analysis yielded a relatively low $R^2$ value of 0.583 for $N_2$ activation, whereas hydrogenation steps, N + H → NH, NH + H → $NH_2$, and $NH_2$ + H → $NH_3$, had significantly higher $R^2$ values of 0.930, 0.982, and 0.987, respectively. The highest correlation for hydrogenation steps strongly suggests that the RDS for ammonia synthesis over LaCoSi is one of the $NH_x$ formation steps rather than $N_2$ dissociation. This conclusion aligns with findings for ruthenium-loaded $C_{12}A_7{:}e^-$, where a similar shift in the RDS was observed [118]. Morimoto et al. [278] reported a similar trend for Ru and Ru + K catalysts but suggested that temperature dependence might determine whether the RDS involves N + H → NH or $NH_2$ + H → $NH_3$.

For Co/SrNH, Fe/SrNH, Ni/SrNH, and Ni/CaNH catalysts, the $N_2$ reaction order falls within a narrow range of 1.1–1.2, while $H_2$ exhibits a broader range from 1.7 (Co/SrNH) and 1.6 (Fe/SrNH) to significantly lower values of 0.2 (Ni/CaNH) and 0.1 (Ni/SrNH) [116]. The drastic reduction in β for Ni-based catalysts is attributed to slow consumption of dissociatively adsorbed H, leading to hydrogen accumulation on the Ni surface and resistance to hydrogen poisoning. Higher activation energies—0.973 eV for Ni/CaNH and 0.955 eV for Ni/SrNH, compared to 0.546 eV for Co/SrNH and 0.492 eV for Fe/SrNH—further support this distinction, suggesting a unique catalytic mechanism for Ni/CaNH and Ni/SrNH.

A dual reaction mechanism [116] has been proposed for hydrogenation on Ni-based catalysts, involving $N_2$ activation at (1) Co metal sites and (2) $NH_2^-$ vacancy sites on the SrNH support. The RDS for ammonia formation is the coupling of H with $NH_2^-$ vacancies ($NH_2$ + H → $NH_3$), a process observed in Ni/SrNH and exhibiting a high activation barrier, similar to Co/SrNH, Ni/LaN, and Ni/CeN. Among these, Co/SrNH demonstrates the highest catalytic efficiency for ammonia synthesis.

For Ru/Ba(10)-$TiH_2$ and Ru–Cs/MgO catalysts [76], the respective values of α, β, and γ were 0.15 (−0.59), 0.79 (0.89), and −0.36 (0.11). These results indicate that Ru/Ba(10)-$TiH_2$ could exhibit appreciable ammonia synthesis activity and is less susceptible to hydrogen poisoning than Ru–Cs/MgO.

Potassium modifies the ammonia reaction order from −0.6 to −0.35 and the hydrogen reaction order from 0.76 to 0.44 on the (100) and (111) faces of iron [72]. However, within experimental error, the activation energy remains unchanged, implying that the fundamental ammonia synthesis mechanism is not altered. The increase in apparent ammonia order from −0.6 on clean Fe(100) to −0.35 on K/Fe(100) reflects this modification.

For Ru(0001), the RDS is proposed to be $N_2$ dissociation, with an activation energy of 1.3 eV, despite DFT calculations suggesting that $NH_2$ formation presents the highest energy barrier [146]. Tautermann et al. [279] noted that at low temperatures (<200 K), the reactions N + H → NH and NH + H → $NH_2$ may act as the RDS, though this is irrelevant to the Haber–Bosch process. Zhang et al. [144] further corroborated this, reporting activation energies of

1.29 eV for N + H → NH and 1.36 eV for $N_2$ → 2N, suggesting that $N_2$ dissociation is the true rate-limiting step.

## 7. Discussion and Conclusions

Jocobi [280] highlighted discrepancies between real-world catalyst performance and single-crystal DFT predictions, emphasizing the importance of studying 2 nm Ru metal particles on various supports to advance understanding of ammonia synthesis over Ru-based catalysts. This discrepancy arises because typical single-crystal DFT models represent idealized, flat surfaces—such as Ru(0001)—that fail to capture the diversity of active sites present on real nanoparticle catalysts. In practice, Ru and Fe NPs may expose a mix of terraces, steps, edges, ledges, kinks, and corners—features that generate undercoordinated sites like B5 and C7, which often serve as the true reactive centers for $N_2$ dissociation. Small slab models (e.g., 2 × 2 unit-cells with ~36 atoms) are too limited to include such sites. To capture them, one must construct larger supercells (e.g., 4 × 3 or 5 × 3) or explicitly model high-index facets like Ru(10$\bar{1}$2) or stepped surfaces such as Ru(11$\bar{2}$1) and Ru(10$\bar{1}$5), which naturally expose these low-coordination geometries. These models, typically exceeding 100 atoms, are computationally demanding, but necessary for bridging the gap between theoretical predictions and actual catalytic behavior, particularly in reactions like $N_2$ activation that are sensitive to surface structure.

Beyond B5 and C7 sites, step-edge, corner (e.g., intersection of multiple facets on an NP), and defect sites significantly influence $N_2$ dissociation. These sites, especially at step-edges, kinks or corners, are more reactive than terrace sites due to their lower coordination number. For instance, corner sites—where two steps meet—are particularly reactive, as are defect-oriented sites like vacancies, which stabilize reactive intermediates. These surface features—though their mechanistic roles are yet to be fully elucidated—are crucial for enhancing catalytic efficiency by promoting the activation and cleavage of the N≡N bond, followed by subsequent hydrogenation and desorption steps.

There exists no singular, universally applicable rule for the straightforward identification of active sites in newly designed or yet-to-be-identified catalysts that facilitate the molecular or dissociative adsorption of $N_2$ without thorough theoretical inspection. Consequently, the mechanistic pathways governing ammonia synthesis activity processes cannot be generalized across all catalytic systems. Nevertheless, the associative mechanism emerges as predominant over its dissociative counterpart when the adsorption strength of molecular $N_2$ exceeds a critical threshold around −1.0 eV. The manifestation of a particular reaction mechanism is intricately orientation-dependent for $N_2$, intertwined with the nature of the chemical or physical interactions governing reactant adsorption. Furthermore, hybrid mechanistic pathways, characterized by associative and dissociative components, may dominate under certain catalytic conditions, particularly in vacancy-assisted catalytic systems, wherein enhanced mechanistic complexity is likely to arise.

While different catalysts follow varying reaction mechanism, such as LH for Ru, Co, and Fe, ER/MvK for transition metal nitrides, or distal, alternating, and mixed associative-dissociative concerted pathways for ammonia synthesis, the exploration of these mechanisms remains confined to a limited set of catalyst systems. If molecular adsorption of $N_2$ is stronger than its dissociative adsorption, the LH mechanism may not be applicable, as it depends on the dissociation of $N_2$ into reactive intermediates (such as atomic N). In such cases, alternative mechanisms such as the LR, ER, MVK, or hybrid models could be more suitable, where $N_2$ remains molecularly adsorbed, and hydrogen atoms or $H_2$ participate in the reaction through different pathways. Therefore, to optimize catalyst design, researchers should focus on elucidating all possible pathways for each catalyst using advanced experimental techniques, including isotope labeling, surface science methods, and in-situ

spectroscopy, alongside computational modeling. These approaches will yield a deeper understanding of the intricate processes occurring on the catalyst surface. Furthermore, developing high-throughput screening techniques for evaluating diverse catalysts will enhance our ability to design more efficient and stable transition metal heterogeneous catalysts for ammonia synthesis.

The use of promoters enhances ammonia synthesis activity through two distinct mechanisms. First, they induce an electronic charge transfer to the catalyst, generating active sites that strengthen the nitrogen-iron bond through moderate adsorption while weakening the nitrogen-nitrogen bond. This dual action activates the adsorbed $N_2$ and facilitates its seamless dissociation. Second, they orchestrate localized surface modifications, creating specialized sites where $NH_3$, produced during hydrogenation, is weakly adsorbed. This process not only eases the desorption of $NH_3$ but also prevents surface blockage, ensuring the continuous and efficient adsorption of $N_2$, thereby facilitating the recycling of the catalytic process.

While many studies have proposed dissociatively adsorbed $N_2$ [60] and the desorption of $NH_3$ [36] from the catalyst surface, such as $Mo_2N$ [281,282] and Ru [15] as potential rate-limiting steps, these are consistent with the suggestions that have been made [283,284] based on the theory of Temkin and Pyzhev [273]. Recent discussions, however, support the idea proposed by Enomoto et al. [285] in 1952, which suggests that the reaction N + H $\rightarrow$ NH (and other hydrogenation steps) could be the slow step in the process [31] and, therefore, should be considered as the RDS.

For most Ru-based catalysts, the RDS is the dissociation of $N_2$, indicated by near-unity $\alpha$ values, suggesting $N_2$ activation as the primary rate-limiting factor. However, in ruthenium-loaded electrides, the RDS shifts to the hydrogenation step. This shift occurs because the electride phase provides a highly efficient electron source, facilitating faster $N_2$ cleavage and lowering the energy required for $N_2$ activation. As a result, the hydrogenation step becomes the new rate-limiting step, lowering the $\alpha$ value for $N_2$ ($\alpha < 1$) and reducing the overall activation energy. The shift in RDS is further influenced by the specific electronic structure of the electrides, which alters the interactions between hydrogen and the catalyst surface, making the hydrogenation step more pronounced. However, for catalysts such as Co/C12A7:$e^-$, Ni/CeN, Ni/LaN, and CeN NPs, and $Co_3Mo_3N$ [24], which feature low activation energies ($E_a$ << 60 kJ mol$^{-1}$), $\alpha$ remains close to 1.0, even though the RDS is the hydrogenation step (N + $H_x$ $\rightarrow$ $NH_x$) due to a complex interplay of vacancy-driven hydrogenation.

Variations in $\beta$ reflect the impact of hydrogen adsorption, with hydrogen poisoning observed in some Ru-based catalysts, which can be mitigated by promoters such as Ba, Ce and La (and their oxides), among others. These promoters modify the catalyst surface topology, enhancing charge transfer and reducing the negative effects of hydrogen poisoning by altering hydrogen adsorption energies. Despite these insights, the relationship between RDS and reaction order remains incompletely understood, particularly regarding the specific conditions—such as catalyst composition, temperature, and reaction environment—that trigger the shift in RDS.

Future research should perhaps focus on elucidating the atomic and electronic mechanisms through which promoters influence hydrogen adsorption and the RDS while investigating temperature and pressure dependencies across diverse catalyst systems. These insights will be crucial for predicting catalyst performance under industrial conditions. However, these mechanistic advances must be considered within the broader context of the challenges faced by ammonia synthesis, particularly regarding energy consumption and carbon emissions.

Despite over a century of dominance in industrial ammonia synthesis, the Haber–Bosch process remains an energy-intensive and carbon-emitting technology, largely due

to its reliance on high-temperature, high-pressure conditions and hydrogen derived from fossil fuels. Advances in catalyst design, integration with renewable hydrogen (enabling green ammonia), and emerging electrochemical methods have shown promise, but remain limited by cost, scalability, and technical maturity. From a policy perspective, accelerating the adoption of low-carbon alternatives will require coordinated investment in R&D, infrastructure for green hydrogen, and regulatory frameworks that support sustainable production without jeopardizing global food security. Looking ahead, novel catalyst architectures—such as electrides, nitrides, hydrides, and bi-, tri-, and multi-metallic (high-entropy) alloy systems—may offer pathways to improved efficiency. Ultimately, the long-term goal is to emulate nature's own solution: nitrogenase enzymes, which fix nitrogen at ambient temperature and pressure with remarkable selectivity and efficiency.

**Author Contributions:** Conceptualization and problem design, P.R.V.; literature search, drawing of figures and analysis, P.R.V.; supervision, P.R.V.; writing—original draft, P.R.V.; writing—review and editing, P.R.V., H.M.M. and I.G. All authors have read and agreed to the published version of the manuscript.

**Funding:** This research received no external funding.

**Institutional Review Board Statement:** Not applicable.

**Informed Consent Statement:** Not applicable.

**Data Availability Statement:** This research used data reported in the manuscript itself.

**Acknowledgments:** This review was conducted using resources from the University of the Witwatersrand and the Institute of Physics at Nicolaus Copernicus University in Toruń. While limited access to facilities at Nagoya University was available during an earlier stage of P.R.V.'s appointment, the review was conceptualized after December 2024 and completed independently. All research, analysis, and writing were carried out using facilities provided by the University of the Witwatersrand and Nicolaus Copernicus University in Toruń. No material or financial support was received from Nagoya University for this review.

**Conflicts of Interest:** The authors declare that no known financial or personal conflicts of interest could have influenced the content or results presented in this paper.

## References

1. Liu, H. *Ammonia Synthesis Catalysts*; World Scientific: Singapore, 2013.
2. Haber, F.; van Oordt, G. Über die Bildung von Ammoniak den Elementen. *Zeit. Anorg. Chem.* **1905**, *44*, 341–378. [CrossRef]
3. Haber, F. The synthesis of ammonia from its elements Nobel Lecture, June 2, 1920. *Resonance* **2002**, *7*, 86–94. [CrossRef]
4. Carl Bosch Nobel Lecture. 1932. Available online: https://www.nobelprize.org/prizes/chemistry/1931/bosch/lecture/ (accessed on 15 March 2025).
5. Schlögl, R. Catalytic Synthesis of Ammonia—A "Never-Ending Story"? *Angew. Chem. Int. Ed.* **2003**, *42*, 2004–2008. [CrossRef]
6. Smith, C.; Hill, A.K.; Torrente-Murciano, L. Current and future role of Haber–Bosch ammonia in a carbon-free energy landscape. *Energy Environ. Sci.* **2020**, *13*, 331–344. [CrossRef]
7. Erisman, J.W.; Sutton, M.A.; Galloway, J.; Klimont, Z.; Winiwarter, W. How a century of ammonia synthesis changed the world. *Nat. Geosci.* **2008**, *1*, 636–639. [CrossRef]
8. Hellman, A.; Baerends, E.J.; Biczysko, M.; Bligaard, T.; Christensen, C.H.; Clary, D.C.; Dahl, S.; van Harrevelt, R.; Honkala, K.; Jonsson, H.; et al. Predicting Catalysis: Understanding Ammonia Synthesis from First-Principles Calculations. *J. Phys. Chem. B* **2006**, *110*, 17719–17735. [CrossRef] [PubMed]
9. Somorjai, G.A. The Evolution of Surface Chemistry. A Personal View of Building the Future on Past and Present Accomplishments. *J. Phys. Chem. B* **2002**, *106*, 9201–9213. [CrossRef]
10. Emmett, P.H.; Brunauer, S. The Use of Low Temperature van der Waals Adsorption Isotherms in Determining the Surface Area of Iron Synthetic Ammonia Catalysts. *J. Am. Chem. Soc.* **1937**, *59*, 1553–1564. [CrossRef]
11. Emmett, P.H.; Brunauer, S. The Adsorption of Nitrogen by Iron Synthetic Ammonia Catalysts. *J. Am. Chem. Soc.* **1934**, *56*, 35–41. [CrossRef]

12. Mittasch, A.; Frankenburg, W. Early Studies of Multicomponent Catalysts. In *Advances in Catalysis*; Frankenburg, W.G., Komarewsky, V.I., Rideal, E.K., Eds.; Elsevier: Amsterdam, The Netherlands, 1950; Volume 2, pp. 81–104.
13. Gerhard Ertl Nobel Lecture 2007. Available online: https://www.nobelprize.org/prizes/chemistry/2007/ertl/lecture/ (accessed on 17 March 2025).
14. Bowker, M. The 2007 Nobel Prize in Chemistry for Surface Chemistry: Understanding Nanoscale Phenomena at Surfaces. *ACS Nano* **2007**, *1*, 253–257. [CrossRef]
15. Aika, K.-I.; Ozaki, A. Kinetics and isotope effect of ammonia synthesis over ruthenium. *J. Catal.* **1970**, *16*, 97–101. [CrossRef]
16. Aika, K.-I.; Ozaki, A. Mechanism of Ammonia Synthesis over Molybdenum Nitride. *Bull. Chem. Soc. Jpn.* **2006**, *41*, 2818. [CrossRef]
17. Spencer, N.D.; Somorjai, G.A. Rhenium: An ammonia synthesis catalyst. *J. Phys. Chem.* **1982**, *86*, 3493–3494. [CrossRef]
18. Bare, S.R.; Strongin, D.R.; Somorjai, G.A. Ammonia synthesis over iron single-crystal catalysts: The effects of alumina and potassium. *J. Phys. Chem.* **1986**, *90*, 4726–4729. [CrossRef]
19. Dahl, S.; Logadottir, A.; Jacobsen, C.J.H.; Nørskov, J.K. Electronic factors in catalysis: The volcano curve and the effect of promotion in catalytic ammonia synthesis. *Appl. Catal. A* **2001**, *222*, 19–29. [CrossRef]
20. Jacobsen, C.J.H.; Dahl, S.; Clausen, B.S.; Bahn, S.; Logadottir, A.; Nørskov, J.K. Catalyst Design by Interpolation in the Periodic Table: Bimetallic Ammonia Synthesis Catalysts. *J. Am. Chem. Soc.* **2001**, *123*, 8404–8405. [CrossRef]
21. Logadottir, A.; Rod, T.H.; Nørskov, J.K.; Hammer, B.; Dahl, S.; Jacobsen, C.J.H. The Brønsted–Evans–Polanyi Relation and the Volcano Plot for Ammonia Synthesis over Transition Metal Catalysts. *J. Catal.* **2001**, *197*, 229–231. [CrossRef]
22. Loffreda, D.; Delbecq, F.; Vigné, F.; Sautet, P. Fast Prediction of Selectivity in Heterogeneous Catalysis from Extended Brønsted–Evans–Polanyi Relations: A Theoretical Insight. *Angew. Chem. Int. Ed.* **2009**, *48*, 8978–8980. [CrossRef] [PubMed]
23. Cheng, J.; Hu, P.; Ellis, P.; French, S.; Kelly, G.; Lok, C.M. Brønsted−Evans−Polanyi Relation of Multistep Reactions and Volcano Curve in Heterogeneous Catalysis. *J. Phys. Chem. C* **2008**, *112*, 1308–1311. [CrossRef]
24. Kitano, M.; Inoue, Y.; Ishikawa, H.; Yamagata, K.; Nakao, T.; Tada, T.; Matsuishi, S.; Yokoyama, T.; Hara, M.; Hosono, H. Essential role of hydride ion in ruthenium-based ammonia synthesis catalysts. *Chem. Sci.* **2016**, *7*, 4036–4043. [CrossRef]
25. Kobayashi, Y.; Kitano, M.; Kawamura, S.; Yokoyama, T.; Hosono, H. Kinetic evidence: The rate-determining step for ammonia synthesis over electride-supported Ru catalysts is no longer the nitrogen dissociation step. *Catal. Sci. Technol.* **2017**, *7*, 47–50. [CrossRef]
26. Hosono, H. Spiers Memorial Lecture: Catalytic activation of molecular nitrogen for green ammonia synthesis: Introduction and current status. *Faraday Discuss.* **2023**, *243*, 9–26. [CrossRef] [PubMed]
27. Ye, T.N.; Park, S.W.; Lu, Y.; Li, J.; Sasase, M.; Kitano, M.; Hosono, H. Contribution of Nitrogen Vacancies to Ammonia Synthesis over Metal Nitride Catalysts. *J. Am. Chem. Soc.* **2020**, *142*, 14374–14383. [CrossRef] [PubMed]
28. Taylor, H.S. A theory of the catalytic surface. *Proc. Roy. Soc. A* **1925**, *108*, 105–111.
29. Boudart, M. Kinetics and Mechanism of Ammonia Synthesis. *Catal. Rev.* **1981**, *23*, 1–15. [CrossRef]
30. Boudart, M. Kinetics on ideal and real surfaces. *AIChE J.* **1956**, *2*, 62–64. [CrossRef]
31. Ozaki, A.; Taylor, H.S.; Boudart, M. Kinetics and mechanism of the ammonia synthesis. *Proc. R. Soc. A* **1960**, *258*, 47–62. [CrossRef]
32. Nadiri, S.; Attari Moghaddam, A.; Folke, J.; Ruland, H.; Shu, B.; Fernandes, R.; Schlögl, R.; Krewer, U. Ammonia Synthesis Rate Over a Wide Operating Range: From Experiments to Validated Kinetic Models. *ChemCatChem* **2024**, *16*, e202400890. [CrossRef]
33. Dyson, D.C.; Simon, J.M. Kinetic Expression with Diffusion Correction for Ammonia Synthesis on Industrial Catalyst. *Ind. Eng. Chem. Fundam.* **1968**, *7*, 605–610. [CrossRef]
34. Sehested, J.; Jacobsen, C.J.H.; Törnqvist, E.; Rokni, S.; Stoltze, P. Ammonia Synthesis over a Multipromoted Iron Catalyst: Extended Set of Activity Measurements, Microkinetic Model, and Hydrogen Inhibition. *J. Catal.* **1999**, *188*, 83–89. [CrossRef]
35. Stoltze, P. Surface science as the basis for the understanding of the catalytic synthesis of ammonia. *Phys. Scr.* **1987**, *36*, 824–864. [CrossRef]
36. Spencer, M.S. On the rate-determining step and the role of potassium in the catalytic synthesis of ammonia. *Catal. Lett.* **1992**, *13*, 45–53. [CrossRef]
37. Mathisen, K.; Kirste, K.G.; Hargreaves, J.S.J.; Laassiri, S.; McAulay, K.; McFarlane, A.R.; Spencer, N.A. An In Situ XAS Study of the Cobalt Rhenium Catalyst for Ammonia Synthesis. *Top. Catal.* **2018**, *61*, 225–239. [CrossRef] [PubMed]
38. McAulay, K.; Hargreaves, J.S.J.; McFarlane, A.R.; Price, D.J.; Spencer, N.A.; Bion, N.; Can, F.; Richard, M.; Greer, H.F.; Zhou, W.Z. The influence of pre-treatment gas mixture upon the ammonia synthesis activity of Co–Re catalysts. *Catal. Commun.* **2015**, *68*, 53–57. [CrossRef]
39. Bowker, M.; Parker, I.B.; Waugh, K.C. Extrapolation of the kinetics of model ammonia synthesis catalysts to industrially relevant temperatures and pressures. *Appl. Catal. A* **1985**, *14*, 101–118. [CrossRef]
40. Brill, R. Kinetics and Poisoning in Ammonia Synthesis. *Angew. Chem. Int. Ed. Engl.* **1963**, *2*, 221–222. [CrossRef]
41. Humphreys, J.; Lan, R.; Tao, S. Development and Recent Progress on Ammonia Synthesis Catalysts for Haber–Bosch Process. *Adv. Energy Sustain. Res.* **2021**, *2*, 2000043. [CrossRef]

42. Park, S.Y.; Jang, Y.J.; Youn, D.H. A Review of Transition Metal Nitride-Based Catalysts for Electrochemical Nitrogen Reduction to Ammonia. *Catalysts* **2023**, *13*, 639. [CrossRef]
43. Stoltze, P.; Norskov, J.K. Bridging the "pressure gap" between ultrahigh-vacuum surface physics and high-pressure catalysis. *Phys. Rev. Lett.* **1985**, *55*, 2502–2505. [CrossRef]
44. Wang, P.; Gong, S.; Li, Y.; Mo, Y. Bond dissociation energy of $N_2$ measured by state-to-state resolved threshold fragment yield spectra. *J. Chem. Phys.* **2024**, *160*, 014304. [CrossRef]
45. Wyckoff, R.W.G.; Crittenden, E.D. An X-ray Examination of Some Ammonia Catalysts. *J. Am. Chem. Soc.* **1925**, *47*, 2866–2876. [CrossRef]
46. Silverman, D.C.; Boudart, M. Surface composition of promoted iron catalysts. *J. Catal.* **1982**, *77*, 208–220. [CrossRef]
47. Era, K.; Sato, K.; Miyahara, S.-I.; Naito, T.; De Silva, K.; Akrami, S.; Yamada, H.; Toriyama, T.; Tamaoka, T.; Yamamoto, T.; et al. Barium-doped iron nanoparticles supported on MgO as an efficient catalyst for ammonia synthesis under mild reaction conditions. *Sustain. Energy Fuels* **2024**, *8*, 2593–2600. [CrossRef]
48. Vieri, H.M.; Badakhsh, A.; Choi, S.H. Comparative Study of Ba, Cs, K, and Li as Promoters for Ru/La2Ce2O7-Based Catalyst for Ammonia Synthesis. *Int. J. Energy Res.* **2023**, *2023*, 2072245. [CrossRef]
49. Bozso, F.; Ertl, G.; Grunze, M.; Weiss, M. Interaction of nitrogen with iron surfaces: I. Fe(100) and Fe(111). *J. Catal.* **1977**, *49*, 18–41. [CrossRef]
50. Bozso, F.; Ertl, G.; Weiss, M. Interaction of nitrogen with iron surfaces: II. Fe(110). *J. Catal.* **1977**, *50*, 519–529. [CrossRef]
51. Dowben, P.A.; Grunze, M.; Jones, R.G. Nitrogen-induced reconstruction of a stepped iron surface. *Surf. Sci. Lett.* **1981**, *109*, L519–L526. [CrossRef]
52. Miyazaki, M.; Ikejima, K.; Ogasawara, K.; Kitano, M.; Hosono, H. Ammonia Synthesis over Fe-Supported Catalysts Mediated by Face-Sharing Nitrogen Sites in $BaTiO_3-N$ Oxynitride. *ChemSusChem* **2023**, *16*, e202300551. [CrossRef]
53. Ye, T.N.; Park, S.W.; Lu, Y.; Li, J.; Sasase, M.; Kitano, M.; Tada, T.; Hosono, H. Vacancy-enabled $N_2$ activation for ammonia synthesis on an Ni-loaded catalyst. *Nature* **2020**, *583*, 391–395. [CrossRef]
54. Ertl, G.; Lee, S.B.; Weiss, M. Adsorption of nitrogen on potassium promoted Fe(111) and (100) surfaces. *Surf. Sci.* **1982**, *114*, 527–545. [CrossRef]
55. Johnson, D.W.; Roberts, M.W. Nitrogen chemisorption by iron. *Surf. Sci.* **1979**, *87*, L255–L259. [CrossRef]
56. Liu, S.; Wang, M.; Ji, H.; Shen, X.; Yan, C.; Qian, T. Altering the rate-determining step over cobalt single clusters leading to highly efficient ammonia synthesis. *Nat. Sci. Rev.* **2020**, *8*, nwaa136. [CrossRef] [PubMed]
57. Roy, P.K.; Kumar, S. Strong Interfacial Electronic Interaction in the Transition-Metal/Mo2C Catalyst for Enhanced Ammonia Synthesis at Ambient Pressure: Shift of the Rate Determining Step. *ACS Appl. Energy Mater.* **2020**, *3*, 7167–7179. [CrossRef]
58. Appl, M. The Haber-Bosch Heritage: The Ammonia Production Technology. In Proceedings of the 50th Anniversary of the IFA Technical Conference, Seville, Spain, 25–26 September 1997.
59. Bowker, M. Modelling of ammonia synthesis kinetics. *Catal. Today* **1992**, *12*, 153–163. [CrossRef]
60. Ertl, G. Surface Science and Catalysis—Studies on the Mechanism of Ammonia Synthesis: The P. H. Emmett Award Address. *Catal. Rev.* **1980**, *21*, 201–223. [CrossRef]
61. Vandervell, H.D.; Waugh, K.C. On the role of promoters in promoted iron catalysts used in the industrial synthesis of ammonia. *Chem. Phys. Lett.* **1990**, *171*, 462–468. [CrossRef]
62. Hinrichsen, O.; Rosowski, F.; Hornung, A.; Muhler, M.; Ertl, G. The Kinetics of Ammonia Synthesis over Ru-Based Catalysts: 1. The Dissociative Chemisorption and Associative Desorption of N2. *J. Catal.* **1997**, *165*, 33–44. [CrossRef]
63. Wagner, J.; Grabnic, T.; Sibener, S.J. STM Visualization of N2 Dissociative Chemisorption on Ru(0001) at High Impinging Kinetic Energies. *J. Phys. Chem. C* **2022**, *126*, 18333–18342. [CrossRef] [PubMed]
64. Aika, K.-I. Heterogeneous Catalysis of Ammonia Synthesis at Room Temperature and Atmospheric Pressure. *Angew. Chem. Int. Ed.* **1986**, *25*, 558–559. [CrossRef]
65. Zhang, C.; Wang, Z.-H.; Wang, H.; Liang, J.-X.; Zhu, C.; Li, J. $Ru3@Mo_2CO_2$ MXene single-cluster catalyst for highly efficient $N_2$-to-$NH_3$ conversion. *Nat. Sci. Rev.* **2024**, *11*, nwae251. [CrossRef]
66. Cao, A.; Nørskov, J.K. Spin Effects in Chemisorption and Catalysis. *ACS Catal.* **2023**, *13*, 3456–3462. [CrossRef]
67. Xu, G.; Cai, C.; Wang, T. Toward Sabatier Optimal for Ammonia Synthesis with Paramagnetic Phase of Ferromagnetic Transition Metal Catalysts. *J. Am. Chem. Soc.* **2022**, *144*, 23089–23095. [CrossRef] [PubMed]
68. Liu, C.; Liu, Y.; Xu, G.; Wang, T. Associative-Distal Mechanism of the Haber–Bosch Process on a Ferrierite Catalyst with Spatially Isolated Dual Molybdenum Sites. *J. Phys. Chem. C* **2024**, *128*, 6711–6718. [CrossRef]
69. Xu, G.; Sun, L.; Wang, T. Demagnetizing Ferromagnetic Catalysts to the Sabatier Optimal of Haber–Bosch Process. *JACS Au* **2024**, *4*, 1405–1412. [CrossRef] [PubMed]
70. Era, K.; Sato, K.; Miyahara, S.-I.; Naito, T.; De Silva, K.; Akrami, S.; Yamada, H.; Toriyama, T.; Yamamoto, T.; Murakami, Y.; et al. Catalytic Behavior of K-doped Fe/MgO Catalysts for Ammonia Synthesis Under Mild Reaction Conditions. *ChemSusChem* **2023**, *16*, e202300942. [CrossRef] [PubMed]

71. Aika, K.; Tamara, K. Ammonia Synthesis over Non-Iron Catalysts and Related Phenomena. In *Ammonia: Catalysis and Manufacture*; Nielsen, A., Ed.; Springer: Berlin/Heidelberg, Germany, 1995; pp. 103–148.
72. Strongin, D.R.; Somorjai, G.A. The effects of potassium on ammonia synthesis over iron single-crystal surfaces. *J. Catal.* **1988**, *109*, 51–60. [CrossRef]
73. Verschoor, J.C.; de Jongh, P.E.; Ngene, P. Recent advances in thermocatalytic ammonia synthesis and decomposition. *Curr. Opin. Green Sustain. Chem.* **2024**, *50*, 100965. [CrossRef]
74. Goto, Y.; Kikugawa, M.; Kobayashi, K.; Manaka, Y.; Nanba, T.; Matsumoto, H.; Matsumoto, M.; Aoki, M.; Imagawa, H. Facile formation of barium titanium oxyhydride on a titanium hydride surface as an ammonia synthesis catalyst. *RSC Adv.* **2023**, *13*, 15410–15415. [CrossRef]
75. Kanbara, S.; Kitano, M.; Inoue, Y.; Yokoyama, T.; Hara, M.; Hosono, H. Mechanism Switching of Ammonia Synthesis Over Ru-Loaded Electride Catalyst at Metal-Insulator Transition. *J. Am. Chem. Soc.* **2015**, *137*, 14517–14524. [CrossRef]
76. Huang, J.; Yuan, M.; Li, X.; Wang, Y.; Li, M.; Li, J.; You, Z. Inhibited hydrogen poisoning for enhanced activity of promoters-Ru/Sr2Ta2O7 nanowires for ammonia synthesis. *J. Catal.* **2020**, *389*, 556–565. [CrossRef]
77. Drummond, S.M.; Naglic, J.; Onsree, T.; Balijepalli, S.K.; Allegro, A.; Orraca Albino, S.N.; O'Connell, K.M.; Lauterbach, J. Promoted Ru/PrOx Catalysts for Mild Ammonia Synthesis. *Catalysts* **2024**, *14*, 572. [CrossRef]
78. Aika, K.-I.; Takano, T.; Murata, S. Preparation and characterization of chlorine-free ruthenium catalysts and the promoter effect in ammonia synthesis: 3. A magnesia-supported ruthenium catalyst. *J. Catal.* **1992**, *136*, 126–140. [CrossRef]
79. Zhang, T.; Hu, H.; Li, J.; Gao, Y.; Li, L.; Zhang, M.; Peng, X.; Zhou, Y.; Ni, J.; Lin, B.; et al. Tuning clusters-metal oxide promoters electronic interaction of Ru-based catalyst for ammonia synthesis under mild conditions. *Chin. J. Catal.* **2024**, *60*, 209–218. [CrossRef]
80. Perdew, J.P.; Burke, K.; Ernzerhof, M. Generalized gradient approximation made simple. *Phys. Rev. Lett.* **1996**, *77*, 3865–3868. [CrossRef] [PubMed]
81. Perdew, J.P.; Burke, K.; Ernzerhof, M. Generalized Gradient Approximation Made Simple. *Phys. Rev. Lett.* **1997**, *78*, 1396. [CrossRef]
82. Langmuir, I. Chemical Reactions at Low Pressures. *J. Am. Chem. Soc.* **1915**, *37*, 1139–1167. [CrossRef]
83. Onwudinanti, C.; Brocks, G.; Koelman, V.; Morgan, T.; Tao, S. Hydrogen diffusion out of ruthenium—An ab initio study of the role of adsorbates. *Phys. Chem. Chem. Phys.* **2020**, *22*, 7935–7941. [CrossRef]
84. Zhao, X. *Adsorbate-Adsorbate Interactions on Metal and Metal Oxide Surfaces*; Technischen Universität Berlin: Berlin, Germany, 2015.
85. García-García, F.R.; Guerrero-Ruiz, A.; Rodríguez-Ramos, I. Role of B5-Type Sites in Ru Catalysts used for the $NH_3$ Decomposition Reaction. *Top. Catal.* **2009**, *52*, 758–764. [CrossRef]
86. Arevalo, R.L.; Aspera, S.M.; Sison Escaño, M.C.; Nakanishi, H.; Kasai, H. First principles study of methane decomposition on B5 step-edge type site of Ru surface. *J. Phys. Cond. Matter* **2017**, *29*, 184001. [CrossRef]
87. Shadravan, V.; Cao, A.; Bukas, V.J.; Grønborg, M.K.; Damsgaard, C.D.; Wang, Z.; Kibsgaard, J.; Nørskov, J.K.; Chorkendorff, I. Enhanced promotion of Ru-based ammonia catalysts by in situ dosing of Cs. *Energy Environ. Sci.* **2022**, *15*, 3310–3320. [CrossRef]
88. Liu, L.; Shi, Y.; Rong, J.; Wang, Q.; Zhong, M. Adsorption Property and Morphology Evolution of C Deposited on HCP Co Nanoparticles. *Molecules* **2024**, *29*, 4760. [CrossRef] [PubMed]
89. Hughes, A.E.; Haque, N.; Northey, S.A.; Giddey, S. Platinum Group Metals: A Review of Resources, Production and Usage with a Focus on Catalysts. *Resources* **2021**, *10*, 93. [CrossRef]
90. Comas-Vives, A.; Larmier, K.; Copéret, C. Understanding surface site structures and properties by first principles calculations: An experimental point of view! *Chem. Commun.* **2017**, *53*, 4296–4303. [CrossRef]
91. Jacobsen, C.J.H.; Dahl, S.; Hansen, P.L.; Törnqvist, E.; Jensen, L.; Topsøe, H.; Prip, D.V.; Møenshaug, P.B.; Chorkendorff, I. Structure sensitivity of supported ruthenium catalysts for ammonia synthesis. *J. Molec. Catal. A* **2000**, *163*, 19–26. [CrossRef]
92. Cao, A.; Bukas, V.J.; Shadravan, V.; Wang, Z.; Li, H.; Kibsgaard, J.; Chorkendorff, I.; Nørskov, J.K. A spin promotion effect in catalytic ammonia synthesis. *Nat. Commun.* **2022**, *13*, 2382. [CrossRef] [PubMed]
93. Zeinalipour-Yazdi, C.D. Topology of active site geometries in HCP and FCC nanoparticles and surfaces. *Chem. Phys.* **2022**, *559*, 111532. [CrossRef]
94. van Hardeveld, R.; van Montfoort, A. The influence of crystallite size on the adsorption of molecular nitrogen on nickel, palladium and platinum: An infrared and electron-microscopic study. *Surf. Sci.* **1966**, *4*, 396–430. [CrossRef]
95. Spencer, N.D.; Schoonmaker, R.C.; Somorjai, G.A. Iron single crystals as ammonia synthesis catalysts: Effect of surface structure on catalyst activity. *J. Catal.* **1982**, *74*, 129–135. [CrossRef]
96. Somorjai, G.A.; Materer, N. Surface structures in ammonia synthesis. *Top. Catal.* **1994**, *1*, 215–231. [CrossRef]
97. Zhang, B.-Y.; Su, H.-Y.; Liu, J.-X.; Li, W.-X. Interplay Between Site Activity and Density of BCC Iron for Ammonia Synthesis Based on First-Principles Theory. *ChemCatChem* **2019**, *11*, 1928–1934. [CrossRef]
98. Ishikawa, A.; Doi, T.; Nakai, H. Catalytic performance of Ru, Os, and Rh nanoparticles for ammonia synthesis: A density functional theory analysis. *J. Catal.* **2018**, *357*, 213–222. [CrossRef]

99. Ye, T.N.; Park, S.W.; Lu, Y.; Li, J.; Wu, J.; Sasase, M.; Kitano, M.; Hosono, H. Dissociative and Associative Concerted Mechanism for Ammonia Synthesis over Co-Based Catalyst. *J. Am. Chem. Soc.* **2021**, *143*, 12857–12866. [CrossRef] [PubMed]
100. Rojas, K.I.M.; Cuong, N.T.; Nishino, H.; Ishibiki, R.; Ito, S.-I.; Miyauchi, M.; Fujimoto, Y.; Tominaka, S.; Okada, S.; Hosono, H.; et al. Chemical stability of hydrogen boride nanosheets in water. *Commun. Mater.* **2021**, *2*, 81. [CrossRef]
101. Hattori, M.; Iijima, S.; Nakao, T.; Hosono, H.; Hara, M. Solid solution for catalytic ammonia synthesis from nitrogen and hydrogen gases at 50 °C. *Nat. Commun.* **2020**, *11*, 2001. [CrossRef]
102. Inoue, Y.; Kitano, M.; Kishida, K.; Abe, H.; Niwa, Y.; Sasase, M.; Fujita, Y.; Ishikawa, H.; Yokoyama, T.; Hara, M.; et al. Efficient and Stable Ammonia Synthesis by Self-Organized Flat Ru Nanoparticles on Calcium Amide. *ACS Catal.* **2016**, *6*, 7577–7584. [CrossRef]
103. Kobayashi, Y.; Tang, Y.; Kageyama, T.; Yamashita, H.; Masuda, N.; Hosokawa, S.; Kageyama, H. Titanium-Based Hydrides as Heterogeneous Catalysts for Ammonia Synthesis. *J. Am. Chem. Soc.* **2017**, *139*, 18240–18246. [CrossRef] [PubMed]
104. Hargreaves, J.S.J. Nitrides as ammonia synthesis catalysts and as potential nitrogen transfer reagents. *Appl. Petrochem. Res.* **2014**, *4*, 3–10. [CrossRef]
105. Zeinalipour-Yazdi, C.D. Mechanistic aspects of ammonia synthesis on Ta3N5 surfaces in the presence of intrinsic nitrogen vacancies. *Phys. Chem. Chem. Phys.* **2021**, *23*, 6959–6963. [CrossRef]
106. Gong, Y.; Wu, J.; Kitano, M.; Wang, J.; Ye, T.-N.; Li, J.; Kobayashi, Y.; Kishida, K.; Abe, H.; Niwa, Y.; et al. Ternary intermetallic LaCoSi as a catalyst for $N_2$ activation. *Nat. Catal.* **2018**, *1*, 178–185. [CrossRef]
107. Qiu, J.-Z.; Hu, J.; Lan, J.; Wang, L.-F.; Fu, G.; Xiao, R.; Ge, B.; Jiang, J. Pure Siliceous Zeolite-Supported Ru Single-Atom Active Sites for Ammonia Synthesis. *Chem. Mater.* **2019**, *31*, 9413–9421. [CrossRef]
108. Cao, Y.; Toshcheva, E.; Almaksoud, W.; Ahmad, R.; Tsumori, T.; Rai, R.; Tang, Y.; Cavallo, L.; Kageyama, H.; Kobayashi, Y. Ammonia Synthesis via an Associative Mechanism on Alkaline Earth Metal Sites of $Ca_3CrN_3H$. *ChemSusChem* **2023**, *16*, e202300234. [CrossRef] [PubMed]
109. Kitano, M.; Kujirai, J.; Ogasawara, K.; Matsuishi, S.; Tada, T.; Abe, H.; Niwa, Y.; Hosono, H. Low-Temperature Synthesis of Perovskite Oxynitride-Hydrides as Ammonia Synthesis Catalysts. *J. Am. Chem. Soc.* **2019**, *141*, 20344–20353. [CrossRef] [PubMed]
110. Honkala, K.; Hellman, A.; Remediakis, I.N.; Logadottir, A.; Carlsson, A.; Dahl, S.; Christensen, C.H.; Nørskov, J.K. Ammonia synthesis from first-principles calculations. *Science* **2005**, *307*, 555–558. [CrossRef] [PubMed]
111. Hagen, S.; Barfod, R.; Fehrmann, R.; Jacobsen, C.J.H.; Teunissen, H.T.; Ståhl, K.; Chorkendorff, I. New Efficient Catalyst for Ammonia Synthesis: Barium-Promoted Cobalt on Carbon. *Chem. Commun.* **2002**, *11*, 1206–1207. [CrossRef]
112. Morlanés, N.; Almaksoud, W.; Rai, R.K.; Ould-Chikh, S.; Ali, M.; Vidjayacoumar, B.; Al-Sabban, B.; Albahily, K.; Basset, J.-M. Development of Catalysts for Ammonia Synthesis Based on Metal Phthalocyanine Materials. *Catal. Sci. Technol.* **2020**, *10*, 844–852. [CrossRef]
113. Zhang, X.; Liu, L.; Wu, A.; Zhu, J.; Si, R.; Guo, J.; Chen, R.; Jiang, Q.; Ju, X.; Feng, J.; et al. Synergizing Surface Hydride Species and Ru Clusters on $Sm_2O_3$ for Efficient Ammonia Synthesis. *ACS Catal.* **2022**, *12*, 2178–2190. [CrossRef]
114. Miyahara, S.-I.; Sato, K.; Tsujimaru, K.; Wada, Y.; Ogura, Y.; Toriyama, T.; Yamamoto, T.; Matsumura, S.; Inazu, K.; Nagaoka, K. Co Nanoparticle Catalysts Encapsulated by BaO–$La_2O_3$ Nanofractions for Efficient Ammonia Synthesis Under Mild Reaction Conditions. *ACS Omega* **2022**, *7*, 24452–24460. [CrossRef] [PubMed]
115. Zeinalipour-Yazdi, C.D.; Hargreaves, J.S.J.; Catlow, C.R.A. Low-T Mechanisms of Ammonia Synthesis on $Co_3Mo_3N$. *J. Phys. Chem. C* **2018**, *122*, 6078–6082. [CrossRef]
116. Li, Z.; Lu, Y.; Li, J.; Xu, M.; Qi, Y.; Park, S.-W.; Kitano, M.; Hosono, H.; Chen, J.-S.; Ye, T.-N. Multiple reaction pathway on alkaline earth imide supported catalysts for efficient ammonia synthesis. *Nat. Commun.* **2023**, *14*, 6373. [CrossRef]
117. Bai, Y.; Zhang, Y.; Hu, J.; Li, J.; Wan, S.; Lin, J.; Wang, Y.; Wang, S. Hydrogen-Assisted Dissociation of $N_2$: Prevalence and Consequences for Ammonia Synthesis on Supported Ru Catalysts. *ACS Catal.* **2025**, *15*, 1455–1466. [CrossRef]
118. Kitano, M.; Kanbara, S.; Inoue, Y.; Kuganathan, N.; Sushko, P.V.; Yokoyama, T.; Hara, M.; Hosono, H. Electride support boosts nitrogen dissociation over ruthenium catalyst and shifts the bottleneck in ammonia synthesis. *Nat. Commun.* **2015**, *6*, 6731. [CrossRef] [PubMed]
119. Raróg-Pilecka, W.; Miśkiewicz, E.; Kępiński, L.; Kaszkur, Z.; Kielar, K.; Kowalczyk, Z. Ammonia synthesis over barium-promoted cobalt catalysts supported on graphitised carbon. *J. Catal.* **2007**, *249*, 24–33. [CrossRef]
120. Sato, K.; Miyahara, S.-I.; Tsujimaru, K.; Wada, Y.; Toriyama, T.; Yamamoto, T.; Matsumura, S.; Inazu, K.; Mohri, H.; Iwasa, T.; et al. Barium Oxide Encapsulating Cobalt Nanoparticles Supported on Magnesium Oxide: Active Non-Noble Metal Catalysts for Ammonia Synthesis under Mild Reaction Conditions. *ACS Catal.* **2021**, *11*, 13050–13061. [CrossRef]
121. Hattori, M.; Mori, T.; Arai, T.; Inoue, Y.; Sasase, M.; Tada, T.; Kitano, M.; Yokoyama, T.; Hara, M.; Hosono, H. Enhanced Catalytic Ammonia Synthesis with Transformed BaO. *ACS Catal.* **2018**, *8*, 10977–10984. [CrossRef]
122. Hattori, M.; Okuyama, N.; Kurosawa, H.; Hara, M. Low-Temperature Ammonia Synthesis on Iron Catalyst with an Electron Donor. *J. Am. Chem. Soc.* **2023**, *145*, 7888–7897. [CrossRef]

123. Ogura, Y.; Sato, K.; Miyahara, S.I.; Kawano, Y.; Toriyama, T.; Yamamoto, T.; Matsumura, S.; Hosokawa, S.; Nagaoka, K. Efficient ammonia synthesis over a $Ru/La_{0.5}Ce_{0.5}O_{1.75}$ catalyst pre-reduced at high temperature. *Chem. Sci.* **2018**, *9*, 2230–2237. [CrossRef] [PubMed]
124. Wang, K.; Jin, B.; He, X.; Liang, X. Atomic layer deposition of Ru nanoclusters on Ba–$LaCeO_x$: A highly efficient catalyst for ammonia synthesis under mild conditions. *RSC Sustain.* **2024**, *2*, 3507–3519. [CrossRef]
125. Lee, K.; Woo, R.; Woo, H.C.; Ko, G.; Cho, K.; Park, Y.; Choi, M.; Yoon, H.C. Unraveling the Role of MgO in the Ru-Ba/MgO Catalyst for Boosting Ammonia Synthesis: Comparative Study of MgO and $MgAlO_x$ Supports. *J. Catal.* **2024**, *434*, 115530. [CrossRef]
126. Morimoto, R.; Ogawa, T.; Ueno, K.; Okumura, H.; Ishihara, K. Enhanced catalytic activity of ammonia synthesis over Ru/CaH2 by addition of oxygen. *ChemRxiv* **2022**. [CrossRef]
127. Arroyo-Caire, J.; Jiang, Y.; Diaz-Perez, M.A.; Lara-Angulo, M.A.; Miyazaki, M.; Serrano-Ruiz, J.C.; Kitano, M.; Hosono, H. $CeNi_x$ Alloys as Catalysts for Ammonia Synthesis: Insights on Ni–CeN Surface Layer Formation and Its Impact. *ACS Catal.* **2023**, *13*, 15715–15724. [CrossRef]
128. Jiang, Y.; Takashima, R.; Nakao, T.; Miyazaki, M.; Lu, Y.; Sasase, M.; Niwa, Y.; Abe, H.; Kitano, M.; Hosono, H. Boosted Activity of Cobalt Catalysts for Ammonia Synthesis with $BaAl_2O_4$–$xH_y$ Electrides. *J. Am. Chem. Soc.* **2023**, *145*, 10669–10680. [CrossRef] [PubMed]
129. Tsuji, Y.; Ogasawara, K.; Kitano, M.; Kishida, K.; Abe, H.; Niwa, Y.; Yokoyama, T.; Hara, M.; Hosono, H. Control of nitrogen activation ability by Co-Mo bimetallic nanoparticle catalysts prepared via sodium naphthalenide-reduction. *J. Catal.* **2018**, *364*, 31–39. [CrossRef]
130. Humphreys, J.; Lan, R.; Chen, S.; Walker, M.; Han, Y.; Tao, S. Cation Doped Cerium Oxynitride with Anion Vacancies for Fe-Based Catalyst with Improved Activity and Oxygenate Tolerance for Efficient Synthesis of Ammonia. *Appl. Catal. B* **2021**, *285*, 119843. [CrossRef]
131. Wang, P.; Chang, F.; Gao, W.; Guo, J.; Wu, G.; He, T.; Chen, P. Breaking scaling relations to achieve low-temperature ammonia synthesis through LiH-mediated nitrogen transfer and hydrogenation. *Nat. Chem.* **2017**, *9*, 64–70. [CrossRef] [PubMed]
132. Dahl, S.; Törnqvist, E.; Chorkendorff, I. Dissociative adsorption of N2 on ru(0001): A surface reaction totally dominated by steps. *J. Catal.* **2000**, *192*, 381–390. [CrossRef]
133. Razdan, N.K.; Bhan, A. Kinetic description of site ensembles on catalytic surfaces. *Proc. Natl. Acad. Sci. USA* **2021**, *118*, e2019055118. [CrossRef] [PubMed]
134. Farrauto, R.J. Industrial Catalysis: A Practical Guide. In *Handbook of Industrial Chemistry and Biotechnology*; Kent, J.A., Bommaraju, T.V., Barnicki, S.D., Eds.; Springer International Publishing: Cham, Switzerland, 2017; pp. 1995–2035.
135. Zhang, B.-Y.; Chen, P.-P.; Liu, J.-X.; Su, H.-Y.; Li, W.-X. Influence of Cobalt Crystal Structures on Activation of Nitrogen Molecule: A First-Principles Study. *J. Phys. Chem. C* **2019**, *123*, 10956–10966. [CrossRef]
136. Rivera Rocabado, D.S.; Noguchi, T.G.; Hayashi, S.; Maeda, N.; Yamauchi, M.; Ishimoto, T. Adsorption States of $N_2/H_2$ Activated on Ru Nanoparticles Uncovered by Modulation-Excitation Infrared Spectroscopy and Density Functional Theory Calculations. *ACS Nano* **2021**, *15*, 20079–20086. [CrossRef]
137. Mortensen, J.J.; Morikawa, Y.; Hammer, B.; Nørskov, J.K. Density Functional Calculations of $N_2$ Adsorption and Dissociation on a Ru(0001) Surface. *J. Catal.* **1997**, *169*, 85–92. [CrossRef]
138. Herron, J.A.; Tonelli, S.; Mavrikakis, M. Atomic and Molecular Adsorption on Ru(0001). *Surf. Sci.* **2013**, *614*, 64–74. [CrossRef]
139. Thomas, J.M. The existence of endothermic adsorption. *J. Chem. Ed.* **1961**, *38*, 138. [CrossRef]
140. Zeinalipour-Yazdi, C.D.; Hargreaves, J.S.J.; Laassiri, S.; Catlow, C.R.A. A comparative analysis of the mechanisms of ammonia synthesis on various catalysts using density functional theory. *Roy. Soc. Open Sci.* **2021**, *8*, 210952. [CrossRef] [PubMed]
141. Mortensen, J.J.; Hansen, L.B.; Hammer, B.; Nørskov, J.K. Nitrogen Adsorption and Dissociation on Fe(111). *J. Catal.* **1999**, *182*, 479–488. [CrossRef]
142. Agharezaei, P.; Tomohiro, N.G.; Kobayashi, H.; Schlenz, H.; Yamauchi, M.; Ghuman, K.K. Unraveling the Enhanced $N_2$ Activity on CuNi Alloy Catalysts for Ammonia Production: Experiments, DFT, and Statistical Analysis. *J. Phys. Chem. C* **2024**, *128*, 3703–3717. [CrossRef]
143. Higham, M.D.; Zeinalipour-Yazdi, C.D.; Zeinalipour-Yazdi, C.D.; Catlow, R.A.; Hargreaves, J.S.J. Mechanism of Ammonia Synthesis on $Fe_3Mo_3N$. *Faraday Discuss.* **2022**, *243*, 77–96. [CrossRef]
144. Zhang, C.J.; Lynch, M.; Hu, P. A density functional theory study of stepwise addition reactions in ammonia synthesis on Ru(0001). *Surf. Sci.* **2002**, *496*, 221–230. [CrossRef]
145. Lan, T.; Wang, H.; An, Q. Enabling high throughput deep reinforcement learning with first principles to investigate catalytic reaction mechanisms. *Nat. Commun.* **2024**, *15*, 6281. [CrossRef] [PubMed]
146. Logadóttir, Á.; Nørskov, J.K. Ammonia synthesis over a Ru(0001) surface studied by density functional calculations. *J. Catal.* **2003**, *220*, 273–279. [CrossRef]

147. Abghoui, Y.; Skúlason, E. Onset potentials for different reaction mechanisms of nitrogen activation to ammonia on transition metal nitride electro-catalysts. *Catal. Today* **2017**, *286*, 69–77. [CrossRef]
148. Mars, P.; van Krevelen, D.W. Oxidations carried out by means of vanadium oxide catalysts. *Chem. Eng. Sci.* **1954**, *3*, 41–59. [CrossRef]
149. Henkelman, G.; Jónsson, H. Improved tangent estimate in the nudged elastic band method for finding minimum energy paths and saddle points. *J. Chem. Phys.* **2000**, *113*, 9978–9985. [CrossRef]
150. Zeinalipour-Yazdi, C.D. A Comparison of the Mechanisms and Activation Barriers for Ammonia Synthesis on Metal Nitrides ($Ta_3N_5$, $Mn_6N_5$, $Fe_3Mo_3N$, $Co_3Mo_3N$). *Crystals* **2024**, *14*, 392. [CrossRef]
151. Henkelman, G.; Uberuaga, B.P.; Jónsson, H. A climbing image nudged elastic band method for finding saddle points and minimum energy paths. *J. Chem. Phys.* **2000**, *113*, 9901–9904. [CrossRef]
152. Chen, Z.; Wang, T. Toward High-Performance Electrochemical Ammonia Synthesis by Circumventing the Surface H-Mediated $N_2$ Reduction. *JACS Au* **2024**, *4*, 4023–4031. [CrossRef] [PubMed]
153. Fang, Z.; Liang, Y.; Li, Y.; Ni, B.; Zhu, J.; Li, Y.; Huang, S.; Lin, W.; Zhang, Y. Theoretical Insight into the Special Synergy of Bimetallic Site in Co/MoC Catalyst to Promote $N_2$-to-$NH_3$ Conversion. *Chem. Eur. J.* **2024**, *30*, e202302900. [CrossRef]
154. Kour, G.; Mao, X.; Du, A. Computational screening of single-atom alloys TM@Ru(0001) for enhanced electrochemical nitrogen reduction reaction. *J. Mater. Chem. A* **2022**, *10*, 6204–6215. [CrossRef]
155. Li, S.; Zhou, Y.; Li, K.; Saccoccio, M.; Sažinas, R.; Andersen, S.Z.; Pedersen, J.B.; Fu, X.; Shadravan, V.; Chakraborty, D.; et al. Electrosynthesis of ammonia with high selectivity and high rates via engineering of the solid-electrolyte interphase. *Joule* **2022**, *6*, 2083–2101. [CrossRef]
156. Liu, J.-C.; Ma, X.-L.; Li, Y.; Wang, Y.-G.; Xiao, H.; Li, J. Heterogeneous $Fe_3$ single-cluster catalyst for ammonia synthesis via an associative mechanism. *Nat. Commun.* **2018**, *9*, 1610. [CrossRef]
157. Zhou, Y.; Xu, C.-Q.; Tan, Z.; Cai, H.; Wang, X.; Li, J.; Zheng, L.; Au, C.-t.; Li, J.; Jiang, L. Integrating Dissociative and Associative Routes for Efficient Ammonia Synthesis over a TiCN-Promoted Ru-Based Catalyst. *ACS Catal.* **2022**, *12*, 2651–2660. [CrossRef]
158. Fuller, J.; Fortunelli, A.; Goddard, W.A.G.; Qi, A. Reaction Mechanism and Kinetics for Ammonia Synthesis on the Fe(211) Reconstructed Surface. *Phys. Chem. Chem. Phys.* **2019**, *21*, 11444–11454. [CrossRef]
159. Lefferts, L. Leveraging Expertise in Thermal Catalysis to Understand Plasma Catalysis. *Angew. Chem. Int. Ed.* **2024**, *63*, e202305322. [CrossRef] [PubMed]
160. Li, Z.; Liu, S.; Zhan, Q.; Li, J.; Zhang, Z.; Qian, Y.; Cai, Y.; Mu, X.; Li, L. Synergistic Enhancement of Plasma-Driven Ammonia Synthesis Using a $AuCu_3$/Cu Composite Catalyst. *Angew. Chem. Int. Ed.* **2025**, *64*, e202424165. [CrossRef]
161. Wei, Y.; Jiang, W.; Liu, Y.; Bai, X.; Hao, D.; Ni, B.-J. Recent Advances in Photocatalytic Nitrogen Fixation and Beyond. *Nanoscale* **2022**, *14*, 2990–2997. [CrossRef] [PubMed]
162. Wang, S.; Zhao, T.; Yan, L. Tailoring of Three-Atom Metal Cluster Catalysts for Ammonia Synthesis. *Catalysts* **2023**, *13*, 869. [CrossRef]
163. Chang, M.; Jing, W.; Li, X.; Zhang, L. Single-atomic site catalysts for electrochemical nitrogen fixation. *Mater. Res. Lett.* **2023**, *11*, 697–712. [CrossRef]
164. Iqbal, A.; Skulason, E.; Abghoui, Y. Electrochemical Nitrogen Reduction to Ammonia at Ambient Condition on the (111) Facets of Transition Metal Carbonitrides. *ChemPhysChem* **2024**, *25*, e202300991. [CrossRef] [PubMed]
165. Hao, Q.; Liu, C.; Jia, G.; Wang, Y.; Arandiyan, H.; Wei, W.; Ni, B.-J. Catalytic Reduction of Nitrogen to produce Ammonia by Bismuth-Based Catalysts: State of the Art and Future Prospects. *Mater. Horiz.* **2020**, *7*, 1014–1029. [CrossRef]
166. Saeidi, N.; Esrafili, M.D.; Sardroodi, J.J. Electrochemical Reduction of $N_2$ to $NH_3$ Using a Co-Atom Stabilized on Defective N-Doped Graphene: A Computational Study. *ChemistrySelect* **2019**, *4*, 12216–12226. [CrossRef]
167. Kiani, D.; Wachs, I.E. The Conundrum of "Pair Sites" in Langmuir–Hinshelwood Reaction Kinetics in Heterogeneous Catalysis. *ACS Catal.* **2024**, *14*, 10260–10270. [CrossRef]
168. Zeinalipour-Yazdi, C.D.; Hargreaves, J.S.J.; Catlow, C.R.A. DFT-D3 Study of Molecular $N_2$ and H2 Activation on Co3Mo3N Surfaces. *J. Phys. Chem. C* **2016**, *120*, 21390–21398. [CrossRef]
169. Fukutani, K.; Yoshinobu, J.; Yamauchi, M.; Shima, T.; Orimo, S. Hydrogenomics: Efficient and Selective Hydrogenation of Stable Molecules Utilizing Three Aspects of Hydrogen. *Catal. Lett.* **2022**, *152*, 1583–1597. [CrossRef]
170. Qian, J.; An, Q.; Fortunelli, A.; Nielsen, R.J.; Goddard, W.A. Reaction Mechanism and Kinetics for Ammonia Synthesis on the Fe(111) Surface. *J. Am. Chem. Soc.* **2018**, *140*, 6288–6297. [CrossRef]
171. Back, S.; Jung, Y. On the Mechanism of Electrochemical Ammonia Synthesis on the Ru Catalyst. *Phys. Chem. Chem. Phys.* **2016**, *18*, 9161–9166. [CrossRef] [PubMed]
172. Irving Langmuir Nobel Lecture 1932. Available online: https://www.nobelprize.org/prizes/chemistry/1932/langmuir/lecture/ (accessed on 17 March 2025).
173. Hougen, O.A.; Watson, K.M. General Principles. *Industr. Eng. Chem.* **1943**, *35*, 529–541. [CrossRef]

174. Langmuir, I. The dissociation of hydrogen into atoms. III. The mechanism of the reaction. *J. Am. Chem. Soc.* **1916**, *38*, 1145–1156. [CrossRef]
175. Langmuir, I. The Mechanism of the Catalytic Action of Platinum in the Reactions $2Co + O_2 = 2CO_2$ and $2H_2 + O_2 = 2H_2O$. *Trans. Faraday Soc.* **1922**, *17*, 621–654. [CrossRef]
176. Hinshelwood, S.C.N. *The Kinetics of Chemical Change in Gaseous Systems*; Clarendon Press: Oxford, UK, 1926.
177. Hinshelwood, C.N.; Hutchison, W.K. A Homogeneous Unimolecular Reactions-The Thermal Decomposition of Acetone in the Gaseous State. *Proc. Roy. Soc. A* **1926**, *111*, 245–257.
178. Hinshelwood, C.N.; Thompson, H.W.; Hartley, H.B. The Kinetics of the Combination of Hydrogen and Oxygen. *Proc. Roy. Soc. A* **1997**, *118*, 170–183. [CrossRef]
179. Hinshelwood, C.N. The Mechanism of Chemical Reactions. *J. Chem. Soc.* **1933**, 1357–1360. [CrossRef]
180. Mortensen, J.J.; Hammer, B.; Nørskov, J.K. Alkali Promotion of $N_2$ Dissociation over Ru(0001). *Phys. Rev. Lett.* **1998**, *80*, 4333–4336. [CrossRef]
181. Kim, Y.K.; Morgan, G.A.; Yates, J.T. Site-specific dissociation of $N_2$ on the stepped Ru(109) surface. *Surf. Sci.* **2005**, *598*, 14–21. [CrossRef]
182. Wang, Q.; Pan, J.; Guo, J.; Hansen, H.A.; Xie, H.; Jiang, L.; Hua, L.; Li, H.; Guan, Y.; Wang, P.; et al. Ternary ruthenium complex hydrides for ammonia synthesis via the associative mechanism. *Nat. Catal.* **2021**, *4*, 959–967. [CrossRef]
183. Almithn, A. Phosphorus Modification of Iron: Mechanistic Insights into Ammonia Synthesis on $Fe_2P$ Catalyst. *Molecules* **2024**, *29*, 1894. [CrossRef] [PubMed]
184. Zeinalipour-Yazdi, C.D.; Hargreaves, J.S.J.; Catlow, C.R.A. Nitrogen Activation in a Mars–van Krevelen Mechanism for Ammonia Synthesis on $Co_3Mo_3N$. *J. Phys. Chem. C* **2015**, *119*, 28368–28376. [CrossRef]
185. Medford, A.J.; Vojvodic, A.; Hummelshøj, J.S.; Voss, J.; Abild-Pedersen, F.; Studt, F.; Bligaard, T.; Nilsson, A. From the Sabatier Principle to a Predictive Theory of Transition-Metal Heterogeneous Catalysis. *J. Catal.* **2015**, *328*, 36–42. [CrossRef]
186. Hagen, S.; Barfod, R.; Fehrmann, R.; Jacobsen, C.J.H.; Teunissen, H.T.; Chorkendorff, I. Ammonia Synthesis with Barium-Promoted Iron–Cobalt Alloys Supported on Carbon. *J. Catal.* **2003**, *214*, 327–335. [CrossRef]
187. Skúlason, E.; Bligaard, T.; Gudmundsdóttir, S.; Studt, F.; Rossmeisl, J.; Abild-Pedersen, F.; Vegge, T.; Jónsson, H.; Nørskov, J.K. A Theoretical Evaluation of Possible Transition Metal Electro-Catalysts for $N_2$ Reduction. *Phys. Chem. Chem. Phys.* **2011**, *14*, 1235–1245. [CrossRef]
188. Wang, S.; Petzold, V.; Tripkovic, V.; Kleis, J.; Howalt, J.G.; Skúlason, E.; Fernández, E.M.; Hvolbæk, B.; Jones, G.; Toftelund, A.; et al. Universal Transition State Scaling Relations for (de)Hydrogenation over Transition Metals. *Phys. Chem. Chem. Phys.* **2011**, *13*, 20760–20765. [CrossRef]
189. Qiu, M.; Li, Y.; Zhang, Y. The synthesis mechanism of nitrogen to ammonia on the Fe, Co, Ni-doped Cu(100) Surface: A DFT study. *Appl. Surf. Sci.* **2022**, *573*, 151477. [CrossRef]
190. Nwaokorie, C.F.; Montemore, M.M. Alloy Catalyst Design beyond the Volcano Plot by Breaking Scaling Relations. *J. Phys. Chem. C* **2022**, *126*, 3993–3999. [CrossRef]
191. Stratton, S.M.; Zhang, S.; Montemore, M.M. Addressing complexity in catalyst design: From volcanos and scaling to more sophisticated design strategies. *Surf. Sci. Rep.* **2023**, *78*, 100597. [CrossRef]
192. Ma, X.-L.; Liu, J.-C.; Xiao, H.; Li, J. Surface Single-Cluster Catalyst for $N_2$-to-$NH_3$ Thermal Conversion. *J. Am. Chem. Soc.* **2018**, *140*, 46–49. [CrossRef] [PubMed]
193. Nguyen, L.; Zhang, S.; Wang, L.; Li, Y.; Yoshida, H.; Patlolla, A.; Takeda, S.; Frenkel, A.I.; Tao, F. Reduction of Nitric Oxide with Hydrogen on Catalysts of Singly Dispersed Bimetallic Sites $Pt_1Co_m$ and $Pd_1Co_n$. *ACS Catal.* **2016**, *6*, 840–850. [CrossRef]
194. Liu, L.; Corma, A. Bimetallic Sites for Catalysis: From Binuclear Metal Sites to Bimetallic Nanoclusters and Nanoparticles. *Chem. Rev.* **2023**, *123*, 4855–4933. [CrossRef]
195. Liu, D.; Zhao, W.; Yuan, Q. Breaking the Linear Relation in the Dissociation of Nitrogen on Iron Surfaces. *ChemPhysChem* **2022**, *23*, e202200147. [CrossRef] [PubMed]
196. Elahi, N.; Zeinalipour-Yazdi, C.D. Recent Advances in Ammonia Synthesis Modeling and Experiments on Metal Nitrides and Other Catalytic Surfaces. *Crystals* **2024**, *14*, 818. [CrossRef]
197. Zybert, M.; Ronduda, H.; Patkowski, W.; Ostrowski, A.; Sobczak, K.; Raróg-Pilecka, W. Improving the catalytic performance of $Co/BaCeO_3$ catalyst for ammonia synthesis by Y-modification of the perovskite-type support. *RSC Adv.* **2024**, *14*, 36281–36294. [CrossRef] [PubMed]
198. Langmuir, I. Part II.—"Heterogeneous Reactions". Chemical Reactions on Surfaces. *Trans. Faraday Soc.* **1922**, *17*, 607–620. [CrossRef]
199. Prins, R. Eley–Rideal, the Other Mechanism. *Top. Catal.* **2018**, *61*, 714–721. [CrossRef]
200. Ben Yaala, M.; Saeedi, A.; Scherrer, D.-F.; Moser, L.; Steiner, R.; Zutter, M.; Oberkofler, M.; De Temmerman, G.; Marot, L.; Meyer, E. Plasma-assisted catalytic formation of ammonia in $N_2$–$H_2$ plasma on a tungsten surface. *Phys. Chem. Chem. Phys.* **2019**, *21*, 16623–16633. [CrossRef]

201. Li, C.; Wang, T.; Gong, J. Alternative Strategies Toward Sustainable Ammonia Synthesis. *Trans. Tianjin Univ.* **2020**, *26*, 67–91. [CrossRef]
202. Li, J.; Xiong, Q.; Mu, X.; Li, L. Recent Advances in Ammonia Synthesis: From Haber-Bosch Process to External Field Driven Strategies. *ChemSusChem* **2024**, *17*, e202301775. [CrossRef] [PubMed]
203. Ye, D.; Tsang, S.C.E. Prospects and challenges of green ammonia synthesis. *Nat. Synth.* **2023**, *2*, 612–623. [CrossRef]
204. Dumesic, J.A.; Rudd, D.F.; Aparicio, L.M.; Rekoske, J.E.; Treviño, A.A. *The Microkinetics of Heterogeneous Catalysis*; American Chemical Society: Washington, DC, USA, 1993.
205. Stoltze, P.; Nørskov, J.K. An Interpretation of the High-Pressure Kinetics of Ammonia Synthesis Based on a Microscopic Model. *J. Catal.* **1988**, *110*, 1–10. [CrossRef]
206. Zeinalipour-Yazdi, C.D.; Hargreaves, J.S.J.; Laassiri, S.; Catlow, C.R.A. The Integration of Experiment and Computational Modelling in Heterogeneously Catalysed Ammonia Synthesis over Metal Nitrides. *Phys. Chem. Chem. Phys.* **2018**, *20*, 21803–21808. [CrossRef] [PubMed]
207. Tian, F.; Zhou, N.; Chen, W.; Zhan, J.; Tang, L.; Wu, M. Progress in Green Ammonia Synthesis Technology: Catalytic Behavior of Ammonia Synthesis Catalysts. *Adv. Sustain. Sys.* **2024**, *8*, 2300618. [CrossRef]
208. Strongin, D.R.; Carrazza, J.; Bare, S.R.; Somorjai, G.A. The importance of C7 sites and surface roughness in the ammonia synthesis reaction over iron. *J. Catal.* **1987**, *103*, 213–215. [CrossRef]
209. Ravi, M.W.; Makepeace, J. Facilitating Green Ammonia Manufacture under Milder Conditions: What Do Heterogeneous Catalyst Formulations Have to Offer? *Chem. Sci.* **2022**, *13*, 890–908. [CrossRef]
210. van der Ham, C.J.M.; Koper, M.T.M.; Hetterscheid, D.G.H. Challenges in Reduction of Dinitrogen by Proton and Electron Transfer. *Chem. Soc. Rev.* **2014**, *43*, 5183–5191. [CrossRef]
211. Sajid, M.; Kaden, W.E.; Kara, A. DFT Investigation of Ammonia Formation via a Langmuir–Hinshelwood Mechanism on Mo-Terminated δ-MoN(0001). *ACS Omega* **2022**, *7*, 4277–4285. [CrossRef]
212. Horiuti, I.; Polanyi, M. Exchange Reactions of Hydrogen on Metallic Catalysts. *Trans. Faraday Soc.* **1934**, *30*, 1164–1172. [CrossRef]
213. Xie, W.; Reid, G.; Hu, P. Discovery of a New Solvent Co-Catalyzed Mechanism in Heterogeneous Catalysis: A First-Principles Study with Molecular Dynamics on Acetaldehyde Hydrogenation on Birnessite. *JACS Au* **2022**, *2*, 328–334. [CrossRef] [PubMed]
214. Yang, B.; Gong, X.Q.; Wang, H.F.; Cao, X.M.; Rooney, J.J.; Hu, P. Evidence to challenge the universality of the Horiuti-Polanyi mechanism for hydrogenation in heterogeneous catalysis: Origin and trend of the preference of a non-Horiuti-Polanyi mechanism. *J. Am. Chem. Soc.* **2013**, *135*, 15244–15250. [CrossRef] [PubMed]
215. Sun, X.; Chen, J.; Hu, P. General trends in Horiuti-Polanyi mechanism vs non-Horiuti-Polanyi mechanism for water formation on transition metal surfaces. *Chin. J. Catal.* **2020**, *41*, 294–301. [CrossRef]
216. Deng, X.; Wang, J.; Guan, N.; Li, L. Catalysts and mechanisms for the selective heterogeneous hydrogenation of carbon-carbon triple bonds. *Cell Rep. Phys. Sci.* **2022**, *3*, 101017. [CrossRef]
217. Faria, J.A. Renaissance of ammonia synthesis for sustainable production of energy and fertilizers. *Curr. Opin. Green Sustain. Chem.* **2021**, *29*, 100466. [CrossRef]
218. Zeinalipour-Yazdi, C.D. Mechanisms of Ammonia and Hydrazine Synthesis on η-$Mn_3N_2$-(100) Surfaces. *Phys. Chem. Chem. Phys.* **2019**, *21*, 19365–19377. [CrossRef] [PubMed]
219. Miyahara, S.-I.; Sato, K.; Kawano, Y.; Imamura, K.; Ogura, Y.; Tsujimaru, K.; Nagaoka, K. Ammonia synthesis over lanthanoid oxide–supported ruthenium catalysts. *Catal. Today* **2021**, *376*, 36–40. [CrossRef]
220. Brennen, W.; Shuman, M.E. Kinetics of the Langmuir-Rideal mechanism for heterogeneous atom recombination. *J. Phys. Chem.* **1978**, *82*, 2715–2719. [CrossRef]
221. Kammler, T.; Wehner, S.; Küppers, J. The role of sticking and reaction probabilities in hot-atom mediated abstraction reactions of D on metal surfaces by gaseous H atoms. *J. Chem. Phys.* **1998**, *109*, 4071–4077. [CrossRef]
222. Harris, J.; Kasemo, B. On Precursor Mechanisms for Surface Reactions. *Surf. Sci. Lett.* **1981**, *105*, L281–L287. [CrossRef]
223. Rideal, E.K. A note on a simple molecular mechanism for heterogeneous catalytic reactions. *Math. Proc. Camb. Phil. Soc.* **1939**, *35*, 130–132. [CrossRef]
224. Eley, D.D.; Rideal, E.K. Parahydrogen Conversion on Tungsten. *Nature* **1940**, *146*, 401–402. [CrossRef]
225. Eley, D.D. The Catalytic Activation of Hydrogen. In *Advances in Catalysis*; Frankenburg, W.G., Komarewsky, V.I., Rideal, E.K., Eds.; Academic Press: New York, NY, USA, 1948; Volume 1, pp. 157–199.
226. Fertig, M. Finite Rate Surface Catalysis Modelling of PM1000 and SiC Employing the DLR CFD Solver TAU. In Proceedings of the 8th European Symposium on Aerothermodynamics for Space Vehicles, Lisbon, Portugal, 2–6 March 2015.
227. Ellis, J.; Köpp, D.; Lang, N.; van Helden, J.H. Evidence of the dominant production mechanism of ammonia in a hydrogen plasma with parts per million of nitrogen. *Appl. Phys. Lett.* **2021**, *119*, 241601. [CrossRef]
228. Rouwenhorstm, K.H.R.; Lefferts, L. Plasma-catalytic Ammonia Synthesis via Eley-Rideal Reactions: A Kinetic Analysis. *ChemCatChem* **2023**, *15*, e202300078. [CrossRef]

229. Zeinalipour-Yazdi, C.D. On the possibility of an Eley–Rideal mechanism for ammonia synthesis on $Mn_6N_{5+x}$ ($x$ = 1)-(111) surfaces. *Phys. Chem. Chem. Phys.* **2018**, *20*, 18729–18736. [CrossRef] [PubMed]
230. Zhang, T.; Zhou, R.; Zhang, S.; Zhou, R.; Ding, J.; Li, F.; Hong, J.; Dou, L.; Shao, T.; Murphy, A.B.; et al. Sustainable Ammonia Synthesis from Nitrogen and Water by One-Step Plasma Catalysis. *Energy Environ. Mater.* **2023**, *6*, e12344. [CrossRef]
231. Jesudass, S.C.; Surendran, S.; Kim, J.Y.; An, T.-Y.; Janani, G.; Kim, T.-H.; Kim, J.K.; Sim, U. Pathways of the Electrochemical Nitrogen Reduction Reaction: From Ammonia Synthesis to Metal-$N_2$ Batteries. *Electrochem. Energy Rev.* **2023**, *6*, 27. [CrossRef]
232. Laassiri, S.; Zeinalipour-Yazdi, C.D.; Catlow, C.R.A.; Hargreaves, J.S.J. The potential of manganese nitride based materials as nitrogen transfer reagents for nitrogen chemical looping. *Appl. Catal. B* **2018**, *223*, 60–66. [CrossRef]
233. Abghoui, Y.; Garden, A.L.; Hlynsson, V.F.; Björgvinsdóttir, S.; Ólafsdóttir, H.; Skúlason, E. Enabling electrochemical reduction of nitrogen to ammonia at ambient conditions through rational catalyst design. *Phys. Chem. Chem. Phys.* **2015**, *17*, 4909–4918. [CrossRef]
234. Yao, Y.; Feng, Q.; Zhu, S.; Li, J.; Yao, Y.; Wang, Y.; Wang, Q.; Gu, M.; Wang, H.; Li, H.; et al. Chromium Oxynitride Electrocatalysts for Electrochemical Synthesis of Ammonia Under Ambient Conditions. *Small Methods* **2019**, *3*, 1800324. [CrossRef]
235. Zeinalipour-Yazdi, C.D.; Catlow, C.R.A. A Computational Study of the Heterogeneous Synthesis of Hydrazine on $Co_3Mo_3N$. *Catal. Lett.* **2017**, *147*, 1820–1826. [CrossRef] [PubMed]
236. Zhang, Y.; Li, J.; Zhou, Y.; Au, C.-t.; Wang, X.; Jiang, L. Recent progress of thermocatalytic ammonia synthesis via an associative mechanism. *Fundam. Res.* **2024**, *in press*. [CrossRef]
237. Li, L.; Zhang, T.; Cai, J.; Cai, H.; Ni, J.; Lin, B.; Lin, J.; Wang, X.; Zheng, L.; Au, C.-T.; et al. Operando spectroscopic and isotopic-label-directed observation of LaN-promoted $Ru/ZrH_2$ catalyst for ammonia synthesis via associative and chemical looping route. *J. Catal.* **2020**, *389*, 218–228. [CrossRef]
238. Chebrolu, V.T.; Jang, D.; Rani, G.M.; Lim, C.; Yong, K.; Kim, W.B. Overview of emerging catalytic materials for electrochemical green ammonia synthesis and process. *Carbon Energy* **2023**, *5*, e361. [CrossRef]
239. Abghoui, Y.; Garden, A.L.; Howalt, J.G.; Vegge, T.; Skúlason, E. Electroreduction of $N_2$ to Ammonia at Ambient Conditions on Mononitrides of Zr, Nb, Cr, and V: A DFT Guide for Experiments. *ACS Catal.* **2016**, *6*, 635–646. [CrossRef]
240. Guan, Y.; Zhang, W.; Wang, Q.; Weidenthaler, C.; Wu, A.; Gao, W.; Pei, Q.; Yan, H.; Cui, J.; Wu, H.; et al. Barium chromium nitride-hydride for ammonia synthesis. *Chem. Catal.* **2021**, *1*, 1042–1054. [CrossRef]
241. Wang, G.; Batista, E.R.; Yang, P. $N_2$-to-$NH_3$ conversion by excess electrons trapped in point vacancies on 5f-element dioxide surfaces. *Front. Chem.* **2023**, *10*, 1051496. [CrossRef]
242. Tian, F.; Li, J.; Chen, W.; Tang, L.; Wu, M. Innovative progress of thermal ammonia synthesis under mild conditions. *Int. J. Hydrogen Energy* **2024**, *78*, 92–122. [CrossRef]
243. Tang, Y.; Kobayashi, Y.; Masuda, N.; Uchida, Y.; Okamoto, H.; Kageyama, T.; Hosokawa, S.; Loyer, F.; Mitsuhara, K.; Yamanaka, K.; et al. Metal-Dependent Support Effects of Oxyhydride-Supported Ru, Fe, Co Catalysts for Ammonia Synthesis. *Adv. Energy Mater.* **2018**, *8*, 1801772. [CrossRef]
244. Li, X.F.; Li, Q.K.; Cheng, J.; Liu, L.; Yan, Q.; Wu, Y.; Zhang, X.H.; Wang, Z.Y.; Qiu, Q.; Luo, Y. Conversion of Dinitrogen to Ammonia by FeN3-Embedded Graphene. *J. Am. Chem. Soc.* **2016**, *138*, 8706–8709. [CrossRef] [PubMed]
245. Peng, X.; Zhang, M.; Zhang, T.; Zhou, Y.; Ni, J.; Wang, X.; Jiang, L. Single-atom and cluster catalysts for thermocatalytic ammonia synthesis at mild conditions. *Chem. Sci.* **2024**, *15*, 5897–5915. [CrossRef] [PubMed]
246. Ertl, G. Reactions at Surfaces: From Atoms to Complexity (Nobel Lecture). *Angew. Chem. Int. Ed.* **2008**, *47*, 3524–3535. [CrossRef] [PubMed]
247. Wang, X.; Li, L.; Fang, Z.; Zhang, Y.; Ni, J.; Lin, B.; Zheng, L.; Au, C.-t.; Jiang, L. Atomically Dispersed Ru Catalyst for Low-Temperature Nitrogen Activation to Ammonia via an Associative Mechanism. *ACS Catal.* **2020**, *10*, 9504–9514. [CrossRef]
248. Ghuman, K.K.; Tozaki, K.; Sadakiyo, M.; Kitano, S.; Oyabe, T.; Yamauchi, M. Tailoring widely used ammonia synthesis catalysts for H and N poisoning resistance. *Phys. Chem. Chem. Phys.* **2019**, *21*, 5117–5122. [CrossRef] [PubMed]
249. Foster, S.L.; Bakovic, S.I.P.; Duda, R.D.; Maheshwari, S.; Milton, R.D.; Minteer, S.D.; Janik, M.J.; Renner, J.N.; Greenlee, L.F. Catalysts for nitrogen reduction to ammonia. *Nat. Catal.* **2018**, *1*, 490–500. [CrossRef]
250. Goodwin, C.M.; Lömker, P.; Degerman, D.; Davies, B.; Shipilin, M.; Garcia-Martinez, F.; Koroidov, S.; Katja Mathiesen, J.; Rameshan, R.; Rodrigues, G.L.S.; et al. Operando probing of the surface chemistry during the Haber-Bosch process. *Nature* **2024**, *625*, 282–286. [CrossRef]
251. Sun, B.; Lu, S.; Qian, Y.; Zhang, X.; Tian, J. Recent progress in research and design concepts for the characterization, testing, and photocatalysts for nitrogen reduction reaction. *Carbon Energy* **2023**, *5*, e305. [CrossRef]
252. Hou, J.; Yang, M.; Zhang, J. Recent advances in catalysts, electrolytes and electrode engineering for the nitrogen reduction reaction under ambient conditions. *Nanoscale* **2020**, *12*, 6900–6920. [CrossRef]
253. Peng, X.; Liu, H.-X.; Zhang, Y.; Huang, Z.-Q.; Yang, L.; Jiang, Y.; Wang, X.; Zheng, L.; Chang, C.; Au, C.-t.; et al. Highly efficient ammonia synthesis at low temperature over a Ru–Co catalyst with dual atomically dispersed active centers. *Chem. Sci.* **2021**, *12*, 7125–7137. [CrossRef]

254. Wei, P.; Wenya, Z.; Xueke, Y.; Lei, H.; Weizhi, X.; Zi, W.; Yongfeng, L.; Si, Z.; Yusong, T.; Jijun, Z. Computational design of spatially confined triatomic catalysts for nitrogen reduction reaction. *J. Mater. Inf.* **2023**, *3*, 26. [CrossRef]
255. Wei, Z.; Feng, Y.; Ma, J. Co-doped graphene edge for enhanced N2-to-NH3 conversion. *J. Energy Chem.* **2020**, *48*, 322–327. [CrossRef]
256. Hoffman, B.M.; Lukoyanov, D.; Yang, Z.-Y.; Dean, D.R.; Seefeldt, L.C. Mechanism of Nitrogen Fixation by Nitrogenase: The Next Stage. *Chem. Rev.* **2014**, *114*, 4041–4062. [CrossRef]
257. Schrock, R.R. Catalytic Reduction of Dinitrogen to Ammonia at a Single Molybdenum Center. *Acc. Chem. Res.* **2005**, *38*, 955–962. [CrossRef]
258. Eady, R.R. Structure−Function Relationships of Alternative Nitrogenases. *Chem. Rev.* **1996**, *96*, 3013–3030. [CrossRef]
259. Peters, J.W.; Szilagyi, R.K. Exploring new frontiers of nitrogenase structure and mechanism. *Curr. Opin. Chem. Biol.* **2006**, *10*, 101–108. [CrossRef] [PubMed]
260. Hu, Y.; Lee, C.C.; Grosch, M.; Solomon, J.B.; Weigand, W.; Ribbe, M.W. Enzymatic Fischer–Tropsch-Type Reactions. *Chem. Rev.* **2023**, *123*, 5755–5797. [CrossRef]
261. Dance, I. The mechanism of Mo-nitrogenase: From $N_2$ capture to first release of $NH_3$. *Dalton Trans.* **2024**, *53*, 19360–19377. [CrossRef]
262. Einsle, O. Catalysis and structure of nitrogenases. *Curr. Opin. Struct. Biol.* **2023**, *83*, 102719. [CrossRef]
263. Threatt, S.D.; Rees, D.C. Biological nitrogen fixation in theory, practice, and reality: A perspective on the molybdenum nitrogenase system. *FEBS Lett.* **2023**, *597*, 45–58. [CrossRef]
264. Rutledge, H.L.; Tezcan, F.A. Electron Transfer in Nitrogenase. *Chem. Rev.* **2020**, *120*, 5158–5193. [CrossRef] [PubMed]
265. Thorneley, R.N.F.; Lowe, D.J. Kinetics and Mechanism of the Nitrogenase Enzyme System. In *Metal Ions in Biology: Molybdenum Enzymes*; Spiro, T.G., Ed.; Wiley-Interscience: New York, NY, USA, 1985; Volume 7, pp. 221–284.
266. Cao, L.; Ryde, U. Putative reaction mechanism of nitrogenase after dissociation of a sulfide ligand. *J. Catal.* **2020**, *391*, 247–259. [CrossRef]
267. Siegbahn, P.E.M. Model Calculations Suggest that the Central Carbon in the FeMo-Cofactor of Nitrogenase Becomes Protonated in the Process of Nitrogen Fixation. *J. Am. Chem. Soc.* **2016**, *138*, 10485–10495. [CrossRef] [PubMed]
268. Lukoyanov, D.; Dikanov, S.A.; Yang, Z.-Y.; Barney, B.M.; Samoilova, R.I.; Narasimhulu, K.V.; Dean, D.R.; Seefeldt, L.C.; Hoffman, B.M. ENDOR/HYSCORE Studies of the Common Intermediate Trapped during Nitrogenase Reduction of $N_2H_2$, $CH_3N_2H$, and $N_2H_4$ Support an Alternating Reaction Pathway for $N_2$ Reduction. *J. Am. Chem. Soc.* **2011**, *133*, 11655–11664. [CrossRef] [PubMed]
269. Raugei, S.; Seefeldt, L.C.; Hoffman, B.M. Critical computational analysis illuminates the reductive-elimination mechanism that activates nitrogenase for $N_2$ reduction. *Proc. Natl. Acad. Sci. USA* **2018**, *115*, E10521–E10530. [CrossRef]
270. Hinnemann, B.; Nørskov, J.K. Catalysis by Enzymes: The Biological Ammonia Synthesis. *Top. Catal.* **2006**, *37*, 55–70. [CrossRef]
271. Neese, F. The Yandulov/Schrock Cycle and the Nitrogenase Reaction: Pathways of Nitrogen Fixation Studied by Density Functional Theory. *Angew. Chem. Int. Ed.* **2006**, *45*, 196–199. [CrossRef]
272. Dance, I. Computational Investigations of the Chemical Mechanism of the Enzyme Nitrogenase. *ChemBioChem* **2020**, *21*, 1671–1709. [CrossRef] [PubMed]
273. Temkin, M.; Pyzhev, V. Kinetics of Ammonia Synthesis on Promoted Iron Catalysts. *Acta Physicochim. URSS* **1940**, *12*, 327–356.
274. Siporin, S.E.; Davis, R.J. Use of kinetic models to explore the role of base promoters on Ru/MgO ammonia synthesis catalysts. *J. Catal.* **2004**, *225*, 359–368. [CrossRef]
275. Rivera Rocabado, D.S.; Aizawa, M.; Noguchi, T.G.; Yamauchi, M.; Ishimoto, T. Uncovering the Mechanism of the Hydrogen Poisoning on Ru Nanoparticles via Density Functional Theory Calculations. *Catalysts* **2022**, *12*, 331. [CrossRef]
276. Imamura, K.; Miyahara, S.-I.; Kawano, Y.; Sato, K.; Nakasaka, Y.; Nagaoka, K. Kinetics of ammonia synthesis over $Ru/Pr_2O_3$. *J. Taiwan Inst. Chem. Eng.* **2019**, *105*, 50–56. [CrossRef]
277. Zhou, Y.; Wang, C.; Peng, X.; Zhang, T.; Wang, X.; Jiang, Y.; Qi, H.; Zheng, L.; Lin, J.; Jiang, L. Boosting Efficient Ammonia Synthesis over Atomically Dispersed Co-Based Catalyst via the Modulation of Geometric and Electronic Structures. *Chin. Chem. Soc. Chem.* **2022**, *4*, 1758–1769. [CrossRef]
278. Morimoto, R.; Ogawa, T.; Ishihara, K. The microkinetics of ammonia synthesis: The effect of surface coverage on apparent activation energy and reaction order. *ChemRxiv* **2022**. [CrossRef]
279. Tautermann, C.S.; Sturdy, Y.K.; Clary, D.C. Reaction rates of all hydrogenation steps in ammonia synthesis over a Ru(0001) surface. *J. Catal.* **2006**, *244*, 199–207. [CrossRef]
280. Jacobi, K. Nitrogen on Ruthenium Single-Crystal Surfaces. *Phys. Stat. Solidi* **2000**, *177*, 37–51. [CrossRef]
281. Aika, K.-I.; Ozaki, A. Mechanism and isotope effect in ammonia synthesis over molybdenum nitride. *J. Catal.* **1969**, *14*, 311–321. [CrossRef]
282. Volpe, L.; Boudart, M. Ammonia synthesis on molybdenum nitride. *J. Phys. Chem.* **1986**, *90*, 4874–4877. [CrossRef]

283. Tanaka, K.; Matsuyama, A. The Rate-Determining Stepo of Ammonia Synthesis and Decomposition: Part 3. Study of the Reaction over a Singly-Promoted Iron Catalyst at 340-390 °C. *J. Res. Inst. Catal. Hokkaido Univ.* **1971**, *19*, 63–84.
284. Horiuti, J. Stoichiometric Number and Universal Kinetic Law in the Neighbourhood of Equilibrium. *J. Res. Inst. Catal. Hokkaido Univ.* **1953**, *3*, 160–163.
285. Enomoto, S.; Horiuti, J. Stoichiometriv Number of Ammonia Synthesis Reaction. *Proc. Jpn. Acad.* **1952**, *28*, 499–504. [CrossRef]

**Disclaimer/Publisher's Note:** The statements, opinions and data contained in all publications are solely those of the individual author(s) and contributor(s) and not of MDPI and/or the editor(s). MDPI and/or the editor(s) disclaim responsibility for any injury to people or property resulting from any ideas, methods, instructions or products referred to in the content.